From Giants to Dwarfs:
A Comprehensive Observational Study of The Globular Cluster System Mass - Halo Mass Relation

FROM GIANTS TO DWARFS: A COMPREHENSIVE OBSERVATIONAL STUDY OF THE GLOBULAR CLUSTER SYSTEM MASS - HALO MASS RELATION

By Veronika DORNAN
M.Sc., McMaster University (Hamilton, ON)
B.Sc., Mount Allison University (Sackville, NB)

A Thesis Submitted to the Department of Physics and Astronomy and the School of Graduate Studies of McMaster University in the Partial Fulfillment of the Requirements for the Degree of Doctor of Philosophy

McMaster University
Doctor of Philosophy (2025)
Hamilton, Ontario (Department of Physics and Astronomy)

TITLE: From Giants to Dwarfs:
A Comprehensive Observational Study of The Globular Cluster System Mass - Halo Mass Relation
AUTHOR: Veronika DORNAN (McMaster University)
SUPERVISOR: Dr. William E. HARRIS
NUMBER OF PAGES: xiii, 146

Abstract

The scaling relation that exists between the total mass of all globular clusters (GCs) hosted by a galaxy and the total mass of that galaxy, which is dominated by its dark matter halo, has been known and studied for several decades. This GC system (GCS) mass - halo mass relation ($M_{GCS} - M_h$) has been observationally found to apply to nearly every galaxy observed. This relation is remarkably tight, linear, and spans over six orders of magnitude in halo mass. Understanding what drives this linearity and what evolutionary mechanisms affect where a galaxy sits on this relation can allow us to probe both galaxy and GCS evolution. In order to do so, an observational sample of high-quality, homogeneous data, which spans the full range of galaxy masses in the local universe is necessary. This thesis addresses this need through the design of a novel method of determining GC radial density profiles which improves the accuracy and precision of N_{GC} estimates for massive galaxies, the application of this method to a sample of 27 brightest cluster galaxies (BCGs), and the compilation of a literature catalog of dwarf galaxy GCSs with standardized GCS and halo mass estimates. With such a complete and methodologically consistent sample we were able to study what properties of GCSs are driving the intrinsic scatter in the relation. We found that, for extremely massive galaxies, positive offset from the relation was associated with more shallow GC radial density profiles, driven specifically by the red GC sub-populations. We also found that ultra diffuse galaxies (UDGs) and extremely low mass and low surface brightness dwarf galaxies were systematically positively offset from the relation compared to their classical dwarf counterparts. BCGs are known to be formed from extensive merger histories, and UDGs are thought to be formed through extreme tidal interactions. Together, these results imply that the merger and tidal histories of galaxies have the greatest affect on the evolution of their GCSs, and by extension, their position on the relation. Studies of GCSs, therefore, are an important tool in tracing galaxy evolution. With this sample, the $M_{GCS} - M_h$ relation has been studied comprehensively from the lowest-mass to the highest-mass galaxies in the local universe; the most complete study of its kind to date.

Acknowledgements

There are many people at McMaster I would like to thank for their support and guidance during my time as a graduate student. First and foremost, I need to thank my supervisor Dr Bill Harris. It is a tremendous privilege to have learned about globular clusters from *the* globular cluster guy and to join the never-ending list of Harris group alumni. Your supervisory approach allowed me the freedom to pursue the projects I was interested in and the opportunity to try things for myself, while still always being there to give me the direction I needed, and to set me back on the right path whenever I (inevitably) got too lost in the weeds of what I was working on. I couldn't have asked for a better mentor through this process.

I would also like to thank the members of my supervisory committee, Drs Alison Sills and Laura Parker. You both have been outstanding sources of encouragement and critique in just the right balance to make my work better and my confidence in myself as a researcher grow. You have supported me as teachers, mentors, and leaders in our department when I needed it most. Next, I would like to thank Dr Robert Cockcroft (one of the many Bill Harris alums himself!). While some may believe that working in the planetarium is unconnected to writing a PhD thesis, they would be dead wrong. The opportunities you have given me in astronomy outreach through the planetarium have been incredibly valuable to me and have helped me see my research in new ways. The feedback you have given me has helped me hone my science communication skills in both public speaking and writing. I truly believe this thesis would not be nearly as well-written without you.

Thank you to my office mates and friends who have been with me for the entirety of this PhD! Kate, Hector, Joey, Megan, Lauren, Rachel, and Taavishi, you folks have been amazing friends, conference buddies, and in many cases, water polo teammates. I have always known you were there for me if I needed someone to talk to, whether it was about observations, simulations, coding, LaTeX, or just for a laugh. Special thank you to Billy too – it's a shame you didn't arrive at McMaster earlier because I wish I had been playing squash with you every week these past six years. I will dearly miss this time I've spent with all of you in one place.

I want to sincerely thank Claude Cournoyer-Cloutier and Blake Ledger. You two have been with me since day one of grad school and I couldn't have imagined it any other way. The help and support you both gave me through my graduate courses, master's defence, comprehensive exam, post-doc applications, and now PhD denfence have been beyond words. You two are among the first I call when things go horribly wrong and you're always there to pick up. You both inspire me to be a better researcher – your accomplishments so far have been outstanding to watch and I know you are only just getting started.

Lastly, Jeremy. I want you to read all the ways I thanked everyone else already and know that every single one of those apply to you too. How lucky am I to have someone like you by my side? I'm constantly amazed that I have such an incredible astronomer as you at the desk across from me to talk to everyday. You help me understand my research and where it fits in the big picture better, both by answering my questions and by asking me your own. I joked in the acknowledgements of my Master's thesis four years ago that "I probably could have done it without you, but I definitely wouldn't have wanted to", but I truly don't think I could have done this one without you. You are friend, collaborator, and partner all rolled into one. You have been there for me through the most difficult parts of this when my future has felt the most uncertain, and you have also been there to celebrate my biggest achievements with me and remind me that my future may yet still be bright. We may be just about as physically far apart as two people can be in a few months, but I know I will still have you close in my heart (and likely inbox). I'm so happy they put your desk across from mine. I love you.

P.S. I also want to thank Bo for meowing as loud as possible in the background of important zoom calls. You keep me on my feet.

Contents

List of Figures

List of Tables

Declaration of Authorship

Chapters 2, 3, and 4 of this thesis present original research conducted and written by myself, Veronika Dornan. I obtained the data, performed the analysis, and created the figures, tables, and catalogs presented. For all of this work, my supervisor Dr. William E. Harris provided guidance on the direction and objectives of the research, in the interpretation of the results, and in the writing and editing process of the manuscripts.

"*People think of education as something they can finish*"

– Isaac Asimov

Chapter 1

Introduction

The major question at the heart of all astronomical research is “how did we end up here?”. How grand or granular you would like to interpret that question depends on subfield, but in extragalactic astronomy we attempt to answer it by probing the ways in which galaxies have formed and evolved to result in the array of properties we observe today. Observationally, we are restricted in how we approach this question, as while increasing the distance to the galaxies we observe will increase our lookback time and allow us to directly observe galaxies at different stages of the universe, in exchange we must sacrifice resolution, resulting in less precise information about those galaxies. Thus, if we restrict ourselves to the local Universe we must make use of tracers of galactic evolution; structures within galaxies today that can tell us about the changes their hosts have undergone up to this point. The most useful tracers for this purpose are luminous, allowing for ease of detection, numerous, allowing for a large sample size within each galaxy, and above all else, ancient, having survived throughout their hosts’ turbulent evolutionary histories.

Globular star clusters (GCs) check each of these boxes. The key properties of GCs that distinguish them from other types of star clusters are the extreme ages and concentrations of their stars. A typical GC hosted by The Milky Way (MW) has an age of $\sim$ 12.5 Gyr and contains $\sim 2 \times 10^5 M_\odot$, or $\sim 10^6$ stars, within a half-light radius less than just 10 pc (Peterson and King 1975; Harris 1996; VandenBerg et al. 2013; Ying et al. 2025). GCs are also ubiquitous and abundant within galaxies, with many residing in the outer regions, away from the very bright galactic centers. The MW hosts at least 170 known GCs, the majority of which are in the outskirts of the stellar halo (Vasiliev and Baumgardt 2021). This results in a very dense system of stars that is resistant to disruption from tidal forces, allowing it to survive to old age, is bright and compact enough to remain observable even at large distances, and exists in a large population around their host galaxy.

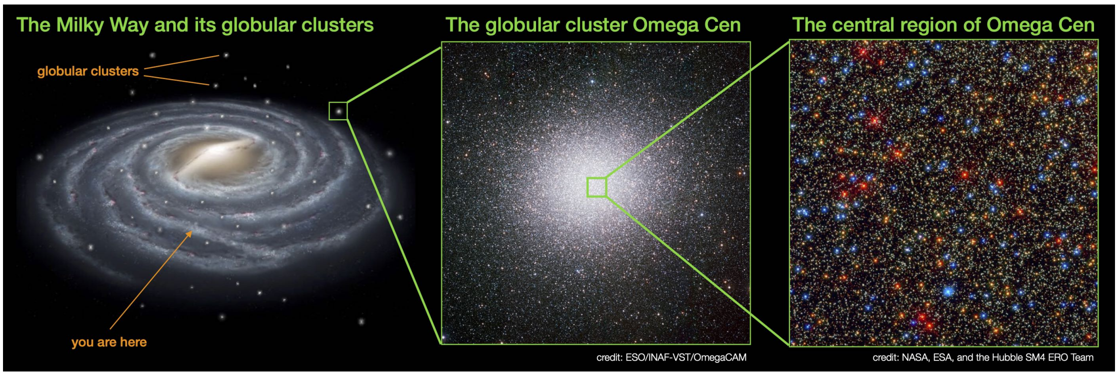

credit: ESO/INAF-VST/OmegaCAM

credit: NASA, ESA, and the Hubble SM4 ERO Team

FIGURE 1.1: GCs can be found in the stellar halo of galaxies, including the MW. The stars in GCs tend to follow a King model distribution, with central surface number densities on the order of 10^2 stars/pc^2 (de Boer et al. 2019). *Figure credit: Paolo Bianchini.*

This chapter will discuss the pertinent information on the role of GCs in the study of galaxy evolution. It will lay out: the theories of formation of GCs and how they relate to the environment of their host galaxy (1.1), the observed diversity in GC system (GCS) properties (1.2), and the significance of the scaling relation between GCS mass and the halo mass of its host galaxy (1.3).

1.1 Globular Cluster Formation Theories

Although GCs are some of the most well-studied structures within the MW, we have yet to reach a consensus on their formation mechanisms. Generally, GC formation theories can be divided into two camps. The first hosts those that suggest that GCs formed as the stellar component of gas-rich dark matter (DM) mini-halos which were then stripped of their DM envelopes as they fell into larger, central galaxies. The second camp hosts those that suggest that GCs formed with similar mechanisms to the young massive clusters (YMCs) which we observe at the present day, but within the dramatically different environment of the early universe, resulting in their different characteristic masses and densities.

These GC formation theories are required to explain a variety of present-day GC properties that we observe both within the Milky Way and extragalactically. These include a lack of dark matter, a range of ages and metallicities, and a characteristic GC luminosity function (GCLF). Although for the most part these properties seem to be universal for GCs everywhere, they also depend somewhat on environment (more on this in Section 1.2).

1.1.1 Globular Cluster Formation in Dark Matter Mini-Halos

It has been proposed that gas-rich but star-free DM mini-halos are capable of forming in the early universe alongside, but separately from, proto-galaxies (Peebles and Dicke 1968; Peebles 1984; Fall and Rees 1985). These mini-halos, with masses around $\sim 10^7 - 10^8 M_\odot$ would also be capable of having their gas cool and collapse and form central star clusters (Padoan et al. 1997). In other cases, collapse is thought to be triggered by external forces, such as mergers between halos during galactic infall, causing compression of the gas reservoirs and therefore bursts of star formation (Trenti et al. 2015). Mini-halo-mini-halo mergers could also be capable of removing the DM from the resulting GC if they occurred at supersonic speeds, which would allow the DM to pass unimpeded, while the gas reservoirs would collide and decouple (Madau et al. 2020; van Dokkum et al. 2022) (a similar, although much smaller scale, version of what happened to the Bullet Cluster (Springel and Farrar 2007)).

These DM-dependent theories of GC formation are also appealing as they yield a baked-in origin for the observed scaling relation between number of GCs hosted by a galaxy and its DM halo mass (more on this in section 1.3). Here, as the DM envelopes are stripped from colliding mini-halos, they are accreted to the larger DM halo of the host galaxy, and due to the characteristic mass of these mini-halos a 1:1 relation emerges (Madau et al. 2020).

Some problems inevitably arise with these DM-dependent theories, however. For one, it is unlikely that *all* mini-halos collided at speeds high enough to fully strip their DM from their stellar and gas components during infall. For another, since these theories suggest that GCs formed in independent gas reservoirs of mini-halos, it is difficult to explain the observed variations in GC metallicities seen not only across galaxy masses and morphologies (Geisler et al. 1996;

Harris et al. 2016), but also across different positions in the MW (Leaman et al. 2013; Woody and Schlaufman 2021).

Vitral and Boldrini 2022 used N-body simulations to determine what properties of GCs could be observed that would indicate whether or not they had originally been embedded in a mini-halo at the time of infall. They found that mini-halos would hasten orbital decay for their clusters, but would also act as a shield from disruption caused by dynamical friction as they traveled through the potential well of their host galaxy, before eventually being stripped itself. As a result, if a GC was *not* originally hosted by a mini-halo we would expect to see stellar streams surrounding it, and a more diffuse stellar distribution. Those that *were* protected by a mini-halo would have more radial outer velocity anisotropy profiles and any DM that they could potentially still host would be entirely on the outskirts. Unfortunately, these properties can be difficult to study, both within and beyond the MW (Peñarrubia et al. 2017), making these GC formation theories tricky to confirm.

1.1.2 Globular Cluster Formation in Giant Molecular Clouds

To solve the issue of GCs' observed lack of DM, formation theories have been put forward that suggest that GC formation is not all that "special" in the early universe. While Peebles and Dicke 1968 originally had in mind a GC formation theory external to galaxy formation, as was discussed in the previous subsection, at the same time they noted that at high redshifts, when GCs would have formed, the Jeans mass would be around $10^6 M_\odot$, largely due to the much higher typical temperatures of the gas at these times (Dekel et al. 2009; Narayanan and Davé 2012). It has since been argued that because of this, the collapse of giant molecular clouds within galaxies at early times would result in a characteristic mass of the resulting GC close to what we observe today (Searle and Zinn 1978; Harris and Pudritz 1994). These gas-collapse theories of GC formation support the idea that GCs formed using the same mechanisms that form YMCs at $z = 0$, but resulted in very different, characteristic GC properties due to the extreme environment in their still-forming host galaxies.

Broadly, these theories state that GC formation occurs in the dense, gas rich disks of high-redshift galaxies. Within this turbulent disk, interstellar medium (ISM) thermal instability can lead to the formation of cool, massive gas clouds, surrounded by the hotter ISM gas (Fall and Rees 1985). When these massive gas clouds collapse they create cores and filaments dense enough for star formation to occur, seeding proto-GCs (Kravtsov and Gnedin 2005; Howard et al. 2018; Kruijssen 2025). During this embedded phase stellar feedback begins, eventually allowing the proto-GC to shed its gas envelope and leave behind a newly formed massive GC (Krause et al. 2012; Reina-Campos et al. 2022). Once a GC has emerged it now becomes a game of survival, as the disk of its host galaxy would subject the newly formed GC to tidal perturbations capable of destroying it (Kruijssen et al. 2012; Keller et al. 2020; De Lucia et al. 2024). Thus, in order to survive to $z = 0$, these clusters must migrate to the halo, where the majority are observed today. This migration can occur as a by-product of energy injection from galaxy mergers (Li et al. 2022; De Lucia et al. 2024).

1.1.3 High Redshift Globular Cluster Observations

With the Hubble Space Telescope (HST), and particularly the recent launch of the James Webb Space Telescope (JWST), we are now capable of obtaining observations of proto-GC candidates in the early universe to compare to our theories of GC formation. Using magnification from gravitational lensing we have been able to observe stellar clusters at redshifts from $z \sim 1 - 10$, dependent on the alignment of the galaxies involved (Adamo et al. 2023; Adamo et al. 2024; Vanzella et al. 2023; Claeyssens et al. 2023; Fujimoto et al. 2024; Mowla et al. 2024; Whitaker et al. 2025). In the most extreme case, the Cosmic Gems Arc at $z = 10.2$, we have been able to determine the masses, sizes, and stellar densities of five star clusters hosted by the galaxy, likely the most massive subset of clusters within the larger system (Adamo et al. 2024).

Pfeffer et al. 2025 compared these JWST observations to predictions of proto-GC and host environment properties using the E-MOSAICS simulations. E-MOSAICS incorporates star cluster formation, evolution, and disruption models into the EAGLE galaxy formation simulations (Pfeffer et al. 2018), which in turn are a suite of hydrodynamical simulations following galaxy evolution in a ΛCDM universe (Schaye et al. 2015). They found that, at least for observations of the brightest GCs hosted by these galaxies, their simulations are capable of re-creating the properties we observe, such as relations between cluster mass and host galaxy star formation rate, and cluster mass/luminosity and redshift. Interestingly, they found that if these massive

GCs were to survive to $z = 0$ (which, at initial masses of $10^6 - 10^7 M_\odot$, is plausible) their ages would span from $\sim 9 - 13.5$ Gyrs, implying that GC formation may not take place solely in a specific epoch, but rather over a range of redshifts.

These observations, at the very least, point to GC formation being a process that both begins around the redshift range that has been predicted by modern theory, and which happens *within* host galaxies, rather than outside followed by an accretion event – at least for the bright, massive GCs we are observing. While these first observations and studies are promising, more data and corrections for systematic biases are needed. It will be difficult to draw concrete conclusions on GC formation mechanisms when being limited to observations of only the highest mass populations, however these can still provide valuable insights. In particular, studying the properties of these clusters prior to tidal disruption effects from many Gyrs of residing in their host galaxies, and prior to any major galaxy mergers will be useful to parse out the effects these events can have on GC evolution and the GCS as a whole.

1.2 Globular Cluster System Evolution

Regardless of formation mechanism, by cosmic noon ($\sim z = 2 - 3$) galaxies were populated with GCSs which then evolved over time with their host galaxy. An open question in GCS evolution is just how similar those initial GCSs were to those which we observe today. There are three main drivers of GCS evolution: GC formation, GC disruption, and GC accretion.

All three of these drivers are sensitive to galaxy merger history, as was studied in the simulations of Newton et al. 2024. They simulated the GCSs of three MW-like galaxies with identical $z = 0$ halo masses, but varying merger histories using E-MOSAICS and EAGLE. They found that galaxies that experienced more mergers with higher galaxy mass ratios, at early times experienced enhanced GC disruption and formation rates (see Figure 1.2). These galaxies with enhanced merger histories also had more massive GCSs by $z = 0$ and more top-heavy GC luminosity functions (GCLF) than their counterparts, which experienced less rich merger histories. To understand these results, let us break down the different ways which GCSs can evolve via galaxy mergers.

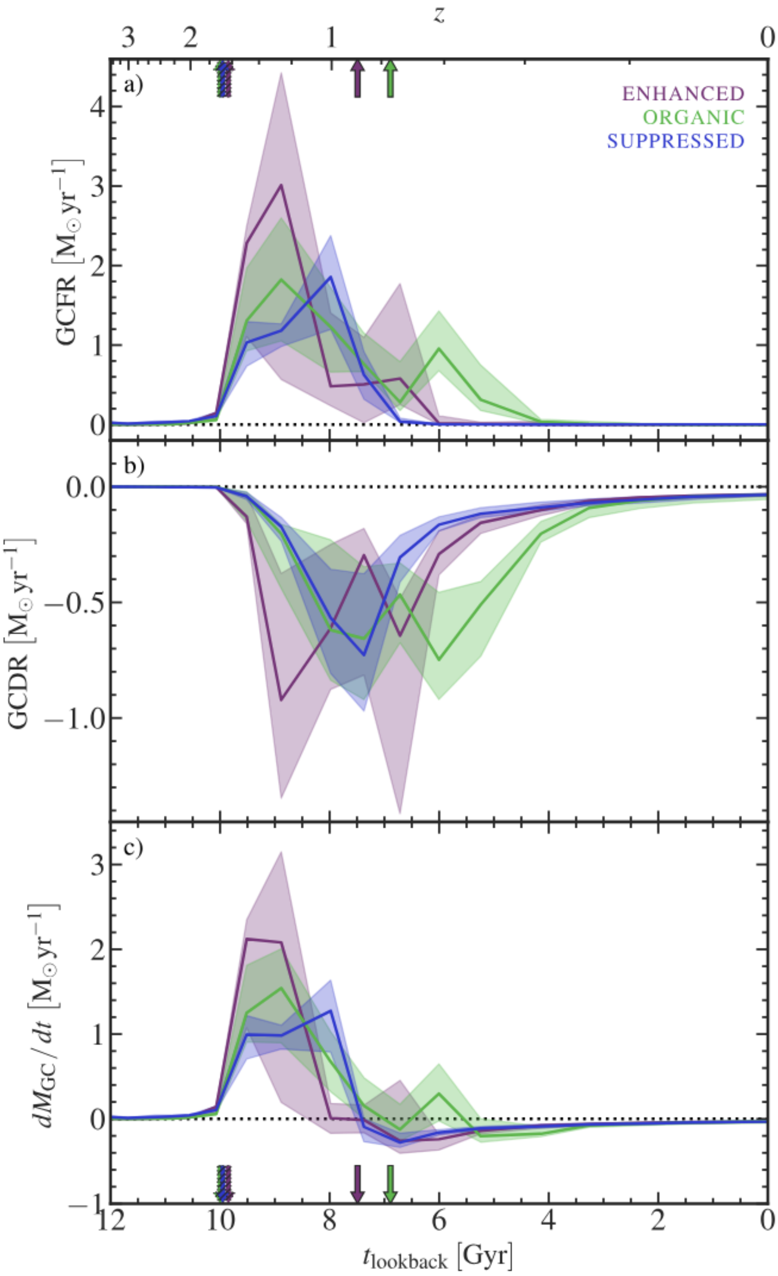

FIGURE 1.2: *Top:* GC formation rate against lookback time, *middle:* GC disruption rate, *bottom:* change in GCS mass vs lookback time, all for three simulated galaxies with the same $z = 0$ mass but different merger histories. Enhanced (purple) has a larger mass ratio, organic (green) is the standard, and suppressed (blue) has the smallest mass ratio and no second merger. The coloured arrows represent the times of the mergers. Reprinted with permission from O. Newton et al. (accessed July 2025). The Formation and Disruption of Globular Cluster Populations in Simulations of Present-Day L^* Galaxies with Controlled Assembly Histories. *Submitted to Monthly Notices of the Royal Astronomical Society.*

1.2.1 Globular Cluster Accretion

First, let us address accretion. Evidence for galaxy mergers being a significant pathway for growth of a GCS can be found in our own backyard – the MW stellar halo (Forbes and Bridges 2010; Massari et al. 2019; Myeong et al. 2019; Limberg et al. 2022; Belokurov and Kravtsov 2024). When comparing chemical abundances, energies, angular momenta and orbits of GCs that make up the MW's GCS we can immediately begin grouping them into different populations. These GCs which formed *ex-situ* (formed not within the main progentior branch galaxy, but rather within a galaxy that has since been accreted) tend to have larger spreads in ages, lower metallicities, and higher energies than their *in-situ* counterparts, as can be seen in Figure 1.3 (Callingham et al. 2022; Malhan et al. 2022). Both observations (Forbes and Bridges 2010; Belokurov and Kravtsov 2024), and simulations (Keller et al. 2020; Kruijssen et al. 2020) show that a significant fraction of the MW GC population was accreted from an *ex-situ* satellite origin, between 25% and 45%.

Although we are limited to unresolved photometry as we look beyond the MW, we can still see clear evidence of merger histories in the GCSs of other galaxies. The majority of intermediate and massive galaxies which have been studied observationally host broad, and sometime clearly bimodal GC colour distributions (Harris et al. 2006; Harris et al. 2017; Fahrion et al. 2020a; Hartman et al. 2023), which is a known tracer of GC metallicity (Brodie and Strader 2006; Usher et al. 2015; Harris 2023; Fahrion et al. 2020b). It has been shown that this colour distribution can be created through rich merger histories, with the bluer, more metal-poor GCs having been formed in smaller parent galaxies that were then accreted by their current host (Choksi and Gnedin 2019; Valenzuela et al. 2024).

We can also observe the positions of these GCs tracing recent merger activity, with blue GC radial distribution profiles having been shown to have more extended and shallow profiles than the red GC profiles in the same galaxy (Kluge et al. 2023; Belokurov and Kravtsov 2024; Veršič et al. 2024). In some rare cases we can also trace out active galactic merger events through the GCSs of the participating galaxies. Ennis et al. 2024 found a bridge of red, metal-rich GCs connecting two merging galaxies (NGC 3640 and NGC 3641), and evidence that the blue, metal-poor GCs' positions were influenced by the same recent merger event which created NGC 3640's shells. Urbano et al. 2024 found that GCs around galaxies and in the intracluster medium of the Dorado group were also capable of physically tracing indicators of galaxy mergers, such as rings, shells, streams, and mass distribution peak offsets.

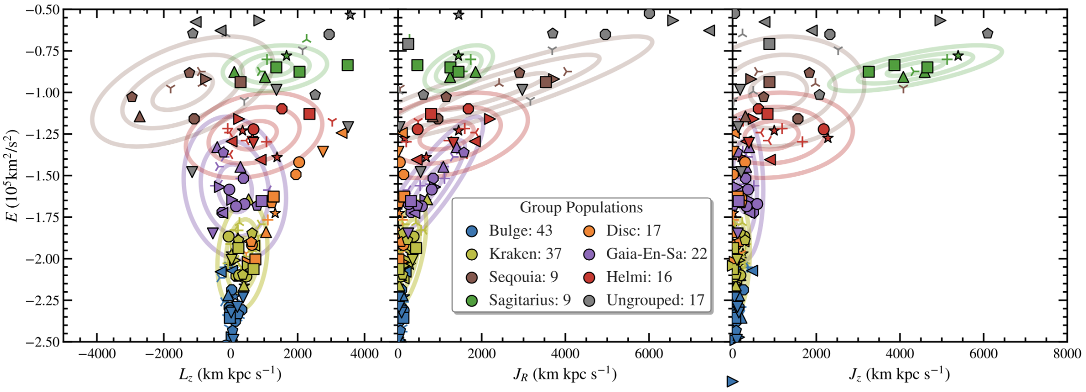

FIGURE 1.3: MW GCs grouped by either progenitor galaxy or MW location in energy-action space. Here action refers to the difference between kinetic and potential energy of the GCs integrated over time. Each subplot has total energy on the y-axis plotted against angular momentum (left), radial action (middle), vertical action (right). Reprinted with permission from T. M. Callingham et al. (Apr. 2022). The Chemo-dynamical Groups of Galactic Globular Clusters. *Monthly Notices of the Royal Astronomical Society* 513(3), 4107-4129.

1.2.2 Globular Cluster Formation via Mergers

If a galaxy merger occurs at early enough times between two gas-rich galaxies, this could also trigger a period of GC formation (Ashman and Zepf 1992; Zepf and Ashman 1993). It is well-known that in the local universe a gas-rich major merger can result in a starburst galaxy which undergoes a period of intense increased star formation (Mihos and Hernquist 1996; Lahén et al. 2022; van Dokkum et al. 2022; Lahén et al. 2025). This has also been recently shown to occur in the early universe as well (Renaud et al. 2022). The same environmental changes that can bring on increased star formation in merging galaxies can bring on increased GC formation as well.

Maji et al. 2017 studied the GC formation efficiency of mergers using high-resolution hydrodynamical simulations. They found that galaxy mergers or strong interactions would lead to intense tidal shocks capable of compressing the galaxies' gas. This would trigger GC formation in the nuclear regions of the mergers and also in areas of high gas density between the interacting and merging galaxies, such as tidal bridges and tails. This has also been studied observationally in the merging Antennae galaxies, where bursts of young massive cluster formation has been identified (Herrera and Boulanger 2017; Tsuge et al. 2021; He et al. 2022).

The most massive galaxies we observe today likely built the majority of that mass through a rich history of hierarchical merging, but mergers are also prominent sources of mass growth for dwarf galaxies as well. GC formation can also be triggered by gas-rich dwarf galaxy mergers, which were common in the early universe (Alavi et al. 2016). Lahén et al. 2019 followed the formation and evolution of massive star clusters in a simulation of a dwarf-dwarf merger. Their clusters formed rapidly following the merger from converging flows of dense gas, capable of reaching masses of $M_\star \gtrsim 10^5 M_\odot$ on a timescale of 6-8 Myrs. The resulting clusters' structures and kinematics are extremely similar to present-day observed GCs, but due to the lower chemical enrichment of the merging dwarf galaxies, these GCs end up also being metal-poor.

These merger events have been shown to significantly increase the specific frequency of GCs for elliptical galaxies compared to their isolated counterparts (Li et al. 2004). It has been suggested that if these mergers occur late enough and between galaxies whose gas has become more enriched since the initial period of GC formation, this second period of cluster formation could also contribute to the spread in GC metallicities observed. Although it was stated in Section 1.2.1 that *in-situ* GCs tend to be more metal-rich than their accreted counterparts, within the MW we still see a spread in matallicities within this *in-situ* sub-population (Belokurov and Kravtsov 2024).

1.2.3 Globular Cluster Disruption

However, galaxy mergers by no means solely contribute to GCS growth, they are dramatic events which can also contribute greatly to GC destruction. For instance, at the time of writing, the MW hosts almost 100 known stellar streams (Mateu 2023), many of which have been identified as originally being GCs hosted by accreted dwarf galaxies (Wan et al. 2020; Bonaca et al. 2021). As GCs fall into a galaxy during a merger event, they are subjected to tidal shocks caused by the sudden increase in surrounding gas density (Gnedin et al. 1999). These shocks can then disrupt GCs, causing mass loss, truncation of their radii, or destruction the clusters entirely (Hughes et al. 2022).

However, this process is sensitive to GC mass, with GC disruption and destruction preferentially affecting lower mass clusters (Kruijssen et al. 2011). In addition, the tidal field that the GCs are moving through will also dictate the survival rate and the average mass of the surviving clusters. Both Villegas et al. 2010 and Harris et al. 2014 observed that the average mass of a GC in a given galaxy scaled with that host galaxy's total mass. This indicates that with larger tidal fields GCs must be more massive to be able to survive infall.

From this picture one might assume that the GCs of isolated field galaxies which have undergone minimal mergers would be safe from disruption. But, unfortunately this is not the case, as internal interactions between GCs and dense galactic disks, or even between GCs themselves, are also capable of causing disruption (Vesperini and Heggie 1997; Dehnen et al. 2004; Miocchi et al. 2006; Peñarrubia et al. 2009). This too is sensitive to GC mass, with larger GCs more likely to survive. Moreno-Hilario et al. 2024a studied the GC disruption and mass loss rates from both interactions with their galactic environments and their own internal stellar dynamics using N-body simulations. They found that dwarf galaxies that underwent no mergers and were not influenced by the tidal fields of any nearby massive galaxies were capable of losing up to 80% of their original GCS mass within a Hubble time, predominantly through the rapid loss of low-mass clusters early in their lifetimes. This however, was also related to host galaxy mass, with the more massive galaxies undergoing a greater GC mass loss rate due to their increased densities and thus increased GC interaction rate.

1.2.4 Globular Cluster Luminosity and Mass Functions

This "survivor bias" caused by GC disruption and formation over time must be considered carefully when studying the GC luminosity function (GCLF) and GC mass function (GCMF) in galaxies, as it can affect the mass distribution of present-day GCs. In general, the GCLF takes on a near-universal unimodal shape, regardless of galaxy morphology (Strader et al. 2006; Jordán et al. 2007; Harris et al. 2014; Lomelí-Núñez et al. 2022; Harris 2023). This GCLF can be well approximated by a log-normal function:

$$\frac{dN}{dm} \propto \exp \frac{(m - m_o)^2}{2\sigma^2} \tag{1.1}$$

Where dN represents the number of globular clusters in an apparent magnitude bin of magnitude m and of width dm, m_o represents the "turn-over" or "peak" apparent magnitude, and σ represents the width of the distribution. If assuming a constant GC mass-to-light ratio (typically taken as $M/L_V \sim 2$ (Bell et al. 2003)), this GCLF can be transformed into a GCMF:

$$\frac{dN}{dM} \propto \frac{1}{\ln(10)M} \exp \frac{(\log(M) - \langle \log(M_o) \rangle)^2}{2\sigma^2} \tag{1.2}$$

Where here dM now represents GC mass bins, M represents GC mass, and M_o represents the average or "peak" GC mass of the population (Harris et al. 2014).

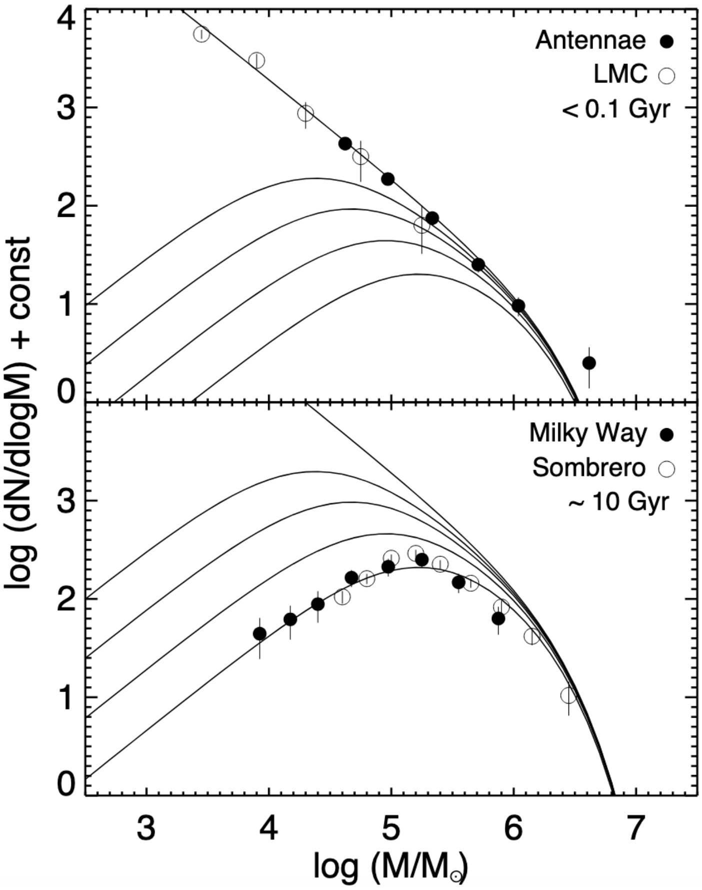

FIGURE 1.4: *Top:* The mass function of YMCs with ages < 0.1 Gyrs in the Antennae and the LMC. *Bottom:* The mass function of old GCs with ages > 10 Gyrs in the MW and the Sombrero galaxy. The smooth curves are from GC formation models with varying GC disruption prescriptions. Reprinted with permission from M. S. Fall et al. (Sep. 2009). New tests for Disruption Mechanisms of Star Clusters: Methods and Application to The Antennae Galaxies. *The Astrophysical Journal* 704(1), 453-468.

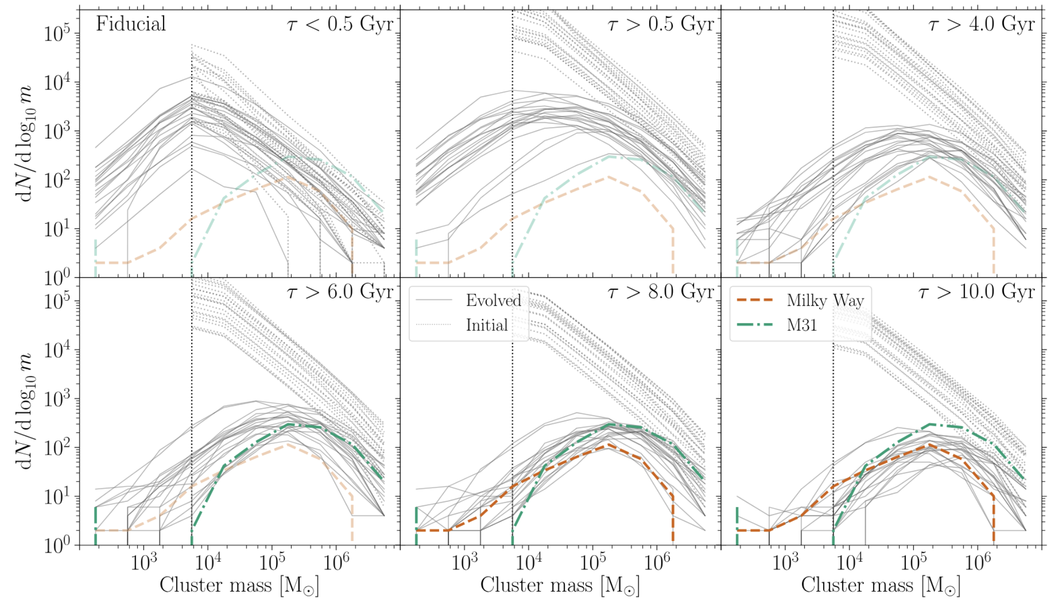

FIGURE 1.5: Mass distributions of EMP-*Pathfinder* stellar clusters bound at z = 0 to the central galaxies. Each panel represents the mass distribution of stellar clusters within an age cut, as indicated in the top-left corner of each panel. The final and initial mass distributions for cluster populations within individual galaxies are shown with the solid and dotted lines, respectively. The red and green dashed lines show the observed GCMFs of the MW and M31, respectively. Reprinted with permission from M. Reina-Campos et al. (Jul. 2022). Introducing EMP-Pathfinder: Modelling The Simultaneous Formation and Evolution of Stellar Clusters in Their Host Galaxies. *Monthly Notices of the Royal Astronomical Society* 517(3), 3144–3180.

While the general shapes of these functions remain largely the same, there has been evidence of a dependence of both turnover magnitude/mass and dispersion on total galaxy luminosity (Villegas et al. 2010; Harris et al. 2013; Harris et al. 2014). For instance, while average GC mass is typically quoted as $\sim 3\times10^5 M_\odot$ for massive spirals (Lomelí-Núñez et al. 2022) and ellipticals (Harris et al. 2014), it can go as low as $1.5-2\times10^5 M_\odot$ for faint dwarf galaxies (Jordán et al. 2007).

This shape of the GCMF is intriguing because the mass functions of recently-formed massive clusters in merging galaxies, like the Antennae, follow a powerlaw distribution rather than a log-normal one, as can be seen in Figure 1.4 (Fall et al. 2009). While we would not expect the mass distributions of YMCs to be the same as GCs for the reasons laid out in section 1.1, it is surprising just how much the the general shape deviates. This implies that this universal GCMF we observe today did not always have this shape, and physical processes may have transformed it into what we see now.

It is possible for this universal log-normal shape to naturally arise from the mass-dependent GC disruption rates discussed in section 1.2.3 (Li and Gnedin 2014; Newton et al. 2024). Lower luminosity GCs would be preferentially destroyed and thus would transform a potential powerlaw initial GCMF into a log-normal one. Both Fall and Zhang 2001 and Prieto and Gnedin 2008 investigated this by evolving GCSs with powerlaw initial mass functions over a Hubble time and varied the cluster disruption mechanisms included in their simulations. They found that including two-body relaxation, tidal shocks, and stellar evolution in their clusters each contributed to their mass loss over time. This mass loss preferentially affected the lower mass GCs as expected, and over time truncated the mass function to eventually re-create the observed peaked log-normal GCMF.

An example of this evolution can be seen in Figure 1.5 from Reina-Campos et al. 2022. In this study they used the EMP-*Pathfinder* suite of cosmological zoom-in Milky Way-mass simulations to study the evolution of GCSs. These simulations used a sub-grid description for GC formation and evolution, allowing them to study both the formation and disruption of GCs within their host galaxies across cosmic time. The results of these simulations painted a similar picture as the comparison of the star cluster mass functions of the Antennae and the MW in Figure 1.4; that GCMFs initially form with a powerlaw shape which is then transformed to a peaked distribution, shifting to higher masses over times as low-mass clusters are preferentially disrupted.

1.3 The $M_{GCS} - M_h$ Scaling Relation

Putting together what has been discussed up to this point, a clear picture begins to emerge; GCS formation, disruption, and evolution is intimately linked to the merger history and environmental properties of its host galaxy. This is demonstrated observationally when comparing the total mass of GCSs (M_{GCS}) to the total mass of their host galaxies, which is dominated by their dark matter halos (M_h).

This scaling relation was first observed by Blakeslee et al. 1997 and was expanded upon by Blakeslee 1999, which found that, for 21 massive elliptical galaxies in 19 Abell galaxy clusters, the number of GCs per unit mass hosted by these galaxies was roughly constant. Several years later, this constant ratio would be predicted to be present for intermediate mass galaxies as well from the numerical simulations conducted by Kravtsov and Gnedin 2005. This would then be observationally confirmed and expanded upon by Spitler et al. 2008, Spitler and Forbes 2009, Georgiev et al. 2010, Harris et al. 2013, Hudson et al. 2014, Harris et al. 2015 and Forbes et al. 2018, each time covering more masses and environments of galaxies and re-confirming the original result: there exists a clear 1:1 linear scaling relationship between these properties, as is shown in Figure 1.6.

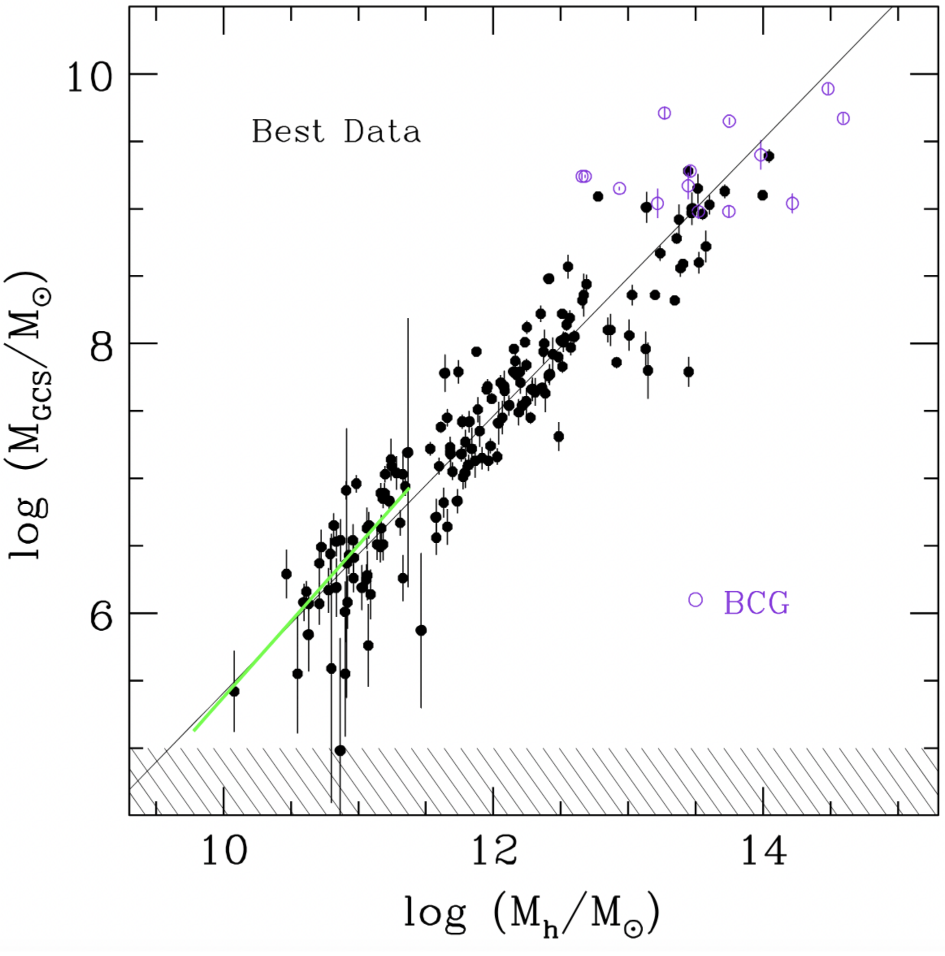

FIGURE 1.6: The observational relation between GCS mass and halo mass for a subsample of 175 galaxies with reliable N_{GC} and M_h estimates. The purple datapoints are classified as BCGs. The green line is the predicted $M_{GCS} - M_h$ relation from Kravtsov and Gnedin 2005. The shaded region is the GCS mass range within which galaxies are expected to host fewer than 1 GC. Reprinted with permission from W. E. Harris et al. (June 2015). Dark Matter Halos in Galaxies and Globular Cluster Populations II: Metallicity and Morphology. *The Astrophysical Journal* 806(1), 36-50.

At first glance this scaling relation might not feel too remarkable, as it makes perfect sense that smaller galaxies would host smaller GCSs and bigger galaxies would host bigger ones. However, this 1:1 linearity is not seen in other scaling relations for galaxy properties that are related to GCS formation and evolution. The stellar to halo mass relation (SHMR), which includes stellar mass hosted not only in GCs but also in other star clusters and field stars, changes slope around $M_\star \sim 10^{10.5}$, making stellar-halo mass ratios lower for more massive galaxies (Hudson et al. 2015; Danieli et al. 2023a). In addition, the relation between the HI gas masses and halo masses hosted by galaxies is also non-linear (Catinella et al. 2010). The varying slopes of these scaling relations arise due to a combination of effects from internal feedback mechanisms and galaxy mergers. For low-mass galaxies, supernova feedback drives internal star formation regulation by expelling gas, and tidal stripping from massive neighbours externally removes star-forming gas, both preventing further stellar enrichment and driving stellar-halo mass ratios down (Koudmani et al. 2022; Collins and Read 2022; Zhang et al. 2024). Massive galaxies' star formation, on the other hand, is mainly regulated by heating, such as active galactic nuclei heating and gravitational infall heating, both preventing gas from reaching low enough temperatures for star formation to occur (Johansson et al. 2009; Weinberger et al. 2017; Scharré et al. 2024). In addition, galaxies with $M_\star > 10^{10.5}$, while growing their halos, tend to lose their low-density gas through major mergers, of which they have experienced many more than their lower-mass counterparts, which also lowers their star formation rates and thus total stellar masses (Spilker et al. 2022; Baker et al. 2023). Despite this, we observe GCS mass increasing in lockstep with halo mass.

It should be noted, however, that in many of these observational studies of the $M_{GCS} - M_h$ relation GC candidates are determined photometrically. Here, GCs are distinguished from other objects by considering their compactness, roundness, luminosity, light profile, and when available, global colours. At these distances these GC candidates are unresolved objects and it is often not possible to obtain accurate age estimates. As a result, some star clusters which have similar masses and compact stellar distributions to GCs but which have intermediate ages (< 9 Gyr) could be photometrically mistaken for GCs. Spectroscopic follow-up observations would yield metallicity measurements which can put constraints on age estimates of these clusters, but it is not possible to obtain these measurements for all clusters. While for many galaxies that are no longer star-forming we can be confident that the majority of clusters we observe are sufficiently old enough to be considered GCs, there can still be a low level of contamination in their N_{GC} estimates. For galaxies which are still star-forming, spectroscopic follow-up observations of identified clusters are even more important.

1.3.1 The Relation for Massive Galaxies

Massive galaxies typically have been able to build up their mass through a more rich hierarchical merger history than their intermediate-mass and dwarf counterparts. This is particularly true for the most massive galaxies in our universe: brightest cluster galaxies (BCGs) which reside at the centres of very dense galaxy clusters, where merger rates are high (De Lucia et al. 2024). Due to their extreme merger histories, BCGs serve as useful tools to study the effect that galaxy mergers have on GCS evolution, and by extent the $M_{GCS} - M_h$ relation.

The distinction between BCGs and non-central massive galaxies can be important, as the evolutionary histories of these galaxies can differ, affecting their GCSs as well. Satellite galaxies experience rapid quenching after infall, with the timescales decreasing for larger host cluster halo masses (Pasquali et al. 2010; Wetzel et al. 2013). As satellite galaxies experience multiple pericentre passes around their central BCG they can also have their dark matter halos stripped (Montero-Dorta et al. 2024; Contreras-Santos et al. 2024). In combination, both of these effects can push massive satellite galaxies lower along the $M_{GCS} - M_h$ relation compared their central counterparts.

BCGs are characterized by their elliptical morphologies and relative lack of gas (Chu et al. 2021). Although it is known that large portions of their GCSs were gained through satellite accretion (Dalal et al. 2021), if a significant enough fraction of their initial gas mass was lost during their early mergers it is possible that their GC formation rate would be suppressed in later mergers. This could increase their halo masses more than their GCS masses and place them lower than linearity on the relation.

This drop in M_{GCS}/M_h ratio for very massive galaxies was predicted by Choksi et al. 2018 and Choksi and Gnedin 2019, but El-Badry et al. 2019a predicted it to continue in linearity instead. Observational studies of the $M_{GCS} - M_h$ relation which covered the BCG mass range also have conflicting results, with Hudson et al. 2014 finding that the most massive BCGs had systematically lower M_{GCS}/M_h ratios, and Dornan and Harris 2023 finding that BCGs continue to follow the 1:1 scaling relation, in agreement with their lower-mass counterparts. Answers to these incongruencies for simulations likely lie in the specifics of the GC formation and disruption prescriptions for BCGs, and for observations the answers likely lie in the methods used to determine GCS membership and masses for BCGs.

1.3.2 The Relation for Dwarf Galaxies

Dwarf galaxies offer their own unique complications to our understanding of the $M_{GCS} - M_h$ relation. Their low masses make them extremely sensitive to the effects of mergers and galaxy-galaxy interactions in GC disruption, but this also makes them more hospitable environments for the survival of low-mass GCs. These factors can cause spread in the $M_{GCS} - M_h$ relation, pushing the population sizes and masses of dwarf galaxies' GCSs both higher and lower, an effect that is exacerbated by the extremely low N_{GC} values already predicted by the relation.

Despite these issues, work done by Georgiev et al. 2010, Forbes et al. 2018, and Gannon et al. 2022, among others, has filled in the observational gaps in our understanding of the low-mass regime of this relation. Overall trends begin to emerge as we see that linearity in the $N_{GC} - M_h$ relation is not possible, as a flattening must occur for galaxies with one or no GCs (with it being obviously physically impossible to have negative numbers of GCs). While many of these non-GC-hosting galaxies have low enough halo masses for this to be a natural outcome of the $N_{GC} - M_h$ relation, many have relatively high halo masses that would result in their lack of GCs making them outliers for the relation (Eadie et al. 2022; Berek et al. 2024). Even for GC-hosting dwarf galaxies, the scatter in the $M_{GCS} - M_h$ relation in this mass regime becomes much higher than for more massive galaxies (Spitler et al. 2008; Harris et al. 2013; Forbes et al. 2018) Simulations of dwarf galaxy GCSs suggest that this scatter could be, in part, because the difference between where a dwarf galaxy was originally situated on the $M_{GCS} - M_h$ relation and where they can now be found could be much bigger than the difference for intermediate mass and high mass galaxies (Munshi et al. 2021; Chen and Gnedin 2024).

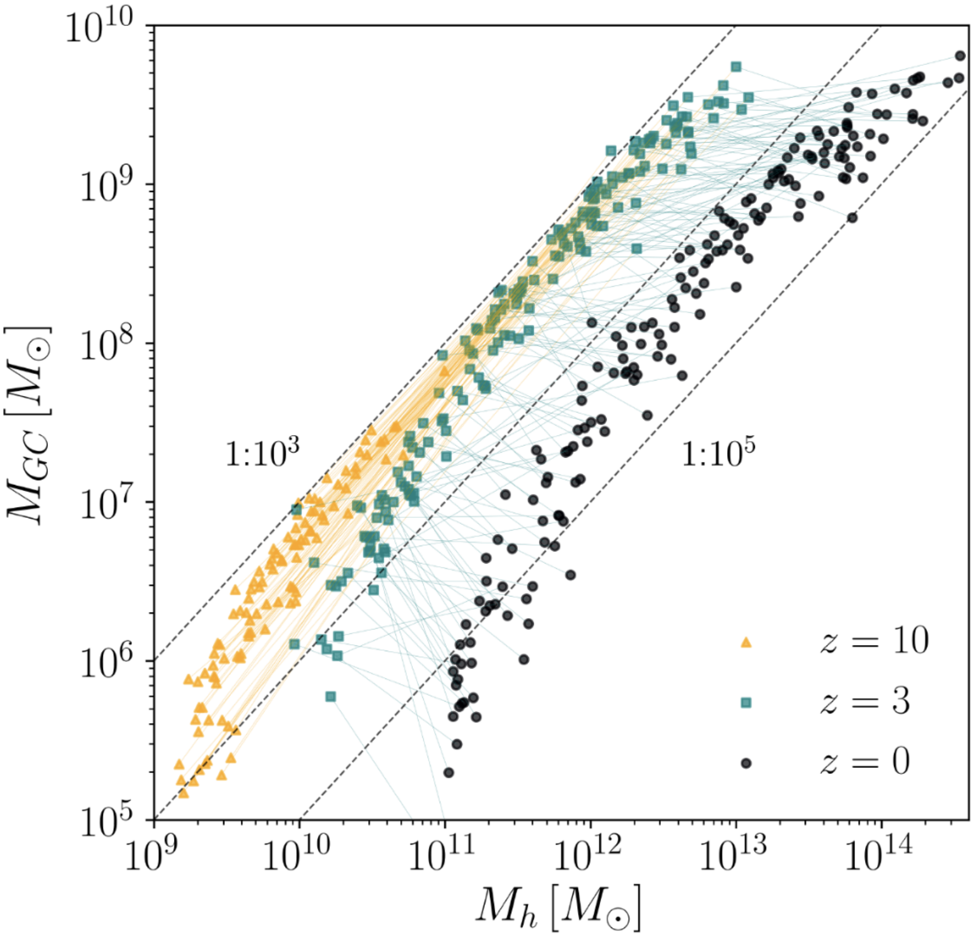

FIGURE 1.7: The positions of a sample of simulated main progenitor branch galaxies on the $M_{GCS} - M_h$ relation, evolved over time including galaxy mergers and GC disruption. Orange datapoints are the galaxies at $z = 10$, green datapoints are the galaxies at $z = 3$ and black datapoints are the galaxies today at $z = 0$. Reprinted with permission from N. Choksi & O. Y. Gnedin (Oct. 2019). Origins of scaling relations of globular cluster systems. *Monthly Notices of the Royal Astronomical Society* 488(4), 5409-5419.

1.3.3 Evolution of The Relation Over Time

As was discussed in section 1.2, while GCs can be disrupted by mergers, for the most part massive GCs are capable of surviving these turbulent merger events and allow galaxies to retain and grow their GCS masses (Choksi and Gnedin 2019; Newton et al. 2024). One question of particular interest regarding this relation is when exactly it took shape, and if it has held this linearity from the formation of the first GCSs or if it has evolved into what we observe today over Gyrs.

Simulations performed by Choksi and Gnedin 2019 found that the overall shape of the relation has been constant across redshifts, although both GCS and halo masses in the early universe were lower (see Figure 1.7). They found that between $3 > z > 0$ galaxies' GCS masses did not change much, but halo masses were an order of magnitude or more lower. Only when they looked further back to a redshift of $z = 10$ did they find that galaxies' GCSs were significantly less massive. This implies that mergers prior to cosmic noon ($10 > z > 3$) would have resulted in both increased halo masses and GCS masses at roughly the same rate, but later mergers would be much more efficient at increasing halo mass while marginally affecting GCS mass. This agrees with what was discussed in section 1.2.2, as mergers would have increased GCS masses much more when galaxies had more gas available at higher densities to allow for periods of increased GC formation.

1.4 Motivation of This Research

This work aims to conduct a comprehensive observational study of the $M_{GCS} - M_h$ relation, from the lowest mass to the highest mass galaxies in the local universe through the compilation of both previously available and new data. Using standardized techniques to determine GC and halo mass estimates, extrinsic scatter in the relation will be minimized, allowing for us to more accurately study the drivers of intrinsic scatter in the relation and their connection to GCS and host galaxy evolution. Through improving the methodology used to determine GCS profiles we will not only have a better understanding of the distribution of GCs around massive galaxies and how that relates to those galaxies' position on the relation, but it will also give us more accurate N_{GC} estimates and therefore positions of these galaxies on the $M_{GCS} - M_h$ relation. Finally, extending this relation to the highest and lowest galaxy masses through the addition of high quality, complete observational samples of GCSs will allow us to test the extremes of this scaling relation.

Chapter 2 will discuss a new technique designed to create more accurate radial density profiles of discrete objects. The application of this technique to GCSs allows for more accurate estimates of GC distribution around galaxies to be made, particularly BCGs, and for more accurate N_{GC} and M_{GCS} estimates to made as well. Chapter 3 places 27 BCGs on the $M_{GCS} - M_h$ relation and studies how various properties of their GCSs relate to their positions on the relation relative to one another and lower-mass galaxies. Chapter 4 compiles a catalog of all dwarf galaxy GCSs studied in the literature and applies standardized conversions for determining GCS mass and halo mass to more accurately compare data from different studies to one another.

Armed with data spanning from the most massive giants to the smallest dwarfs this work will analyze what are the most influential drivers of GCS evolution and how they relate to galaxy evolution as a whole. Finally, Chapter 5 will summarize the results and lay out the future of this field and what the next steps are for fully understanding the connection between GCs and their host galaxies.

Chapter 2

Utilizing Voronoi Tessellations to Determine Radial Density Profiles

The following chapter has been published in The Astronomical Journal (AJ):

V. Dornan and W. E. Harris (Aug. 2024). Utilizing Voronoi Tessellations to Determine Radial Density Profiles. *AJ* 168(2) 48, 48

2.1 Introduction

Determining the radial density profiles of a variety of astronomical systems that consist of discrete objects is a frequently encountered problem within the field. Prominent examples may include stars within a star cluster (King 1966; Miocchi et al. 2013), systems of globular clusters (GCs) within their host galaxy (Harris et al. 2015; Dornan and Harris 2023), or galaxies within a larger group or cluster (Nagai and Kravtsov 2005). Thus, in order to get accurate estimates of the central concentration, profile shape, and total number of objects within a system it is necessary to have an accurate fit to the projected radial density profile.

Observationally, the classic method to determine these radial density profiles is to first determine the 2-dimensional spatial distribution of objects from photometric observations, then divide this spatial distribution into a series of concentric circular or elliptical annuli, effectively binning the objects as a function of radius. For each of these bins the number of objects and the area of the bin's annulus are determined in order to obtain a density value. These density values are then plotted as a function of radius to which a density profile can then be fit. This method had been applied observationally to stars in open star clusters (e.g. Alfonso and García-Varela 2023; Bisht et al. 2024; Belwal et al. 2024), stars in GCs (e.g. Knödlseder 2000; Dalessandro et al. 2015; Simpson et al. 2017), systems of GCs around galaxies (e.g. Harris et al. 2015; Harris et al. 2016; Harris and Mulholland 2017a; Dornan and Harris 2023; Caso et al. 2024; Ennis et al. 2024), galaxies within galaxy clusters (e.g. Popesso et al. 2007; Newman et al. 2013; Fassbender et al. 2014; Tozuka et al. 2021), and compact radio sources at the centre of the Galaxy (Zhao et al. 2022).

This annulus fitting method is useful in its simplicity, but has some drawbacks. The systems to which it is applied can have thousands of detected objects within this spatial distribution (Peng et al. 2008; Peng et al. 2011; Harris et al. 2016; Dornan and Harris 2023), which when binned, are reduced to only a few datapoints, resulting in a loss of information about the system, and uncertainty in the fit. In addition, the number of these binned annuli, and by extension the radial width they encompass, is arbitrary, which can introduce further uncertainty in the resulting fit. Finally, as well the annulus method prescribes a geometrically regular (circular or elliptical) density distribution, smoothing over substructure such as satellites or local overdensities.

This work introduces a different general methodology using Voronoi tessellations for determining radial density profiles. Voronoi tessellation plots are constructed from a spatial distribution of points, and each tessellation (Voronoi cell) consists of the area of the distribution that is closer to the given point than the other points (Okabe et al. 1992). The result is a distribution of polygons each containing one of the objects from the input spatial distribution. See Figure 2.1 for a simple example of a 2D Voronoi tessellation plot.

The tessellation process allows for construction of the density distribution, since the area of a Voronoi cell is directly related to the local number density of objects surrounding the cell. Higher density regions will produce Voronoi cells with smaller areas, and lower density regions will produce Voronoi cells with larger areas. Thus, once a Voronoi tessellation plot has been created from a spatial distribution of objects, the area of each cell can be inverted to obtain a density value for each object. Dividing the region into Voronoi cells is a binning process like the standard annular method, but it essentially carries the definition of bin size to its minimum possible extreme, with one object per bin. In addition, unlike the classic annulus method, the

Voronoi method makes no assumptions about any geometric regularity in the spatial distribution.

It should be noted however, that in order to determine surface density using both annuli and Voronoi tessellations, a distribution of discrete objects is required. Neither of these methods can be applied to, for example, surface brightness profiles.

Voronoi tessellations have been applied to the determination of spatial densities in astronomical research in the past, as they can be very useful in describing the spatial distribution of observed galaxies, which can exist in areas of over and under densities (van de Weygaert and Icke 1989; Icke and van de Weygaert 1991). Voronoi tessellations have also been used in algorithms to automatically detect these over-densities, galaxy clusters, from 2D galaxy field spatial distributions (Ramella et al. 2001).

In the present paper, we test this Voronoi-cell method against simulated radial distributions of populations following a simple input distribution (a Hubble model profile), and compare the results with the standard annular-bin method. The data used to test this new Voronoi method will be discussed in section 2.2. This section will describe the simulated 2D Hubble distributions and test the method's ability to return the input radial density profile, compared to the annulus method. Section 2.3 will further describe the Voronoi method in detail and the statistical tests used to compare it to the annulus method. Section 2.4 will summarize the results of these statistical tests and outline the benefits of the Voronoi method for determining radial density profiles. Finally, section 2.5 will provide a sample application to observed systems and discuss future applications of this method and improvements that can be made.

2.2 Data

In order to test the ability of both the annulus fitting method and the Voronoi fitting method to accurately return the true radial density profile of a 2D spatial distribution of objects, a series of artificial systems were created with known Hubble profiles, defined by

$$\sigma = \sigma_0\Big(1 + \frac{r}{r_0}\Big)^{-b} \tag{2.1}$$

where σ_0 is the density at $r = 0$, r_0 is the core radius, and the exponent b sets the power-law slope of the profile at large radius.

We generated simulated systems with five different total populations, The properties of which are detailed in Table 2.1 (The scale units are arbitrary, but are simply labelled as 'pixels' for convenience). The spatial distribution of objects for each of these systems was generated with 30 different random seeds each, allowing for each system to be tested with the same underlying Hubble distribution but varying positions of objects.

The parameters for the artificial systems were chosen building from our previous work on the estimated properties of a sample of observed GC systems hosted by massive elliptical galaxies. These galaxies have already had the radial density profiles of their GC systems determined with the annulus fitting method in Dornan and Harris 2023, hereafter referred to as Paper I. The parameters of the simulated systems were chosen to reflect the range of profiles seen in a real-life application of this methodology.

It should be noted that in this initial study the Voronoi method is tested only on circularly symmetric systems, although does not make any assumptions on the underlying symmetry of the system. This decision was made because the annulus method, to which we are directly comparing the Voronoi method, does. In followup work, the Voronoi method will be extended to systems where one or more satellites are present, with their own subpopulations of objects, in order to investigate the technique's ability to handle asymmetrical systems.

TABLE 2.1: Artificial System Hubble Profile Parameters

System Number (1)	Objects (2)	Core (pixels) (3)	b (4)	r_{max} (pixels) (5)	σ_o (pixels^{-2}) (6)
1	300	75	1.5	3250	8.83×10^{-4}
2	2000	150	0.96	3250	6.93×10^{-4}
3	4500	150	0.96	3250	1.56×10^{-3}
4	7000	250	1.09	3250	2.05×10^{-3}
5	20000	250	1.09	3250	5.86×10^{-3}

Key to columns: (1) Artificial system identification; (2) number of objects in the system; (3) size of the core of the Hubble profile in units of pixels; (4) exponent of the Hubble profile; (5) maximum radius objects can be from the centre of the spatial distribution in units of pixels; (6) density at $r = 0$ of the Hubble profile in units of objects per pixel^2.

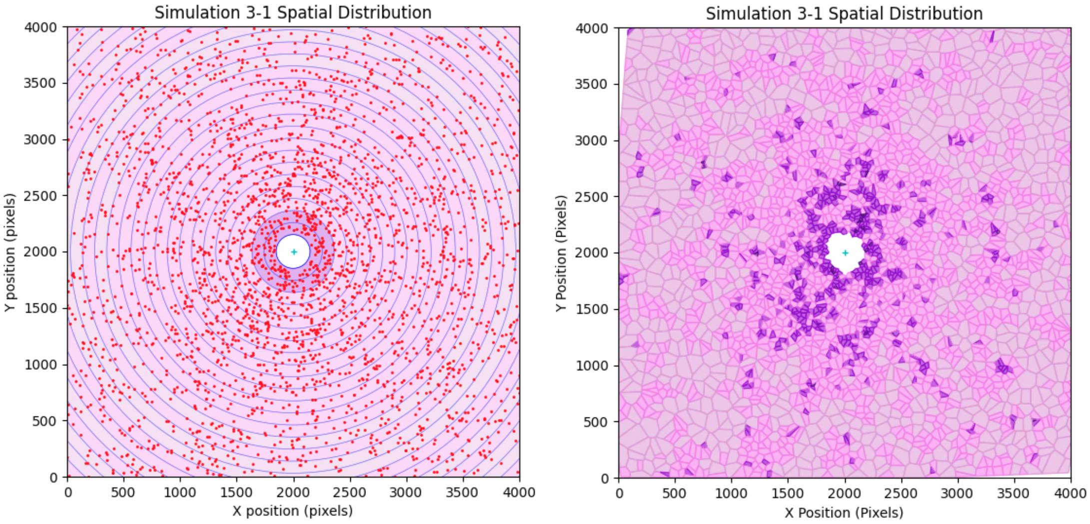

Figure 2.1: *Left:* The 2D spatial distribution of objects with concentric annuli drawn out from the centre of the system. These annuli are used to bin the objects and determine densities as a function of radius. *Right:* The Voronoi Tessellation plot for the same 2D distribution of objects, with one object per cell. For both plots cell colour represents comparative density on the same scale.

2.3 Methods

2.3.1 Annulus Fitting Method

As noted above, annulus fitting is a standard binning method used to determine radial density profiles of a variety of circularly and spherically distributed systems, both simulated and observed (King 1966; Nagai and Kravtsov 2005; Miocchi et al. 2013; Dornan and Harris 2023; Alfonso and García-Varela 2023).

An example of a 2D spatial distribution of objects divided into concentric annuli can be seen in Figure 2.1, which is for simulated system number 3. These binned densities can then be plotted as a function of radius and a simple fitting function such as a power law or Sersic profile can be fit to it.

For these simulated systems the number of annuli was always set to 26 and the bin widths determined from the range of radii encompassing the innermost and outermost objects. However, often the 1-2 outermost bins had to be removed for incompleteness, as often the final few annuli would only host a very low number of objects and areas. This can be seen in Figure 2.1 in the corners of the annulus distribution.

2.3.2 Voronoi Fitting Method

The Voronoi fitting method is capable of retaining far more information about the system than the annulus fitting method through the use of the Voronoi tessellations. When a Voronoi cell is generated around each object in the system, the number of datapoints is equal to the number of objects within the system. A density value for each datapoint, at the radius of each object, is determined by simply inverting the area of the Voronoi cell.

In practice, the resulting plot of density versus radius for one object per cell displays the desired profile, but is also dominated by large stochastic scatter. A useful approach to reduce the scatter is simply to combine adjacent cells into larger combined ones. We have experimented with grouping 3, 5, or 7 cells together compared to no grouping at all, as shown in Figure 2.2. Binning the Voronoi cells to have five objects per cell proved to be an excellent compromise between significantly reducing scatter and keeping a large number of independent datapoints.

An alternative approach to grouping cells would be to combine a given cell with all its adjacent cells (i.e. those whose sides are in direct contact). However, for a typical Voronoi tesselation, approximately 89% of all cells have 6 or more adjacent cells (see Table 1 of Suârez-Plasencia et al. 2021). Thus the majority of cells in the distribution would be binned in groups of 7 or more, which, as previously mentioned, was found to result in too strong an averaging and greater culling of datapoints.

Combining cells was done by sorting the cells by density, from highest to lowest. The highest density cell in the list then has the four spatially closest objects to it identified, and all five are added into a single bigger cell and removed from the initial list. This new cell is assigned an (x, y) position in the grid that corresponds to the averaged positions of the five member objects, and an area equal to the combined areas of the original cells. The rest of the binning continues in the same way for the next highest density individual cell in the list. This procedure ensures that the objects that are being binned together are spatially close to one another and prevents situations where the last two objects are on opposite sides of the system, or oddly shaped ("gerrymandered") combined cells are created.

Binning the cells together not only reduces scatter, but also reduces a particular statistical bias that is associated with Voronoi tessellations. A tessellation of a random, *spatially uniform*

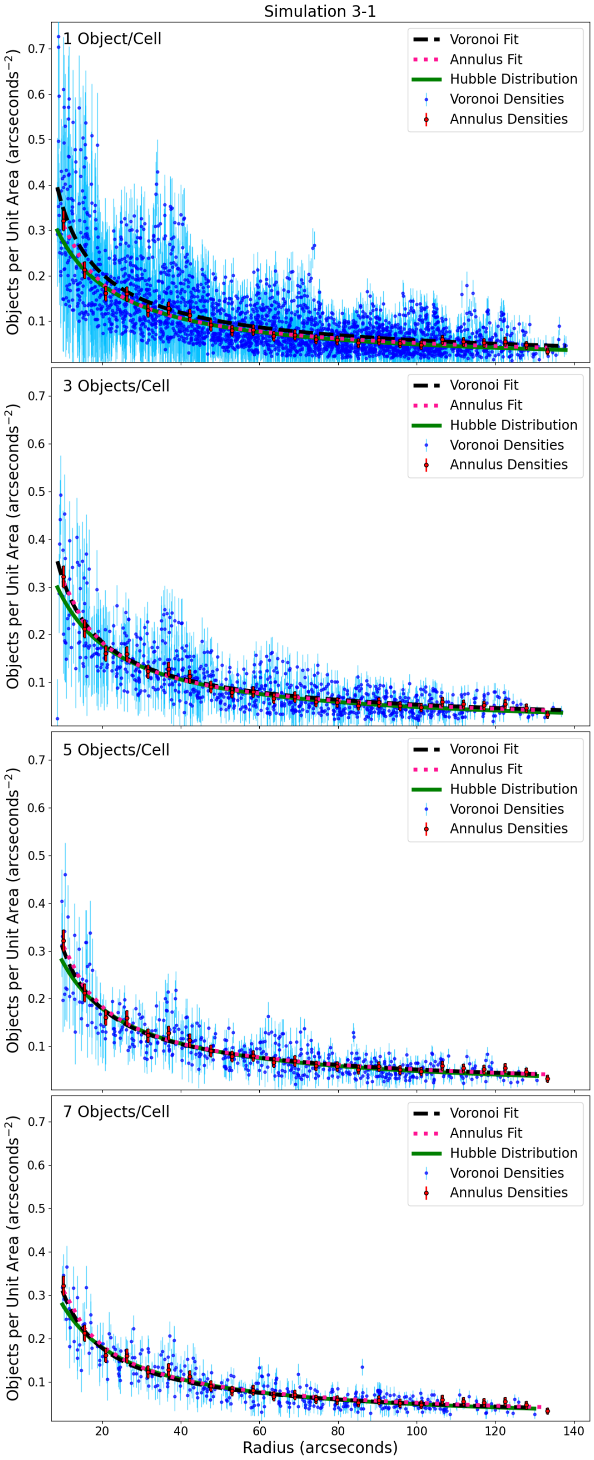

FIGURE 2.2: Sample radial profile showing the radial density distributions for 1, 3, 5, and 7 objects per cell (going from top down). All annulus data and fitting is identical, as it is independent from the Voronoi fitting.

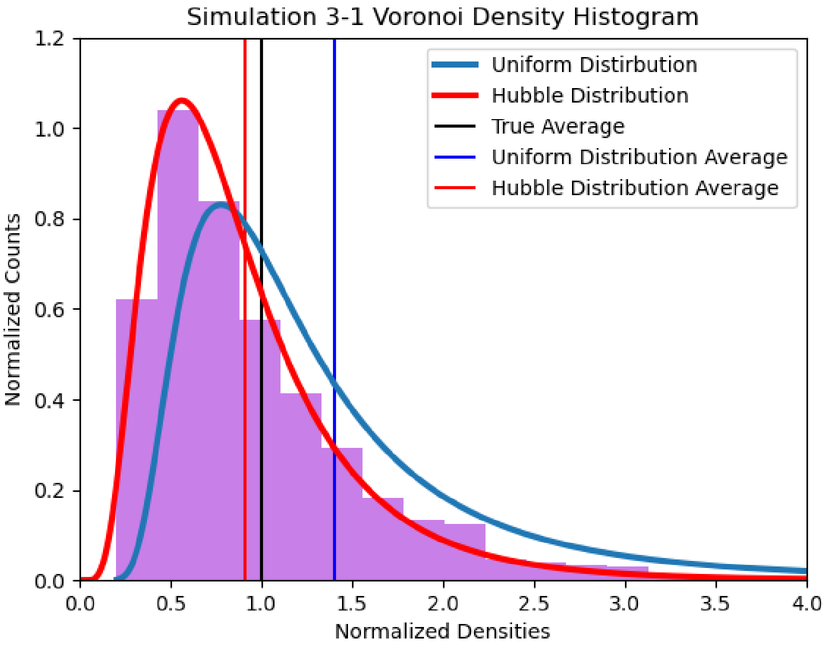

FIGURE 2.3: A histogram of the normalized density of Voronoi cells for a Hubble distribution. The red curve is the log-normal fit to the histogram and the red line is the average for the Hubble distribution. The blue curve is the fit to the histogram for a uniform distribution and the blue line is average for the uniform distribution. The black line is the mean normalized number density, where $x = n/\langle n\rangle = 1$ when $n = \langle n\rangle$ for all distributions.

2D distribution of objects can be described (Jarai-Szabo and Neda 2004) as

$$f_{2D}(y) = \frac{343}{15}\sqrt{\frac{7}{2\pi}}y^{5/2}\exp\Big(-\frac{7y}{2}\Big) \tag{2.2}$$

where y is the normalized cell area, S, as $y = S/\langle S\rangle$. This distribution for cell size can be transformed into a distribution for a number density (n) distribution for each cell. Here we will take $x = n/\langle n\rangle = 1/y$ to be the normalized number density. The 2D number density distribution for a uniform spatial distribution of objects is

$$f_{2D}(x) = \frac{343}{15}\sqrt{\frac{7}{2\pi}}x^{9/2}\exp\Big(-\frac{7}{2x}\Big) \tag{2.3}$$

For this distribution the mean value of the probability density function does not equal the mean normalized number density, $x = n/\langle n\rangle$. It is instead 1.4 times the mean normalized number density, indicating that, for a uniform spatial distribution, Voronoi tessellations tend to overestimate the influence of high density areas for the overall system. This can be seen in Figure 2.3 when comparing the blue curve, which corresponds to Equation 2.3, and the blue vertical line, which represents the curve's mean, to the black line which is the expected mean value, where $n = \langle n \rangle$ and $x = 1$.

However, for the purposes of this work we are not concerned with the number density bias for a uniform distribution, but rather for a distribution following a power-law-like radial profile. When the normalized number density distribution is plotted as a histogram for the artificial systems in this work, the distribution can instead be described by a log-normal distribution, taking the form:

$$f_{2D}(x) = \frac{1}{xa\sqrt{2\pi}} \exp\left(\frac{(\log x - b)^2}{2a^2}\right) \tag{2.4}$$

Where a and b are free parameters. This can again be seen in Figure 2.3, where the red curve corresponds to Equation 2.4 and the red vertical line represents this curve's mean.

For a Hubble distribution, the average number density of the cells, after binning into groups of five, is actually 0.90 times the mean normalized number density. This statistical underestimation of the average number density of the Voronoi tessellations was found to be small enough that it has a negligible effect on the radial density profile fits. As will be seen below, the over- and under-estimations of the density profile at various radii due to simple randomness across the systems studied were consistently greater than the influence of this statistical bias, so at this time it is ignored.

2.4 Results

Table 2.2: Bootstrapped Powerlaw Fits with Standard Errors

System Number	Annulus Method	Voronoi Method
1	$\sigma = (1.131 \pm 0.110)r^{(-1.360 \pm 0.021)}$	$\sigma = (1.184 \pm 0.084)r^{(-1.370 \pm 0.020)}$
2	$\sigma = (0.852 \pm 0.035)r^{(-0.794 \pm 0.010)}$	$\sigma = (0.849 \pm 0.029)r^{(-0.784 \pm 0.007)}$
3	$\sigma = (1.899 \pm 0.040)r^{(-0.782 \pm 0.006)}$	$\sigma = (1.704 \pm 0.012)r^{(-0.753 \pm 0.002)}$
4	$\sigma = (2.637 \pm 0.127)r^{(-0.757 \pm 0.010)}$	$\sigma = (2.765 \pm 0.011)r^{(-0.758 \pm 0.001)}$
5	$\sigma = (7.377 \pm 0.244)r^{(-0.747 \pm 0.008)}$	$\sigma = (8.726 \pm 0.013)r^{(-0.780 \pm 0.0004)}$

These fitting parameters and standard errors were obtained from 5000 iterations of bootstrapping for both methods.

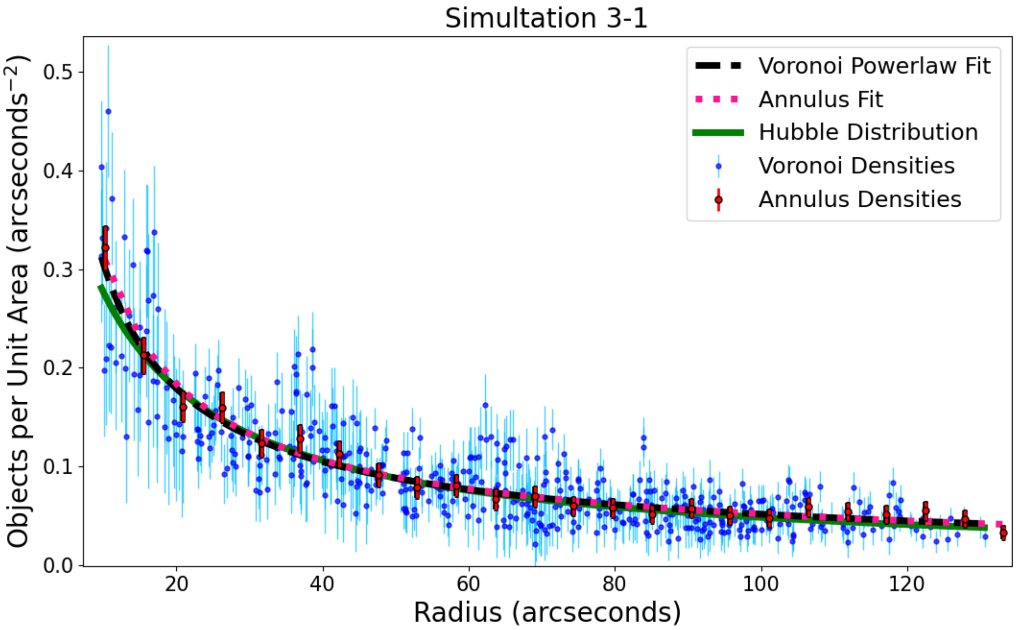

Figure 2.4: The density data for the same system using the annulus fitting method (red datapoints) and the Voronoi fitting method (blue datapoints). Both datasets are fit with a powerlaw function and compared to the “true” Hubble profile (green line).

For each run of each system the density profiles were determined both with the annulus method and the Voronoi method. This created two different radial density datasets from the same underlying Hubble distribution. For both the annular and Voronoi methods, objects within the core of the system (defined in table 2.1) were removed. This is because in real observations of systems of globular clusters the background light intensity within the core of the central galaxy is typically high enough that identification and measurement of objects in the core cannot be done (Harris et al. 2015; Harris et al. 2016; Harris 2023; Dornan and Harris 2023; Ennis et al. 2024). Thus, these objects have been removed for the analysis in order to better re-create the data available for a real astronomical system, to which this method will be applied in section 2.5.1.

Figure 2.1 shows the spatial distribution of the simulated objects and a visualization of the density fitting method used. Once the objects have been binned according to the methods used their densities can be plotted as a function of radius and have profiles fit to them. Here the radii and densities have been converted from pixels to “arcsecond” according to HST ACS camera pixel conversions, defined as 1 pixel width = 0.05 arcseconds (Ryon 2019), again to better reflect observed data. The uncertainties associated with the annulus fitting method density values assume $\sqrt{N}$ statistics.

The uncertainties of the density values from the Voronoi fitting method were determined from the root mean square scatter around a powerlaw fit to the densities as a function of radius, for 10 radial bins. This allows the decreasing uncertainty in cell density to be reflected in the voronoi cells, as is seen for the annulus bins. Once the uncertainty for each radial bin was determined it was applied to all density values in that bin.

Once the uncertainties for both methods are determined the Voronoi fitting method density values were culled to remove outliers. This is done by determining the average Voronoi density value for the same number of radial bins as was used for the annuli (although the average Voronoi densities in these bins are slightly different than the annuli density values). All Voronoi density values that are within 1.5 standard deviations of these radially binned means are kept, and all others are culled. The percentage of cells kept after culling varied for system and run, but was roughly 85%.

In the case of this work, although the distribution was created according to a Hubble profile, the densities are fit with a simpler powerlaw function due to the lack of information within the core. These fits can then be compared to the "true" Hubble profile to determine which method returns the more nearly correct density profile. An example is shown in Figure 2.4. If this Voronoi method was applied to, for example, a single GC, a Hubble profile could then be used to fit the data as the information in the core would be available.

In order to compare the effectiveness of these two methods of determining radial profiles there are two important factors to examine: the methods' precision, and their accuracy. For the precision we compare the uncertainties of the fits to the data, while for the accuracy, we compare the total numbers of objects integrated over all radii relative to the input number.

The uncertainties on the fits to the profiles of all systems with both methods were determined via bootstrapping. The radial density data for both methods was bootstrapped with 5000 iterations for each system, and powerlaw profile fitting values were determined, as well as their standard deviations. The uncertainty for each of these fitting values, the standard error, defined here in Equation 2.5, was determined from the standard deviations.

$$SE = \frac{\sigma}{\sqrt{n}} \tag{2.5}$$

Here σ is the standard deviation of the scatter of points around the fitted curve, and n is the length of the dataset used to determine the fitting parameters.

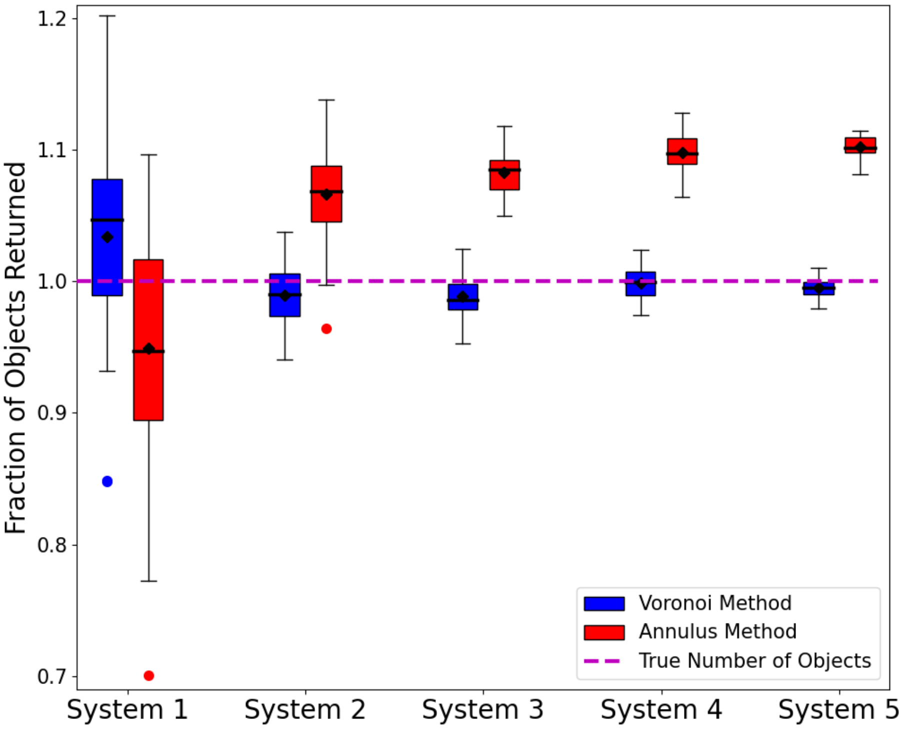

FIGURE 2.5: A boxplot depicting the results of the number of objects in each system returned when the radial density profile obtained from each method is integrated, done across all 30 random object distributions for each system. The dashed line shows where 100% of all objects are returned. The boxes represent the interquartile range (IQR), the black lines within the boxes denote the medians, the diamonds denote the means, and the errorbars encompass all non-outlier data that lie outside the IQR. The coloured circles represent outliers, defined as data that lie greater than 1.5 times the IQR past the upper and lower quartiles.

In an ideal case, even when the total number of objects in the system is not completely observed, as in the case of the inner regions of these simulated systems seen in Figure 2.1, if the fit is accurate and integrated from zero to the system's maximum radius it should return the true number of objects. This was done for each run of each simulated system, and the results are displayed in Figure 2.5 as the total number of objects returned by the fit, relative to the total input number over the same radial region.

2.5 Discussion

It can be seen from Figure 2.5 that the Voronoi method is more successful at returning a total population that is close to the input total. For systems 2 through 5 the Voronoi method's upper quartiles enclose or very nearly enclose the true number of objects. For these same systems however, the lower quartiles of the annulus method lie much further from the true number of objects, and for systems 3 through 5 the true number of objects is not even within their lower range. This shows that, certainly for larger systems of 2000 objects or more, the Voronoi method will more consistently and more accurately return the true number of objects.

Across Figure 2.5 we can see that the spread in both methods decreases with increasing system size. Thus, for system 1, the smallest system in this work, the spread for both methods is significantly higher than for the other systems. But even for the smallest system the Voronoi method still returns a slightly more accurate result, with both its mean and median lying closer to the true number of objects returned than for the annulus method (0.949 and 0.947 compared to 1.033 and 1.047, respectively).

The radial profile fits for each system using each method are listed in Table 2.2. The precision of each of these methods is compared via the uncertainties on the fitting parameters for each method. As can be seen in Table 2.2, the Voronoi method consistently returns lower uncertainties on both powerlaw fitting parameters for all systems studied. As system size increases so too does the difference in method precision, with the parameter uncertainties for system 1 being comparable between methods, to systems 4 and 5 having uncertainties differing by an order of magnitude.

2.5.1 An Application to Observed Distributions

Here we present a comparison of these two methods when applied to real, observed GCSs, for which a definition of the "true" underlying radial density profile is unknown. A common problem in many observed cases is that giant galaxies may have nearby satellites with their own GCSs,

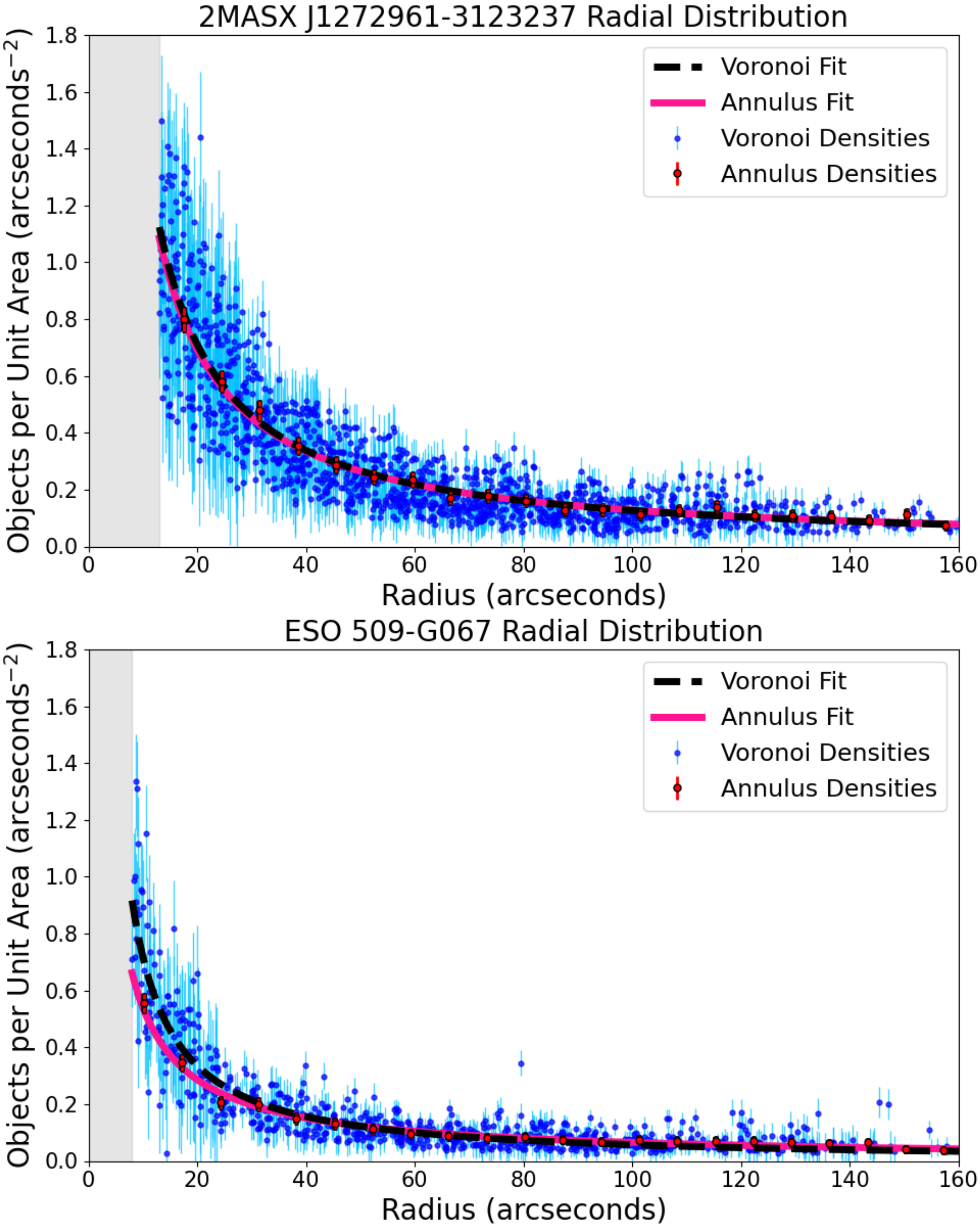

FIGURE 2.6: The density data for the observed GCSs MASX J13272961-3123237 (top) and ESO 509-G067 (bottom) using the annulus fitting method (red datapoints) and the Voronoi fitting method (blue datapoints). Both datasets are fit with a powerlaw function. The gray shaded region is unobservable due to high surface brightness.

which can overlap the GCS of the central giant (Dornan and Harris 2023; Ennis et al. 2024; Lim et al. 2024). We will return to this separate problem in followup work.

For the purposes of this paper we will focus on two observed examples with minimal satellite interference. The GCSs chosen for this comparison are those hosted by the BCGs 2MASSX J13272961-3123237 and ESO 509-G067. Their GCS radial density profiles have already been determined with the annulus method in Paper I, and have few significant satellite galaxies. The comparison of these two methods, applied in the identical way as for the simulated systems, can be seen in Figure 2.6. From the work done in Paper I 2MASSX J13272961-3123237 is estimated to have a GCS population of 9100, and ESO 509-G067 to have a GCS population 4200, putting them in terms of size close to systems 3 and 4 simulated in this paper.

The radial density fits to these observed GCSs, and the uncertainties on these fits, using both methods are shown in table 2.3. The number of GCs in the GCS and the total mass of the GCS obtained from using these fits are shown in table 2.3 as well, using the same methods and photometric completion corrections as Paper I.

While no statement can be said about the comparative accuracies of these two methods when applied to observed systems, it can be seen in Figure 2.6 that the fits agree well. This is as expected as for ESO 509-G067, as for a system of this size it was found in Table 2.2 that the fitting parameters between both methods agree within uncertainties. However, the fits between methods for 2MASSX J13272961-3123237 agree strikingly well, and is not something that is expected from the simulations for a system of its size. The further application of these methods to extremely massive observed systems is needed, and plans for this is discussed in Section 2.6.1.

The estimates of the populations themselves are roughly consistent with what we would expect based on the results from Figure 2.5, within their uncertainties. For the larger system, 2MASSX J13272961-3123237, the annulus method returned a higher estimate than the Voronoi method, albiet with much less a dramatic difference than expected, as was seen for system 4. For ESO 509-G067, its size would make it roughly comparable to systems 2 and 3, and although the Voronoi method actually returned a higher estimate than the annulus method, within the uncertainties of the two methods, this is still be consistent with the results from Figure 2.5.

Overall, for both of the returned GCS values for both galaxies in Table 2.3 both methods return estimates within their mutual uncertainties. However, the Voronoi method still returns estimates with lower uncertainties, indicating that this method is capable of more precise estimates.

2.6 Conclusions

This work develops a new methodology to determine radial density profiles of a variety of astronomical systems of discrete objects using Voronoi tessellations. Our main conclusions are as follows:

- This Voronoi method was tested and compared to the classic annulus method for five simulated systems of varying sizes and steepness of known Hubble profiles, each run 30 times with different random seeds. These systems were chosen for their similarities to observed GCSs.
- It was found that for all five systems the standard errors on the fits found with the Voronoi method were lower than for the fits found with the annulus method, indicating that the Voronoi method returns more precise fits regardless of system.
- It was found that the Voronoi method returned more accurate estimates of the total population of all five systems than the annulus method. The spread in potential population estimates decreased for both methods with increasing system size. For systems of roughly more than 1000 objects the annulus method overestimated the total population by approximately 10%, while the Voronoi method consistently returned estimates at or within 3% of the true value.
- When these methods were applied to two observed GCSs it was found that the radial density profile fits produced by the two methods were very similar and the total N_{GC} estimates were within both methods' uncertainties. However, the uncertainties on both the fits and the N_{GC} estimates for both observed systems were lower for the Voronoi method than for the annulus method.

Table 2.3: Comparison of Annulus and Voronoi Methods on Observed Galaxies

Galaxy	Value	Annulus Method	Voronoi Method
J13272961	Powerlaw	$\sigma = (16.1 \pm 1.5) r^{(-0.92 \pm 0.03)}$	$\sigma = (16.6 \pm 0.8) r^{(-0.93 \pm 0.01)}$
	N_{GC}	9055 ± 1173	8885 ± 793
ESO 509-G067	Powerlaw	$\sigma = (4.5 \pm 0.5) r^{(-0.92 \pm 0.03)}$	$\sigma = (5.2 \pm 0.02) r^{(-0.93 \pm 0.01)}$
	N_{GC}	4174 ± 726	4632 ± 471

2.6.1 Future Work

Future work with this new method of radial density profile fitting will include its application to more observed systems of varying sizes. Currently the authors of this paper plan to apply this method to the remaining GCSs studied in Paper I, as well as 17 additional BCGs imaged with the HST.

Further improvements to this method also include the ability to accurately remove objects associated with nearby systems. As briefly mentioned in section 2.5.1, observed GCSs often have nearby satellite galaxies with their own GCSs which can contaminate radial density profile estimates of the target system. The current method of removal of these contaminating systems is to simply mask out any objects suspected to not belong to the target system (Dornan and Harris 2023; Lim et al. 2024), or even to simply leave the contaminating system if it is small enough to not have a drastic affect on the target system (Harris et al. 2015; Harris and Mulholland 2017a). This method can lead to objects associated with the target system being removed, or missing various objects associated with the contaminating system.

With the increase in spatial density data associated with the Voronoi method compared to the annulus method, it is possible that the radial density profile of the contaminating system, and its influence on the estimated profile of the target system, cam be determined and subtracted from the target system's fit. This would not only give a far more accurate estimate of the profile for systems in dense, clustered environments, but would also allow for an estimate of the smaller contaminating system's radial density profile. This can be particularly helpful in situations where the GCS distributions of two interacting galaxies is trying to be studied (Ennis et al. 2024). Work on developing this method is in progress.

Chapter 3

Major Mergers Mean Major Offset: Drivers of Intrinsic Scatter in The $M_{GCS} - M_h$ Scaling Relation for Massive Elliptical Galaxies

The following chapter has been published in The Astrophysical Journal (ApJ):

V. Dornan and W. E. Harris (July 2025). Major Mergers Mean Major Offset: Drivers of Intrinsic Scatter in the $M_{GCS} - M_h$ Scaling Relation for Massive Elliptical Galaxies. *The Astrophysical Journal* 988(1), 70

3.1 Introduction

Globular clusters (GCs) have long been a useful tool in tracing galaxy structure and evolution. These massive stellar clusters, hosting as many as 10^7 stars, are some of the oldest surviving objects within galaxies across all masses (VandenBerg et al. 2013; Beasley 2020). Their compact size and strong gravitational boundedness also ensure that these clusters can survive tidal disruption and merger events that their host galaxies have undergone (Reina-Campos et al. 2023; Joschko et al. 2024). As a result, the properties of a globular cluster system (GCS) can correlate with its host galaxy's global properties and merger history (Belokurov and Kravtsov 2023; Belokurov and Kravtsov 2024; Newton et al. 2024; Federle et al. 2024; Mirabile et al. 2024).

One scaling relation of particular interest is that between the total number of GCs (N_{GC}), or total mass enclosed in a galaxy's GCS (M_{GCS}) and the total mass of the galaxy, typically dominated by its dark matter halo (M_h) (Blakeslee et al. 1997). This relation has been known and studied both through observations and simulations for decades. It has been found that across a range of at least 10^6 in galaxy mass this relation holds a tight 1:1 linear shape (Spitler and Forbes 2009; Hudson et al. 2014; Harris et al. 2015; Burkert and Forbes 2020; Dornan and Harris 2023). It is well known that this relation, particularly for massive galaxies, is driven by mergers, as they can grow both the dark matter halos and GCSs of galaxies (Choksi and Gnedin 2019; Chen and Gnedin 2023; Valenzuela et al. 2024). However, there exists uncertainty over what drives the variation in GCS mass for galaxies of the same halo mass that is observed.

Observationally, there is a significant amount of GCS data for galaxies with halo masses in the range of $10^{11} - 10^{13} M_{\odot}$ (Peng et al. 2008; Villegas et al. 2010; Lim et al. 2024), becoming more sparse above this mass range, where brightest cluster galaxies (BCGs) dominate. For the data that is available in the literature, the methods used to determine both the M_{GCS} and M_h estimates are not always consistent. This makes it difficult to get an accurate observational understanding of the behaviour of this relation across different mass ranges.

The issue of consistency is especially interesting for galaxies with halo masses above $10^{13} M_{\odot}$, which are mostly BCGs (brightest cluster galaxies) with extended halos that may not be enclosed in the imaging used to determine GC counts. They also typically reside in high density clustered environments, which can also introduce difficulty in determining the exact boundary of the galaxy's GCS and the contribution from the host galaxy cluster's intracluster medium, which hosts its own GC population.

In these clustered environments BCGs typically have multiple nearby satellite galaxies that are included in imaging of the target BCG. The GCSs of these satellite galaxies also add difficulty in determining the GC counts for the target BCG, as these satellites host their own GCSs. It can sometimes become unclear which satellite galaxies should be masked from an image to ensure GC contamination is minimized, and which should be left in to ensure GC counts for the target BCG are maximized.

All of these considerations added together make studying GCSs around extremely massive

BCGs not as straightforward as their lower-mass counterparts, but the process can be optimized through consistent methodology. In this paper we apply a new Voronoi tessellation-based method of determining GC radial density profiles to 27 massive ellipticals, to replace the standard annulus-based method.

This new Voronoi method was introduced in Dornan and Harris 2024, hereafter referred to as Paper I, and it was found that when applied to circularly symmetric single systems of approximately 2000 or more detected objects the Voronoi method outperformed the conventional annulus method for both accuracy and precision of fits to the radial density profiles. In this paper we now will apply this method to a sample of more complicated, observed systems, many of which host significant satellite systems, have extended halos, or are highly elliptical. We derive more accurate, precise, and methodologically consistent GCS mass estimates for a large sample of galaxies with halo masses above $10^{13} M_{\odot}$. This will allow for the high-mass end of the $M_{GCS} - M_h$ relation to be far more accurately constrained observationally than previous mass estimates have allowed.

3.2 Methods

3.2.1 Galaxy Sample

The sample of galaxies analyzed in this work consists of 27 massive elliptical galaxies, most of which are classified as BCGs, and the remainder would be classified as the second or third brightest galaxies in their respective clusters, which we refer to here as next massive cluster galaxies (NMGCs). The first 11 galaxies listed in Table 3.1 were previously studied in Dornan and Harris 2023 using an annulus-based method to determine their GC radial density profiles, where here we will be updating their profile fits using the Voronoi method. The GCSs of the last 16 galaxies listed in Table 3.1 were studied photometrically in Harris 2023, although their GC radial density profiles were not determined.

Table 3.1 lists all galaxies in the sample as well as their Galactic latitudes and longitudes, their extinctions, distance moduli, total visual absolute magnitudes, total K-band absolute magnitudes, distances in Megaparsecs, and their classification as a BCG or NMCG, taken

Table 3.1: List of target galaxies

Target Name (1)	l (2)	b (3)	A_I (4)	$(m-M)_I$ (5)	M_V^T (6)	M_K (7)	$D(Mpc)$ (8)	Class (9)
J13481399-3322547	316.35°	+28.01°	0.082	36.335 ± 0.093	-21.7	-25.5	178 ± 8	BCG
J13280261-3145207	311.96°	+30.47°	0.079	36.446 ± 0.093	-22.0	-25.3	187 ± 8	NMCG
J13275493-3132187	311.97°	+30.69°	0.076	36.839 ± 0.093	-23.3	-26.1	225 ± 10	NMCG
J13272961-3123237	311.89°	+30.85°	0.088	36.679 ± 0.093	-23.3	-26.2	208 ± 9	NMCG
ESO 509-G067	314.69°	+34.75°	0.103	36.023 ± 0.094	-23.3	-25.8	153 ± 7	NMCG
ESO 509-G020	312.83°	+34.81°	0.086	35.957 ± 0.094	-23.3	-25.6	149 ± 6	NMCG
ESO 509-G008	312.47°	+34.78°	0.080	36.031 ± 0.093	-23.0	-26.1	155 ± 7	BCG
ESO 444-G046	311.99°	+30.73°	0.076	36.635 ± 0.093	-24.8	-27.1	205 ± 9	BCG
ESO 383-G076	316.32°	+28.55°	0.083	36.223 ± 0.093	-24.2	-26.8	169 ± 7	BCG
ESO 325-G016	314.72°	+23.64°	0.123	36.214 ± 0.093	-22.3	-25.4	165 ± 7	BCG
ESO 325-G004	314.08°	+23.57°	0.092	35.958 ± 0.093	-23.3	-26.2	149 ± 6	BCG
ESO 306-G017	246.41°	-30.29°	0.041	36.069 ± 0.094	-24.3	-26.5	161 ± 7	BCG
NGC 1129	146.34°	-15.63°	0.279	34.541 ± 0.108	-22.9	-26.1	71 ± 3	BCG
NGC 1132	176.45°	-51.07°	0.080	34.993 ± 0.094	-22.5	-25.7	96 ± 4	NMCG
NGC 1272	150.52°	-13.32°	0.245	34.512 ± 0.097	-23.3	-25.6	74 ± 3	NMCG
NGC 1278	150.56°	-13.21°	0.251	34.518 ± 0.097	-22.3	-25.2	71 ± 3	NMCG
NGC 3258	272.90°	+18.82°	0.123	33.457 ± 0.095	-22.1	-25.1	46 ± 2	BCG
NGC 3268	272.94°	+19.18°	0.157	33.491 ± 0.096	-23.2	-25.2	46 ± 2	BCG
NGC 3348	134.63°	+41.35°	0.113	33.125 ± 0.094	-21.7	-25.1	40 ± 2	NMCG
NGC 4696	302.40°	+21.56°	0.170	33.604 ± 0.099	-24.2	-26.3	49 ± 2	BCG
NGC 4874	58.08°	+88.01°	0.014	35.094 ± 0.094	-23.7	-26.2	104 ± 4	BCG
NGC 4889	57.19°	+87.89°	0.015	35.095 ± 0.094	-23.8	-26.7	104 ± 4	NMCG
NGC 6166	62.93°	+43.69°	0.017	35.611 ± 0.094	-23.6	-26.43	131 ± 6	BCG
NGC 7626	87.86°	-48.38°	0.110	33.616 ± 0.096	-22.4	-25.5	50 ± 2	BCG
NGC 7720	103.50°	-33.07°	0.108	35.669 ± 0.096	-23.2	-26.2	124 ± 5	BCG
UGC 10143	28.91°	+44.52°	0.048	36.069 ± 0.095	-24.4	-25.8	160 ± 7	BCG
UGC 9799	9.42°	+50.12°	0.057	35.936 ± 0.094	-23.6	-26.3	150 ± 6	BCG

Key to columns: (1) Galaxy identification; (2,3) Galactic longitude and latitude; (4) foreground extinction; (5) apparent distance modulus; (6) total visual absolute magnitude; (7) total K-band absolute magnitude; (8) adopted distance in Mpc; (9) BCG or NMCG classification. All images are taken with the HST ACS/WFC camera.

from the NASA/IPAC Extragalactic Database. The distances were determined using $H_0 = (70 \pm 3km/s/Mpc)$. Although some the galaxies in our sample have updated surface brightness fluctuation distances available, we have decided to use the same distance calculation for all galaxies for internal consistency. We have also chosen to use $H_0 = (70 \pm 3km/s/Mpc)$ for consistency with the analysis done in Dornan and Harris 2023 and Harris 2023, but included an uncertainty which covers the H_0 values found by Hinshaw et al. 2013, Planck Collaboration et al. 2016, and Planck Collaboration et al. 2020. This sample of galaxies was selected from the HST archive based on their distances, filters used for imaging, and depth of exposure times. These selection criteria ensured that the GCs hosted by these galaxies would appear star-like and have high signal-to-noise ratios (SNRs), making them easily identifiable by the photometry code used (Dornan and Harris 2023; Harris 2023)

3.2.2 Photometry

Photometry for all galaxies in this sample was carried out using DOLPHOT (Dolphin 2000), a package originally designed for stellar photometry, but which is widely used for GC photometry at distances above $\sim$ 25Mpc, as at these distances GCs appear morphologically star-like.

All photometric data used in this paper is from Dornan and Harris 2023 and Harris 2023. Key photometric parameters used can be found in Table 1 of Harris 2023. Once DOLPHOT identified star-like objects in each image, those objects were culled to leave behind only GC candidates. For the galaxies studied in Dornan and Harris 2023 this was done purely through chi, sharp, and signal-to-noise ratios, while for the galaxies studied in Harris 2023, due to the multiple filters available, star-like objects could also be culled using colour-magnitude diagrams. The limiting magnitudes for each image were determined by adding artificial GCs with a variety of magnitudes to each image, re-running the photometric process, and determined at which magnitude less than 50% of the artificial stars were identified by DOLPHOT. These limiting magnitudes can be found in Table 2 of Dornan and Harris 2023 and Table 3 of Harris 2023.

3.2.3 Determining Radial Profiles with Voronoi Tessellations

Once a 2D distribution of all detected and limiting-magnitude-corrected GCs around each target galaxy has been created, we then move on to create GC radial density profiles for each galaxy. For some of our sample these profiles have already been determined in Dornan and Harris 2023 with a standard circular annulus method. However, our aim in this work is to improve the fits of those profiles with a new Voronoi method, as was described in Paper I.

In brief, the Voronoi method begins by taking the 2D distribution of objects and creating a Voronoi tessellation map, where each object is contained in a polygon whose area is inversely proportional to its local density. The Voronoi tessellations were computed using the built-in Voronoi function in the scipy.spatial package (Virtanen et al. 2020). The areas of these tessellations are then inverted to obtain a density value for each detected object. As described in Paper I, in order to reduce stochastic scatter for the radial profile, the individual tessellations are then spatially binned into groups of five and combined into one larger cell with an averaged radius value and combined density value. The densities of these binned cells are then plotted as a function of radius. In order to further reduce stochastic scatter, the mean density of the cells in each interval of radius is determined and any cells with densities greater than 1.5 standard deviations from the mean are culled.

One of the benefits of this Voronoi method over the annulus method that was not explored in Paper I was the ability to better identify satellite galaxies with contaminating GCSs. Although satellite galaxies can be identified visually in the GC spatial distribution, it is not always immediately clear which galaxies are large and extended enough to warrant removal. Typically, one method of identifying significant satellite systems is to find GC overdensities in the radial and azimuthal profiles and mask out the satellite that would correspond to the overdensity's position and re-run the whole process. One of the difficulties with the annulus method was that it was very difficult to accurately identify overdensities when only $\sim 20-25$ density values are available and can be subject to their own stochastic scatter.

However with the Voronoi method, the increased number of density values available makes it much more apparent which satellite systems need to be removed and which could remain without significantly impacting the profile fit. As a result, many of the satellites that were removed from the galaxies studied in Dornan and Harris 2023 (see figure 4) were found unnecessary to mask, and instead remained in this work. In the case of ESO 325-G004, there was one satellite that was not removed in Dornan and Harris 2023 that was now identified to be significant and removed. An example of this can be see in Figure 3.1.

Once this culling and satellite system removal is complete, a powerlaw is fit to the remaining data using a boostrapping technique with 1000 iterations. An example of this fit with the Voronoi datapoints can be seen in Figure 3.1 for ESO 325-G004. The fits for all the galaxies in the sample with colour information are shown in Figure 3.2, and the fits for all the galaxies in the sample without colour information are shown in Figure 3.3. As was discussed in the results of Paper I, the Voronoi method returns radial profile fits with lower uncertainties, subsequently allowing for more precise estimates of total GC counts.

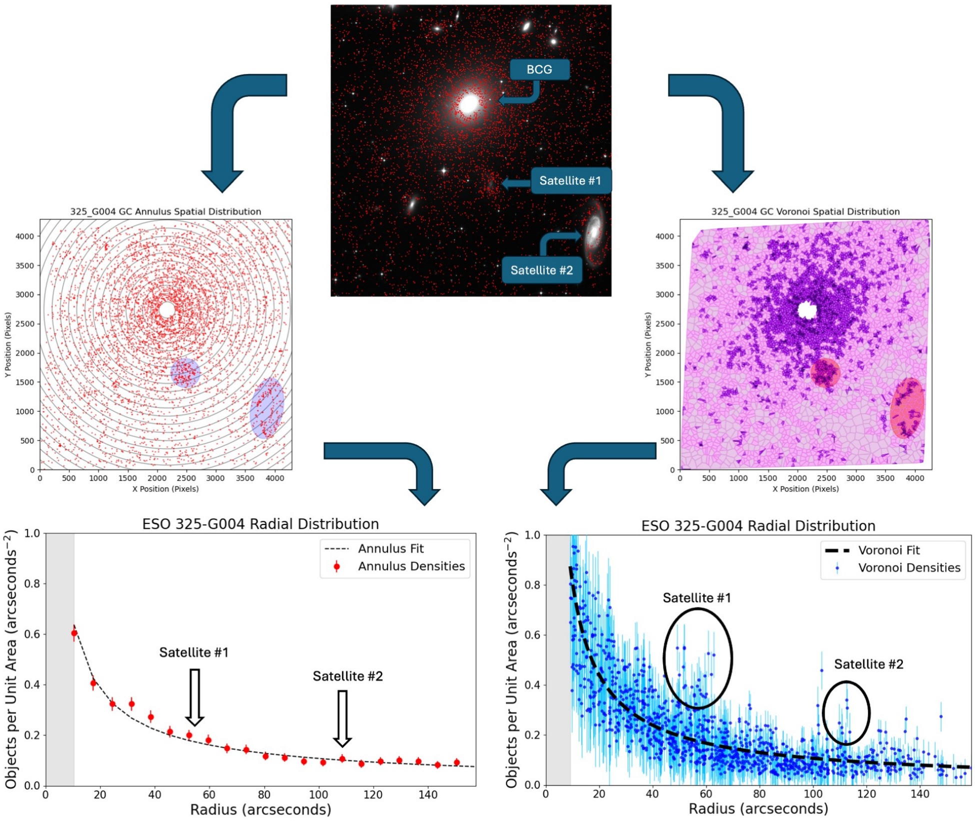

FIGURE 3.1: An example of the spatial distributions and radial density profiles of ESO 325-G004 using both the annulus and Voronoi methods, before removal of any satellites. On the left it is difficult to identify the satellites and determine if they are affecting the fit to the data. On the right it is much more clear where the satellites are, how extended they are, and by how much they are driving up the average density at their radii.

3.2.4 Determining GCS Masses

Once the radial density profiles of the galaxies were determined they were then integrated out to the defined radius of the GCS. Here we adopt the same definition of GCS radius as in Dornan and Harris 2023, where $R_{GCS} = 0.1R_{vir}$. This is to ensure that we have a standardized definition of GCS size in order to effectively compare the resulting GCS masses of these sample galaxies to one another. We define the R_{GCS} using Equation 3.1, below.

$$\begin{aligned} R_{GCS} &\equiv 0.1 R_{vir} \\ &= 0.1\Big[\frac{3M_{vir}}{4\pi \cdot 200\rho_c}\Big]^{1/3} \\ &= 0.1\Big[\frac{GM_{vir}}{100H_0^2}\Big]^{1/3} \end{aligned} \tag{3.1}$$

where M_{vir} is in Solar masses and H_0 in km s^{-1} Mpc^{-1}. Here $\rho_c = 3H_0^2/8\pi G$ is the cosmological critical density and it is assumed for the purposes of this study that $M_{vir} \simeq M_h$. We note that this definition does mean that the R_{GCS} becomes dependent on the M_h for each galaxy, but does so on the cube root, making it not strongly sensitive to small variations in M_h. Although it *is* sensitive to large variations in M_h, it is still to a smaller extent than by which GCS size in general scales with M_h (Forbes 2017; Hudson and Robison 2018).

Due to the high background light intensity at the centres of these galaxies DOLPHOT is unable to identify any GCs in the innermost radii of the galaxies in the sample. Since we have a lack of information in regards to the radial density profiles at these radii we simply assume a constant density here, equivalent to the density of the innermost data available. This approximation is reasonable as the area of this region is small and observations of the Milky Way and M31, for which we do have GC data at small radii, find that the GC density does in fact level off towards the bulge (Huxor et al. 2011). Other studies of massive ellipticals also find that the GC radial density profiles begin to flatten before detection becomes no longer possible (Capuzzo-Dolcetta and Mastrobuono-Battisti 2009). It should be noted that for BCGs this flattening of the profile can typically occur between $2 - 10$ kpc (Peng et al. 2011), and as can be seen in column 3 of Table 3.2, the inner limits of our photometry for some of our galaxies is within or exceeds this range. We caution that depending on assumptions made about where these GC density profiles level off it is possible for the N_{GC} estimates of this sample to increase by approximately 2%.

Thus, the total number of globular clusters in the image can be defined by Equation 3.2, as shown below.

$$N_{GC} = \int_0^{R_{in}} \sigma_{in} 2\pi r dr + \int_{R_{in}}^{R_{GCS}} 2\pi r \sigma_{cl} dr \tag{3.2}$$

Here R_{in} represents the inner limit of the GC photometry, R_{GCS} represents the radial size of the GCS, σ_{in} represents the adopted, constant GC density in the inner region, and σ_{cl} represents the variable density of GCs in arcseconds^{-1} in at all other radii.

Although we have already removed background GCs and attempted to minimize the contamination from the ICM by using a standard R_{GCS} definition, within our image we likely still have a fraction of our detected GCs which are actually ICGCs. Due to the small field of view of our HST images it is outside the scope of this work to determine the ICGC background density within all the different environments which host the various galaxies in our sample. Instead, we assume that $3\% \pm 3\%$ of the final, integrated N_{GC} estimate are from the ICM and are thus subtracted from our totals. This estimate would cover very low-density environments where the ICGC contamination is estimated to be negligible (Sánchez-Janssen et al. 2019; Harris et al. 2020), as well as richer environments where the contamination has been estimated to be as much as $5\% - 6\%$ (Madrid et al. 2018; Harris 2023).

Finally, this estimate must be corrected to account for the GCs that have magnitudes dimmer than the limiting magnitude of the image. For the galaxies in our sample we assume that their GC luminosity functions (GCLFs) take on a well-defined, classical log-normal shape, with peaks at $M_I = -9.0 \pm 0.3$ and Gaussian dispersions of $\sigma_g = 1.30$ (Harris et al. 2014). The fraction of undetected GCs in each image can then be calculated through comparing the peak GCLF magnitude to the absolute limiting magnitude of the images of each galaxy in the sample.

With the final, corrected estimate of the total GC count for each galaxy, which, as can be seen in Table 3.2, is on the order of $10^4 - 10^5$, we can then convert this to total GCS mass by simply multiplying it by the average single GC mass for each galaxy. For massive ellipticals such as these, there exists a well-defined, shallow relation between average GC mass and host galaxy luminosity (Villegas et al. 2010; Harris et al. 2017), as described in Equation 3.3 below.

$$\log\langle M_{GC}\rangle = 5.698 + 0.1294M_V^T + 0.0054(M_V^T)^2 \tag{3.3}$$

We adopt an uncertainty on our calculated $\log\langle M_{GC}\rangle$ values of ± 0.1 dex based on the scatter in this relation around BCGs (Harris et al. 2014). This mass range distinction is important as scatter increases for dwarf galaxies (Villegas et al. 2010). The final resulting GCS masses for our sample can be found in Table 3.2.

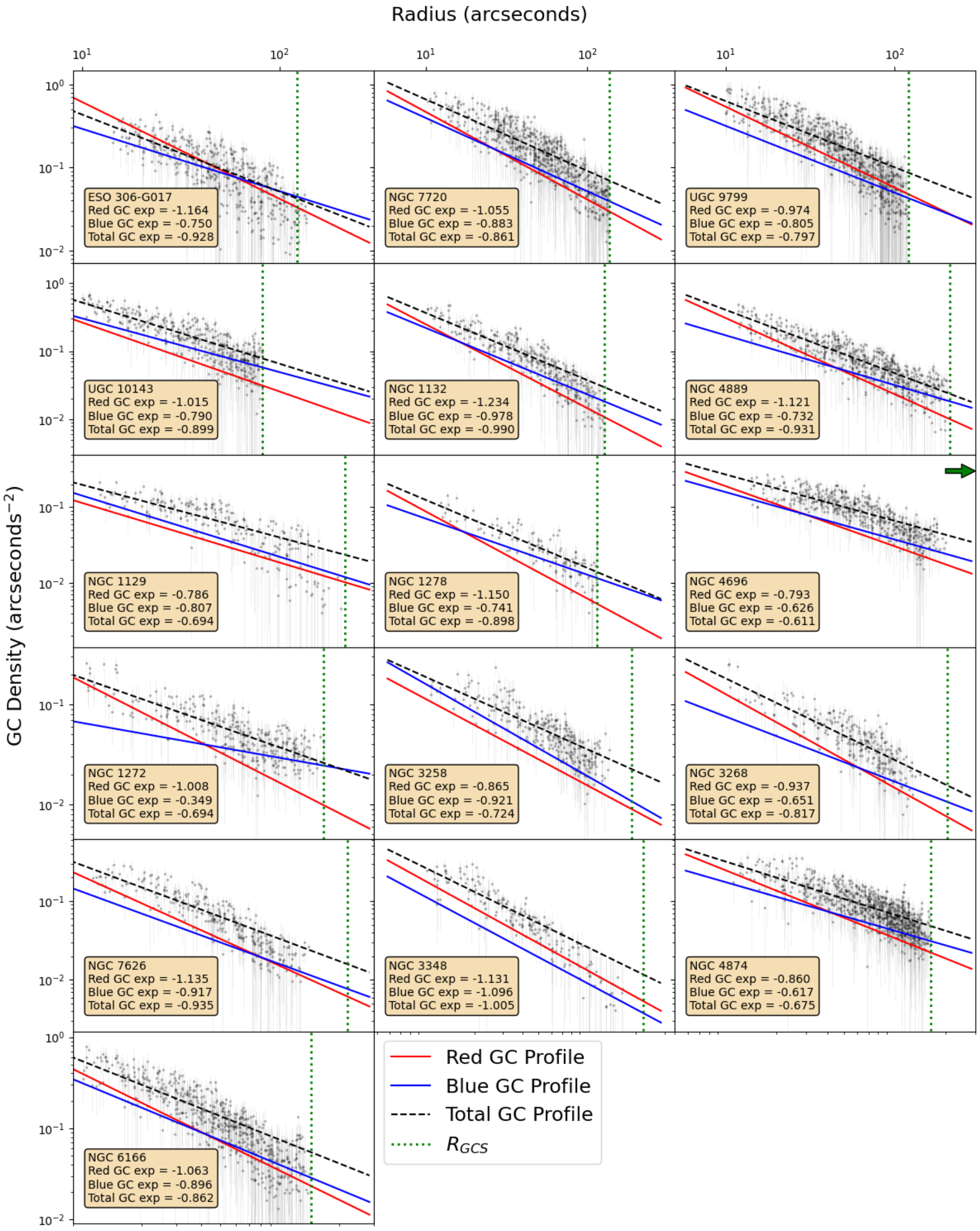

FIGURE 3.2: The red, blue and total GC density profiles for the 16 galaxies in this sample with colour information available, plotted in log-log space. The green vertical dashed lines represent the radius of the GCS and outer bound of integration for determining each galaxy's N_{GC}, defined here as $0.1R_{vir}$. Each galaxy's exact R_{GCS} values can be found in Table 3.2. The names of each galaxy and the exponents of their powerlaw fits for the total, red, and blue GCS profiles are shown in the inset boxes.

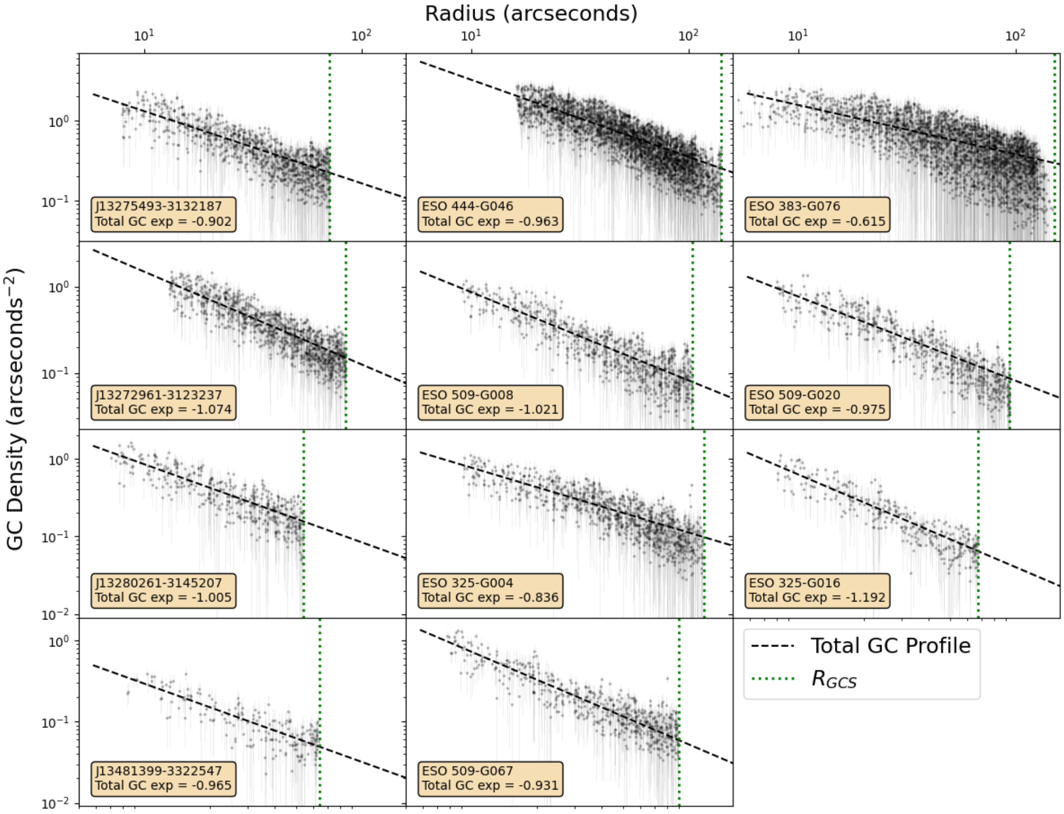

FIGURE 3.3: Same as for Figure 3.2, but for the 11 galaxies in this sample with no colour information.

3.2.5 Determining Halo Masses

In this work we use the SHMR (stellar-to-halo mass ratio) as defined in Hudson et al. 2015 to convert stellar masses to halo masses for the galaxies in our sample. This relation is well defined for massive galaxies such as the ones being studied here and is described by Equation 3.4 below.

$$M_\star/M_h = 2f_1\left[\left(\frac{M_\star}{M_1}\right)^{-0.43} + \frac{M_\star}{M_1}\right]^{-1} \tag{3.4}$$

Here M_1 is the transition or pivot halo mass, set to $10^{10.76}M_\odot$, and f_1 is the mass ratio at M_1, which is $f_1 = 0.0227$. This equation has been adjusted to a redshift of zero, which is appropriate given the low distances of the galaxies in this sample. The stellar masses of the galaxies were calculated from their K-band total luminosities using the K-band stellar mass-to-light ratio, assuming a Chabrier/Kroupa mass function (Bell et al. 2003).

Table 3.2: Final M_{GCS} and M_h Values

Target Name (1)	N_{GC} (2)	$R_{in}(kpc)$ (3)	$R_{GCS}(kpc)$ (4)	$M_{GCS}(\times 10^9 M_\odot)$ (5)	$M_h(\times 10^{13} M_\odot)$ (6)
J13481399-3322547	1600 ± 300	5.6 ± 0.2	53.3 ± 0.2	0.42 ± 0.08	1.73 ± 0.39
J13280261-3145207	3500 ± 500	5.5 ± 0.2	49.3 ± 0.3	1.03 ± 0.17	1.23 ± 0.29
J13275493-3132187	10000 ± 2000	7.1 ± 0.3	78.1 ± 0.4	4.13 ± 0.88	4.89 ± 1.14
J13272961-3123237	9100 ± 1600	11.6 ± 0.5	85.6 ± 0.4	3.76 ± 0.74	6.30 ± 1.46
ESO 509-G067	4200 ± 600	4.8 ± 0.2	66.7 ± 0.2	1.73 ± 0.28	2.92 ± 0.65
ESO 509-G020	5800 ± 800	4.7 ± 0.2	68.3 ± 0.2	2.35 ± 0.38	3.22 ± 0.70
ESO 509-G008	6500 ± 900	5.6 ± 0.2	78.5 ± 0.2	2.45 ± 0.38	4.91 ± 1.06
ESO 444-G046	40800 ± 6700	14.9 ± 0.6	141 ± 0.6	26.4 ± 4.80	28.5 ± 6.39
ESO 383-G076	39300 ± 5000	4.1 ± 0.2	124 ± 0.4	21.3 ± 3.38	18.6 ± 3.95
ESO 325-G016	2800 ± 400	5.2 ± 0.2	54.1 ± 0.2	0.89 ± 0.16	1.53 ± 0.34
ESO 325-G004	9000 ± 1100	5.4 ± 0.2	85.4 ± 0.2	3.65 ± 0.56	6.20 ± 1.34
ESO 306-G017	17000 ± 6000	10.5 ± 0.5	96.7 ± 0.3	9.24 ± 3.36	10.3 ± 2.51
NGC 1129	7800 ± 1500	3.5 ± 0.1	73.8 ± 0.5	2.88 ± 0.60	4.59 ± 0.97
NGC 1132	5600 ± 1300	2.8 ± 0.1	59.2 ± 0.8	1.85 ± 0.46	2.37 ± 0.51
NGC 1272	6800 ± 1500	2.4 ± 0.1	57.7 ± 0.8	2.79 ± 0.68	2.19 ± 0.47
NGC 1278	3300 ± 900	1.8 ± 0.1	44.7 ± 1.3	1.04 ± 0.31	1.02 ± 0.21
NGC 3258	4800 ± 600	1.7 ± 0.1	42.4 ± 1.5	1.44 ± 0.23	0.87 ± 0.17
NGC 3268	4300 ± 600	1.9 ± 0.1	46.1 ± 1.2	1.71 ± 0.27	1.12 ± 0.23
NGC 3348	4000 ± 500	1.6 ± 0.1	42.8 ± 1.4	1.09 ± 0.15	0.89 ± 0.18
NGC 4696	23300 ± 3400	2.8 ± 0.1	86.4 ± 0.4	12.5 ± 2.11	7.37 ± 1.55
NGC 4874	12300 ± 2800	4.3 ± 0.2	81.4 ± 0.4	5.70 ± 1.38	6.15 ± 1.31
NGC 4889	12600 ± 3000	5.0 ± 0.2	106.5 ± 0.2	5.93 ± 1.51	13.8 ± 2.80
NGC 6166	18900 ± 5400	3.5 ± 0.2	91.8 ± 0.3	8.55 ± 2.54	8.85 ± 1.88
NGC 7626	5100 ± 600	2.2 ± 0.1	53.7 ± 0.9	1.64 ± 0.23	1.77 ± 0.37
NGC 7720	15000 ± 3700	3.9 ± 0.2	80.9 ± 0.4	6.02 ± 1.55	6.04 ± 1.29
UGC 9799	17000 ± 4700	3.5 ± 0.1	63.5 ± 0.6	7.68 ± 2.22	7.56 ± 1.77
UGC 10143	8600 ± 2500	4.3 ± 0.2	87.2 ± 0.3	4.86 ± 1.47	2.94 ± 0.65

Key to columns: (1) Target name; (2) Total number of GCs; (3) Inner limit of GC photometry; (4) Standardized GCS radius; (4) GCS masses; (5) Dark matter halo masses.

3.3 Results

3.3.1 Updated GCS Masses

Figure 3.4 shows the GCS and halo masses for all the galaxies studied in this work. For the 11 galaxies which had masses previously determined in Dornan and Harris 2023 with the annulus method, we plot those old values in purple and the new masses in black.

As can be seen clearly in Figure 3.4 the updated masses are all of higher values and, with the exception of ESO 383-G076, within the errorbars of the original mass estimates. In addition, all updated GC radial density profile fits have lower uncertainties when calculated with the Voronoi method than with the annulus method, although due to the previously discussed higher ICGC uncertainty adopted in this paper, it does not end up translating to the M_{GCS} uncertainties.

The higher precision in the radial density profile fits with the Voronoi method was as expected

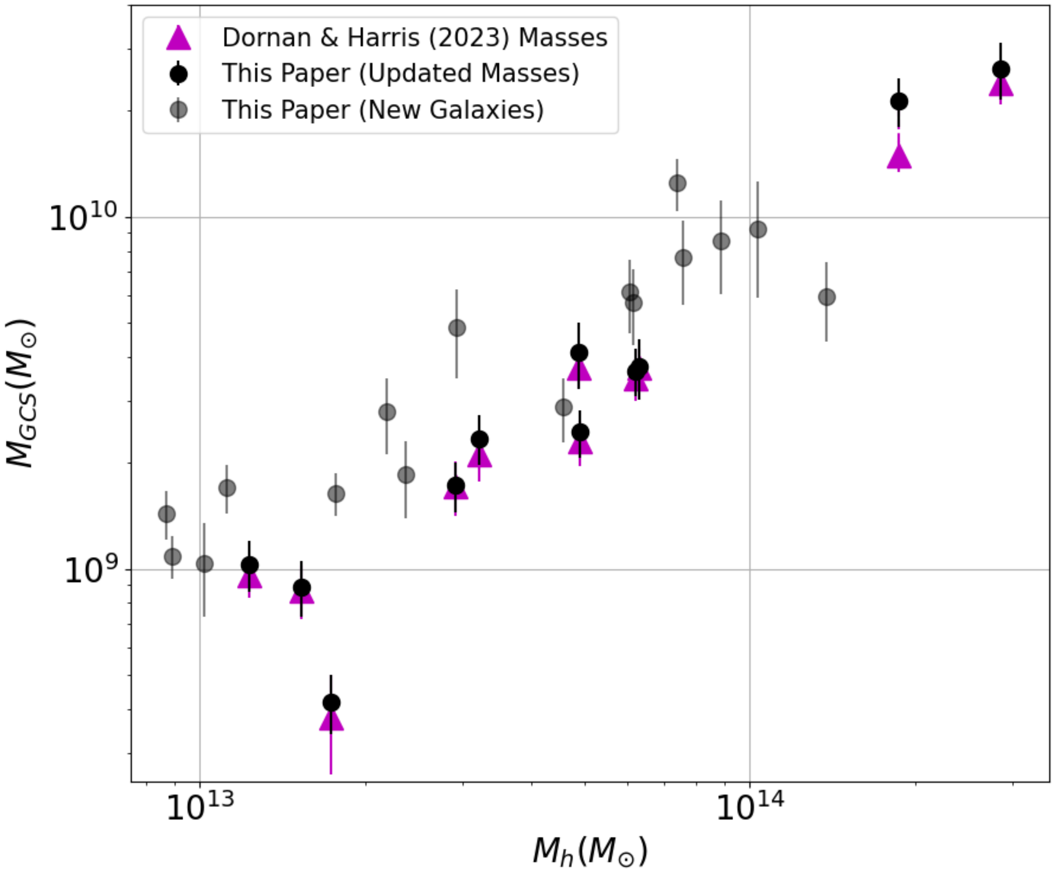

FIGURE 3.4: $M_{GCS} - M_h$ relation plotted in log-log space for the galaxies studied in this paper. The M_{GCS} values calculated using an annulus method and published in Dornan and Harris 2023 are plotted in purple triangles and the updated values calculated using the Voronoi method detailed int this paper are plotted in black circles. Grey circles denote the masses determined with the Voronoi method for the galaxies studied in this paper but not in Dornan and Harris 2023.

based on the results of Paper I but, at first glance, the higher mass estimates were unexpected. Paper I found that for GCSs with more than ~ 5000 objects, as is the case for all of these massive elliptical galaxies, the Voronoi method should return an accurate N_{GC} estimate and the annulus method should over-predict that value, not under-predict. However, upon further comparison of the simulated systems used in Paper I and the observed GCSs of the galaxies in this sample, it was found that although the sizes of these systems are similar, the steepnesses of their GC density profiles differ.

The massive simulated systems in Paper I all have shllower GCS profiles than 10 of the 11 GCSs studied with both methodologies in this paper. One simulated system in Paper I had a steeper profile than the galaxies in this paper, and it was found that the annulus method underpredicted its N_{GC} estimate compared to the Voronoi method, which is what we see for these galaxies. This is due to the fact that for shallow profiles small areas of high local density in the inner regions of a distribution can artificially increase the average density of the innermost annuli, whereas for steep profiles the annulus bins cannot accurately mimic the more rapid change in radial density.

This steep simulated system in Paper I, however, was of a much smaller size than our observed galaxies, hosting only 300 objects. As such, the Voronoi method was found to predict the correct N_{GC} only slightly better than the annulus method, likely due to small number statistics. We can extrapolate the results from Paper I out to massive systems with steep profiles; expecting the Voronoi method to accurately estimate N_{GC} and the annulus method to underpredict it.

ESO 383-G076 has an updated mass higher than calculated in Dornan and Harris 2023 despite also having a very shallow density profile with a powerlaw exponent of 0.615. This is because this galaxy is highly elliptical and this was not properly corrected for when determining the GC density profile in the previous paper. Thus, the increase in the mass estimate comes from taking ellipticity into account, rather than differences between the Voronoi and the annulus method.

3.3.2 The Global $M_{GCS} - M_h$ Relation

Once all of the masses for the galaxies in our sample were calculated they were plotted on the $M_{GCS} - M_h$ relation alongside galaxies of other mass ranges as well as predictions from simulations. This can be seen in Figure 3.5. For observational data we have plotted our sample of massive elliptical galaxies with galaxies in the ACS Virgo Cluster Survey (Peng et al. 2008) and the survey of low-mass galaxies in the Local Group which was used in Eadie et al. 2022 and includes GCS data from Harris et al. 2013; Forbes et al. 2018; Forbes 2020. We also highlight the locations of the Virgo BCG, M87 (Peng et al. 2008), M31 (Harris et al. 2013; Patel et al. 2017), and the Milky Way (Harris et al. 2013; Kravtsov and Winney 2024) on the relation.

We have also plotted where five galaxy clusters lie on the $M_{GCS} - M_h$ relation as well, represented by the green crosses in Figure 3.5, although these are not used in calculating the slope of the relation. These galaxy clusters include Abell 2744 (Harris et al. 2017), Abell 1689

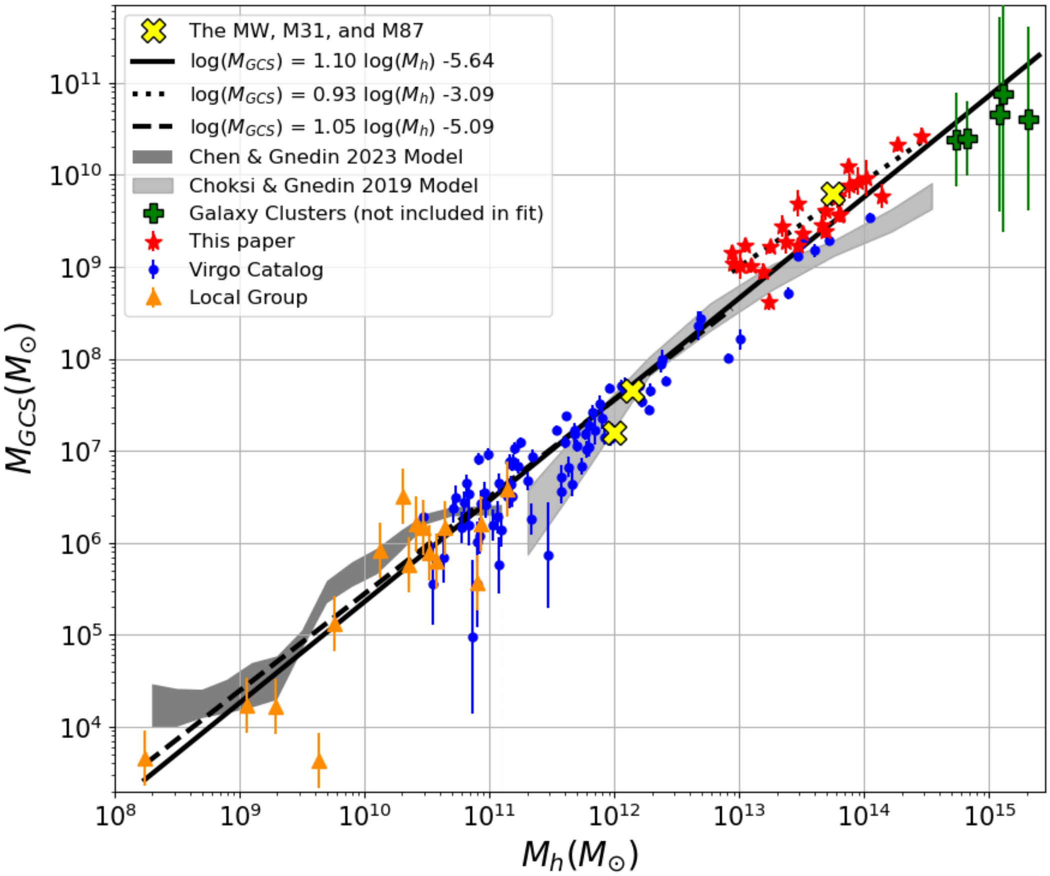

FIGURE 3.5: $M_{GCS} - M_h$ relation plotted in log-log space. Blue circles are Virgo catalog galaxies from Peng et al. 2008, orange triangles are low-mass local group galaxies, green crosses are galaxy clusters (not used for the fit), and red stars are the galaxies from this sample. The Milky Way, M31, and M87 have been highlighted in yellow crosses. The lighter shaded region is the results from the Choksi and Gnedin 2019 model and the darker shaded region is the results from the Chen and Gnedin 2023 model. The solid black line is the linear fit to all three extragalactic observational samples, the dashed line is the fit to just the local group and Virgo galaxy samples, and the dotted line in the fit to just the massive galaxy sample detailed in this paper.

(Alamo-Martínez et al. 2013; Harris et al. 2017), the Perseus cluster (Harris and Mulholland 2017b), the Coma cluster (Peng et al. 2011), and the entirety of the Virgo cluster summed together (Peng et al. 2008; Durrell et al. 2014), and represent estimates of the N_{GC} hosted both within and between all member galaxies, which results in the larger M_{GCS} uncertainties. This estimate was done, very roughly, by using Equation 3.3 to determine the $\langle M_{GC} \rangle$ for each cluster's BCG, assuming that approximately half of all the GCs hosted by the cluster have that mass, and that the other half have masses similar to the average Milky Way GC ($2.5 \times 10^5 M_\odot$).

Rather than add in all galaxies with known GCSs (which make an inhomogeneous list with measurements from a wide variety of methods and raw data), here we deliberately subselect only the ones from the homogeneous, well defined Virgo survey, and the Local Group members whose GC numbers are well determined and allow us to extend the relation to the lowest possible galaxy masses. With this combination of observational samples the $M_{GCS} - M_h$ relation now spans over 7 orders of magnitude in GCS mass, the most complete and methodologically consistent global analysis of this relation to date.

It should be noted that the uncertainties on the GCS masses for the Local Group dwarfs were adopted as 0.3 dex. Though the N_{GC} values for the dwarfs are well known (Eadie et al. 2022), the conversion to M_{GCS} requires multiplying by a mean mass-to-light ratio, which observationally shows a typical cluster-to-cluster range of a factor of two (cf. Villegas et al. 2010; Harris et al. 2017). Here we adopt a mean mass-to-light ratio of 1.4 for these local dwarfs.

The shaded regions in Figure 3.5 correspond to the results from Choksi and Gnedin 2019 and Chen and Gnedin 2023. This data is results from analytical GC models applied to the *Illustris-1-Dark* dark matter-only cosmological simulations. As can be seen in Figure 3.5, globally, the relation continues to hold linearly in log-log space across all three samples of galaxies. However, when fitting a linear regression to the observational data we found that the global relation is not only steeper than that predicted by the simulations, but is also slightly steeper than a 1:1 ratio. It should also be noted that when a linear regression is fit to only the sample of massive ellipticals studied here, of which the majority are BCGs, the slope is shallower than a 1:1 ratio. Table 3.3 shows the solutions and associated uncertainties when fitting to each sample and combination of samples. Interestingly, we find that fitting only data from Local Group galaxies and M87 results in a close approximation of our fit to the full dataset.

3.3.3 Trends with GCS Properties

We also take the opportunity to study how two different GCS properties may relate to their offset from the main relation. Figure 3.6 plots the massive galaxies in our sample with the colour bars representing the fraction of GCs that are red rather than blue (upper panel) and the exponent of the GC density profile as a representation of profile steepness (lower panel). We also plot the

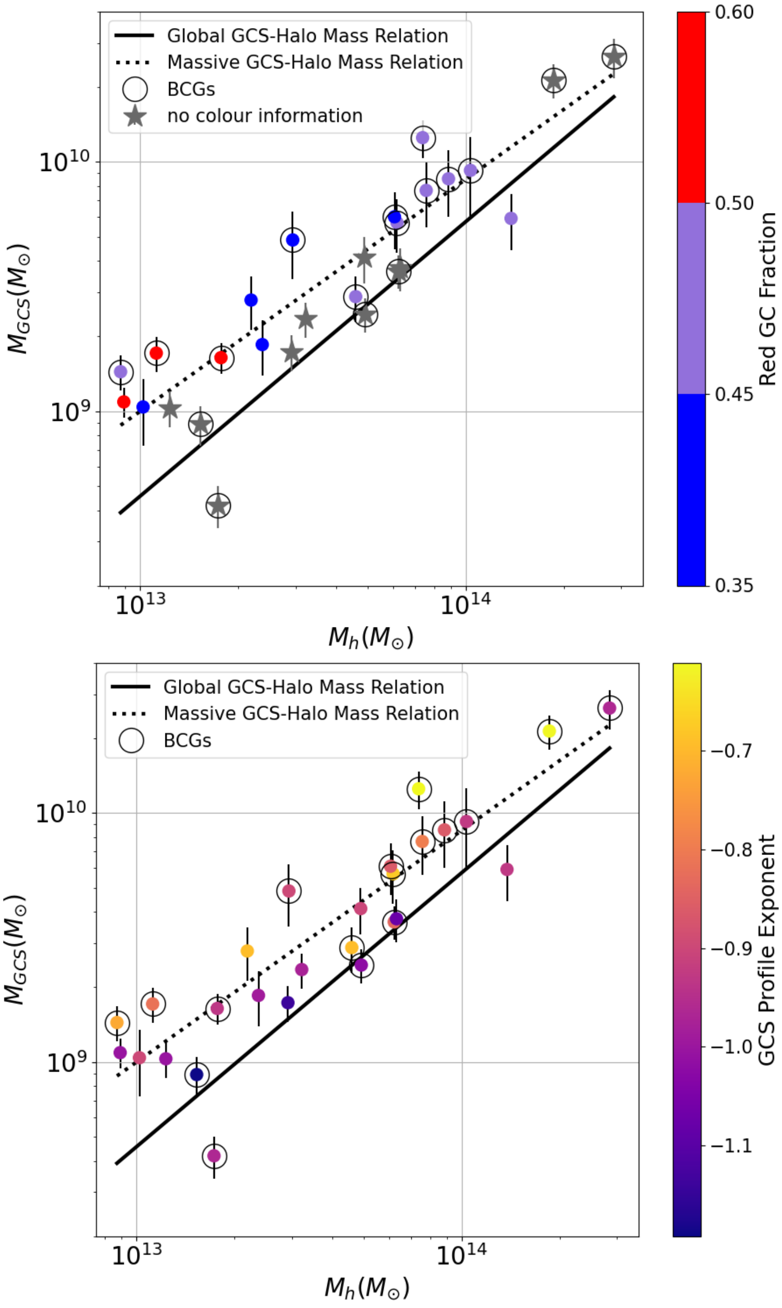

FIGURE 3.6: M_{GCS} vs M_h in log-log space for this paper's sample of massive galaxies. The linear fit determined from just this sample is represented by the dotted line, and the linear fit determined from this sample, the Virgo sample, and the Local Group sample is represented by the solid line. Black circles identify BCGs. *Top:* Colour represents the fraction of red GCs, grey stars are galaxies without colour information. *Bottom:* Colour represents the slope of the galaxies' GC radial density profile, with dark colours corresponding to steep and light corresponding to shallow.

TABLE 3.3: Linear Fit Solutions for $M_{GCS} - M_h$ Relation

Sample Combination (1)	Slope (2)	Intercept (3)
All Samples	1.10 ± 0.02	-5.64 ± 0.89
Massive Galaxies Only	0.93 ± 0.09	-3.09 ± 1.02
Virgo Cluster Only	1.05 ± 0.03	-5.05 ± 0.91
Local Group Only	1.11 ± 0.15	-5.82 ± 1.04
Massive Galaxies + Virgo Cluster	1.10 ± 0.03	-5.62 ± 0.89
Massive Galaxies + Local Group	1.13 ± 0.04	-5.85 ± 0.94
Virgo Cluster + Local Group	1.05 ± 0.03	-5.09 ± 0.90
Local Group + M87	1.16 ± 0.06	-6.32 ± 0.96

Key to columns: (1) Combination of observational samples used for the linear fits: either all of them, only one, or a combination of two; (2) The slope of the fit in log-log space; (3) The intercept of the fit in log-log space.

slope of the $M_{GCS} - M_h$ relation for all galaxies with a solid line, as was plotted in Figure 3.5, as well as the $M_{GCS} - M_h$ relation determined for just the massive galaxies in our sample with a dotted line.

16 of the 27 galaxies in our sample have imaging with multiple filters available, allowing for color information. We find that the GCSs of these galaxies have bimodial colour distribution (see Figure 12-14 in Harris 2023), which is expected for galaxies in this mass range (Hartman et al. 2023). We define red vs blue GCs based on the double-Gaussian fit to the color distributions for each GCS, where the red vs blue fits become dominant over the other. We find no significant trend between galaxy position on the relation and GC fraction of red N_{GC}.

However, when we compare GC radial density profile steepness against position on the relation we *do* see a trend. We find that, independent of host galaxy mass, a galaxy is more likely to lie above the $M_{GCS} - M_h$ relation if it has a shallow GC radial density profile and it is more likely to lie below the relation if it has a steep profile.

Figure 3.7 shows the amount a galaxy is offset from the $M_{GCS} - M_h$ relation derived form the massive galaxy sample in log-space as a function of radial density profile exponent derived from all GCs in the system, red GCs only, and blue GCs only. The left panel plots all 27 massive ellipticals in our sample, while the middle and right panels plot only the 16 ellipticals with colour information. Figure 3.2 shows the fits for red and blue GCs separately for the galaxies in our sample with colour information, along with the profile exponents.

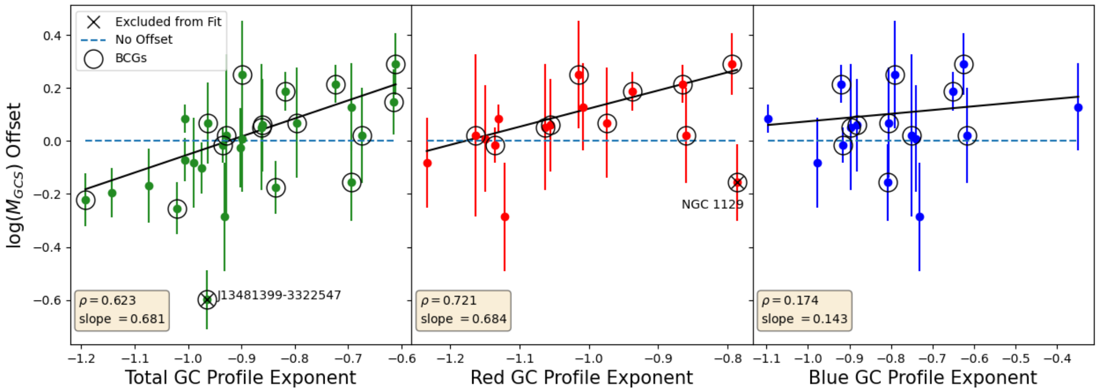

FIGURE 3.7: All subfigures show the log(M_{GCS}) offset from the $M_{GCS} - M_h$ relation derived from the massive galaxy sample as a function of slope of the galaxies' total GC density profiles, with more negative numbers being steeper and more positive numbers being more shallow. *Left:* Total offset vs slope of density profile for all GCs. *Middle:* Total offset vs slope of red GC density profile. *Right:* Total offset vs slope of blue GC density profile. Note that the leftmost subfigure plots the full 27 galaxy sample, while the middle and right subfigures only plot the 16 galaxies with colour information.

It can be clearly seen that this trend exists when looking at both the steepnesses derived from the total GCS and the red GCs, but is not present for the blue GCs. We found a Spearman correlation coefficient of 0.63, with a p-value of 0.0005, and a slope of 0.73 for total GCS profile steepness. When looking at the red and blue GC density profiles we find that this correlation is being driven entirely by the red GC population, as there exists no trend with relation offset and blue GC density profile steepness (Spearman correlation coefficient of 0.17, and a slope of 0.16). However, the correlation with relation offset and red GC density profile steepness is even tighter and steeper, with a Spearman correlation coefficient of 0.72, with a p-value of 0.002, and a slope of 0.68 when removing the outlier NGC 1129.

We find that for the galaxies studied in this paper that whether a galaxy is classified as BCG or not does not have any significant affect on where it lies on the relation or on the trend with offset. This is likely because any non-BCGs studied in this sample are still NMCGs, with similar properties.

3.4 Discussion

3.4.1 Comparison with Simulations

First, let us compare the observational and theoretical $M_{GCS} - M_h$ relations shown in Figure 3.5. It can be seen that the Choksi and Gnedin 2019 model does an excellent job of predicting the positions of the Virgo Cluster galaxy members with halo masses greater than $10^{11} M_{\odot}$, with the exception of the BCG M87. However, its slope decreases past halo masses of $10^{13} M_{\odot}$ and the model ends up falling short of the GCS masses of the massive ellipticals (which are mostly BCGs and NMCGs) in our sample by about 0.3 dex. This offset is another representation of the long-known tendency of BCGs to have $2-3$ times higher specific frequencies compared with giant galaxies of the same luminosity but not located in central positions within their environments (e.g. Harris and van den Bergh 1981; Peng et al. 2008; Harris et al. 2013). The archetype of this difference is the pair of Virgo giants, M87 and M49, but another good example is the pairing of NGC 4874 and 4889 in Coma. Essentially, the Choksi and Gnedin (2019) model does well at matching the luminous non-BCGs in the list but underpredicts the BCGs.

A potential explanation for this discrepancy was offered by Choksi and Gnedin 2019, as they note that it was found by Li and Gnedin 2019 that the GC initial mass function can shift to higher masses when the host galaxy experiences a major merger. This in turn increases the likelihood of much more massive GCs forming, which allows for more clusters to survive to present-day. However, the Choksi and Gnedin 2019 model used a merger-independent cluster formation rate, meaning they did not take this GC initial mass function shift into account. This would explain why the model would succeed in predicting the locations of lower-mass and non-BCG Virgo cluster members, as these galaxies have experienced comparatively less major mergers than the BCGs and NMCGs in our sample.

The Chen and Gnedin 2023 model, when compared to our Local Group observational sample here, appears to over-predict the GCS masses of these dwarf galaxies in Figure 3.5. However, this opposite effect appears to be at least in part because our Local Group sample, although chosen due to the higher confidence in the estimated masses, does not fully capture the extremely high scatter in the $M_{GCS} - M_h$ relation in this mass range. Figure 5 in Chen and Gnedin 2023 shows the model alongside data from Forbes et al. 2018 which illustrates this clearly. The addition of many more dwarfs with carefully determined GC numbers would be an important step, and will be the subject of a later paper (see Section 3.4.4).

3.4.2 Drivers of Relation Offset

With the compilation of a homogeneous sample of massive elliptical galaxies in this paper, the extrinsic scatter in the $M_{GCS} - M_h$ relation has been minimized. Now we may investigate the intrinsic scatter in the relation to determine the physical processes pushing galaxies' GCS masses higher or lower than expected for their halo masses. The results from Figure 3.6 shows that shallow density profiles for red GCs correlate the strongest with positive offset from the $M_{GCS} - M_h$ relation.

It has been seen observationally that GC metallicity, and by extent, colour, is related to age, across host galaxy scales (Côté et al. 1998; Katz and Ricotti 2014; Fahrion et al. 2020b; Escudero et al. 2022). In general, it is found that red GCs tend to be formed *in-situ* and blue GCs *ex-situ*, making their way into massive galaxies like the ones in this sample via accretion of smaller satellites. Because of this, it has also been found that the spatial and kinematic properties of both GC populations also differ, with blue GC profiles being more extended and shallow than the red GC profiles in the same galaxy (Kluge et al. 2023; Belokurov and Kravtsov 2024; Veršič et al. 2024). As such, it is not surprising to find that the galaxies in our sample have differing red and blue GC density profiles slopes or trends with relation offset.

However, one would assume that since blue GCs tend to be formed *ex-situ* they would trace rich merger histories more readily and thus be the population driving a trend with offset from the $M_{GCS} - M_h$ relation, not the red GCs. The result that we see instead implies that purely the number of mergers a galaxy has undergone does not determine its position on the relation, but rather the *type* of mergers. The population of red GCs hosted by a massive elliptical can either be formed *in-situ* or be accreted from a major merger with another massive elliptical which hosts many old, red GCs. Thus, the results of Figure 3.6 implies that having experienced many minor mergers does little to drive a galaxy's GCS mass above what is expected for its halo mass, but a few major mergers will.

This result is in agreement with what was found by Kluge and Bender 2023, who studied surface brightness profiles around BCGs, rather than GCS profiles. They found that the “excess light” that BCGs host, making them more luminous than very massive normal elliptical galaxies, must be caused by major mergers with other massive ellipticals, with minor mergers playing a comparatively smaller role.

It should be noted that the galaxy NGC 1129 is excluded from the fit for this trend. This is the galaxy in our sample with the most shallow red GC density profile, yet it lies below the relation. NGC 1129 has been know to have a peculiar morphology for decades, with observations indicating a perpendicular light profile to its major axis (Peletier et al. 1990; Goullaud et al. 2018; Ene et al. 2020), a twisted stellar kinematic profile to its major axis (Veale et al. 2017), and a double-core at its centre (Lyman et al. 2016). All of these observations indicate that NGC 1129 has undergone a recent, major merger, unlike the other galaxies in our sample.

3.4.3 Comparison of $M_{GCS} - M_h$ Slopes Between Galaxy Samples

This interpretation of the cause of galaxy offset from the $M_{GCS} - M_h$ relation is supported by the differing slopes and intercepts of the relation for the Virgo cluster and massive galaxy samples. Table 3.3 shows that when studied individually, both the Virgo cluster sample (comprised mostly of galaxies below the BCG mass regime) and the massive galaxy sample studied here have relatively similar slopes, close to a 1:1 ratio. However, their intercepts differ, with the massive galaxy sample $\log(M_{GCS})$ values sitting systematically higher than those for the Virgo cluster sample. When the linear fits of the two samples are compared using the Chow test (Chow 1960), we find a Chow statistic of 8.1 and a p-value of 0.0005, indicating that the difference in linear fits is statistically significant.

In this picture, our sample of massive galaxies have all experienced a higher number of mergers than the Virgo cluster galaxies, and of those mergers, the major mergers have accreted more massive ellitptical galaxies. Thus, systematically it would be expected that they would all have a positive offset from the global $M_{GCS} - M_h$ relation. In fact, it can be seen in Figure 3.5 that M87, the Virgo cluster BCG, sits above all other Virgo galaxies, right alongside this paper’s massive galaxy sample. Of the six non-BCG Virgo galaxies with $M_h > 10^{13} M_\odot$ four seem to sit on the negative-most offset boundary of the massive galaxy sample (NGC 4649, NGC 4374, NGC 4365, and NGC 4406) and two appear to be more in line with the Virgo cluster sample relation (NGC 4472, NGC 4382). The four with similar positions to the massive galaxy sample have central positions in the Virgo A subcluster and could be considered NMCGs, or in the case of NGC 4365 is the central galaxy to a separate galaxy group (Blom et al. 2014). On the other hand, NGC 4472 (M49), while also being a central galaxy and the Virgo sample galaxy with the highest M_h, sits at the centre of the smaller Virgo B subcluster. NGC 4382, the lowest mass Virgo galaxy with a M_h still above $10^{13} M_\odot$, sits on the outskirts of the Virgo A subcluster, and would be considered a normal luminous elliptical rather than a BCG or NMCG.

It has been a subject of debate whether the high-mass end of the $M_{GCS} - M_h$ relation is genuinely linear or begins to display a downward curve (Harris et al. 2017; Boylan-Kolchin 2017; Choksi and Gnedin 2019; El-Badry et al. 2019b). The results of this paper would suggest that past work which have indicated a curvature of the $M_{GCS} - M_h$ relation may have simply used an observational sample of massive galaxies with fewer major mergers, or simulations which did not fully account for major mergers or did not use accurate GC disruption formation and disruption rates for BCGs. Both of these scenarios might result in only galaxies lying below $M_{GCS} - M_h$ relation and giving the appearance of a downward curve.

Interestingly, in Figure 3.5 we can see that all five galaxy clusters are at the top end of the mass range but lie below the relation defined by the individual galaxies. This is expected, as the majority of GCs hosted by these massive clusters are either currently being hosted, or would have been originally formed in, smaller galaxies with lower specific GC frequencies (Harris et al. 2013; Moreno-Hilario et al. 2024b). Thus, these galaxy clusters' total GC specific frequencies are lower than for individual BCGs, putting them below the relation.

3.4.4 Future Work

In order to further investigate this difference in positions between the massive Virgo cluster sample galaxies and the massive galaxy sample studied in this paper, GCSs from very massive but *non-central* galaxies must be studied. This would allow for a clearer understanding of how much merger history can drive galaxies above or below the relation.

In addition, a similar study to this one can be conducted with a sample of Milky Way mass galaxies to determine if there exists the same trend with GC profile slope and $M_{GCS} - M_h$ relation offset in lower mass regimes. For these lower-mass galaxies there will be other observational considerations to take into account due to their differing merger histories and mass contents from BCGs. For example, major mergers likely will not be depositing older, red populations of GCs, and thus any trend we observe would likely be with blue GCs instead. As well, GCs hosted by lower-mass galaxies also tend to be, on average, lower-mass themselves (see Equation 3.3) (Villegas et al. 2010; Harris et al. 2013). Thus, major mergers for Milky Way-like galaxies may disrupt more of the GC population than for massive ellipticals, but also due to their higher gas mass, at early enough times these mergers could also increase GC formation (Newton et al. 2024).

Finally, it would also be greatly beneficial for a study such as this to be applied to a sample of dwarf galaxies. However, in order to determine the drivers of intrinsic scatter in this relation, extrinsic scatter from differing observational methods must first be minimized. The low-mass end of the $M_{GCS} - M_h$ relation is dominated by scatter (Georgiev et al. 2010; Forbes et al. 2018; Berek et al. 2024), in part due to the observational difficulties in observing the complete GCSs of these small, dim galaxies, and in having enough luminous tracers at high enough radii to get accurate estimates of total halo masses. As well, there exists a diversity of dwarf galaxy morphologies, GC specific frequencies, and mass-to-light ratios that are likely also driving the intrinsic scatter in the relation (Gannon et al. 2022; van Dokkum et al. 2024; Li et al. 2024). The compilation of a literature catalog of dwarf galaxies with standardized GC counts and halo masses will be the subject of an upcoming paper.

3.5 Conclusions

In this work we studied the GCSs of 27 BCGs and NMCGs using HST data and a new Voronoi-tessellation based technique to determine accurate GC radial density profiles. For 16 of the 27 galaxies in our sample with colour information we determined the profiles for both the red and blue GC populations for each galaxy. We were able to plot this sample of massive galaxies alongside Virgo cluster galaxies and Local Group dwarf galaxies on the $M_{GCS} - M_h$ relation, spanning seven decades of GCS masses, the most complete observational view of this relation to date. From this, we found the following results:

1. We found the $M_{GCS} - M_h$ relation across all galaxy masses to be slightly steeper than 1:1 linearity, with a slope of 1.10, however this is only present when connecting our BCG and non-BCG samples. The $M_{GCS} - M_h$ relation for non-BCG galaxies has a slope of 1.05.
2. The nearly 1:1 linear $M_{GCS} - M_h$ relation holds for extremely massive, central galaxies, with a slope of 0.93. However, our massive galaxy sample is systematically shifted to higher GCS masses than for lower-mass galaxies.
3. There exists a negative trend with GCS radial density profile steepness and host galaxy offset from the $M_{GCS} - M_h$ relation, with galaxies with shallower GCS profiles being more likely to sit above the relation.
4. This trend is even tighter and steeper when considering the profiles of only the red GCs hosted by galaxies, and no trend exists for the profiles of only the blue GCs hosted by galaxies.
5. Thus, the red GC populations of the massive galaxies in our samples are driving this trend with offset, with the observed shallower red GC profiles having been caused by previous major mergers with other red-GC rich massive ellipticals.
6. The lack of trend with offset for blue GCs suggests that minor mergers, which deposit more blue GCs, do little to affect massive ellipticals' positions on the $M_{GCS} - M_h$ relation.
7. Therefore, we find that major mergers have the largest influence on intrinsic scatter around the $M_{GCS} - M_h$ relation for extremely massive, central, elliptical galaxies.

Chapter 4

Globular Cluster Systems in Dwarf Galaxies: Catalogs and Comparisons

The following chapter presents work towards a paper to be submitted to the Astrophysical Journal (ApJ), by Veronika Dornan & William E. Harris.

4.1 Introduction

Globular clusters (GCs) are a useful and frequently studied observational tracer of galaxy evolution. These dense stellar systems of up to 10^7 stars are some of the oldest objects in their host galaxies, with typical ages between 10 and 13 Gyrs (VandenBerg et al. 2013; Beasley 2020). Their compact sizes and high luminosities also allow them to be easily detectable at large distances (Reina-Campos et al. 2023; Joschko et al. 2024), which, when combined with their ubiquity (Harris et al. 2013; Le and Cooper 2025), means the number of GCs hosted are often included in photometric analyses of galaxies.

The properties of a galaxy's GCS today can be closely linked to the evolutionary history the host galaxy has undergone. It has been shown that GCSs can grow through galaxy mergers (Maji et al. 2017; Lahén et al. 2019; Newton et al. 2024; Dornan and Harris 2025), and can also be destroyed via mergers or tidal interactions with other, more massive galaxies (Gnedin et al. 1999; Kruijssen et al. 2011). Comparing the global properties of galaxies to the properties of their GC systems (GCSs) can give clues about these galaxies' merger histories or previous tidal interactions.

One way to probe the connection GCSs have with their host galaxies is through a galaxy's position on the GCS - halo mass ($M_{GCS} - M_h$) scaling relation. This linear relation between the mass of a galaxy's GCS and its total halo mass has been studied extensively, both through observations (Blakeslee et al. 1997; Blakeslee 1999; Spitler and Forbes 2009; Hudson et al. 2014; Harris et al. 2017; Forbes et al. 2018; Dornan and Harris 2025; Saifollahi et al. 2025a) and simulations (Kravtsov and Gnedin 2005; Kruijssen 2015; El-Badry et al. 2019b; Choksi and Gnedin 2019; Bastian et al. 2020; Valenzuela et al. 2021). This relation can tell us if certain classes of galaxies have experienced events that formed or accreted excess GCs for their masses (Forbes et al. 2025; Dornan and Harris 2025), and what those events may have been.

While massive galaxies are found to consistently (and tightly) follow the $M_{GCS} - M_h$ scaling relation (Harris et al. 2017; Dornan and Harris 2023; Dornan and Harris 2025), the scatter observed in this relation for dwarf galaxies increases significantly (Georgiev et al. 2010; Forbes et al. 2018; Prole et al. 2019). As a result, while the GCS mass for a galaxy with a stellar mass $\gtrsim 10^{10} M_\odot$ can be well predicted using this relation, dwarf galaxies have a wide range of possible GCS masses per unit stellar mass (Burkert and Forbes 2020; Eadie et al. 2022). Unlike massive galaxies, some dwarf galaxies can deviate very strongly from the expected $M_{GCS} - M_h$ relation by hosting no GCs at all (Eadie et al. 2022; Berek et al. 2024). While $N_{GC} = 0$ should not be unexpected for dwarfs with stellar masses below $M_\star \lesssim 10^7 M_\odot$, where the expected average N_{GC} is smaller than the dispersion in the relation, puzzlingly galaxies with stellar masses as high as $M_\star \sim 10^9 M_\odot$ have been found to lack GCs (Peng et al. 2008; Georgiev et al. 2010). It is currently unclear if these galaxies formed without GCs, once hosted GCs which have now been destroyed, or host very faint or obscured GCs that have yet to be detected.

In order to fully understand the cause of this wide range in GCS masses for dwarfs, it is necessary to isolate the scatter in the $M_{GCS} - M_h$ relation that is caused by physical processes affecting dwarf galaxies and their GCSs from the scatter caused by differing observational techniques between surveys and studies. While there are many excellent studies of dwarf galaxy GCSs (see Section 4.2), it can be difficult to compare the data from these studies to one another on the $M_{GCS} - M_h$ relation as the methods used to determine total number of GCs (N_{GC}), GCS masses, and halo masses can vary. This work aims to compile the data from surveys and catalogs already available in the literature and clearly lay out the differing methods applied in the photometric analyses of the GCSs and determine M_{GCS} and M_h estimates for these galaxies using consistent methods. This not only allows for the positions of these galaxies on the $M_{GCS} - M_h$ relation to be properly compared to one another, but also provides a convenient, public catalog of the data from several major dwarf galaxy GCS surveys.

In this work we list the surveys and catalogs included in our combined catalog and compare the methods employed by each to obtain their N_{GC} estimates in Section 4.2. We then detail the scaling relations used to determine GCS and peak halo masses for all galaxies in our combined catalog in Section 4.3. With these data, we then plot the positions of all galaxies in the combined catalog on the $M_{GCS} - M_h$ relation as well as the $N_{GC} - M_\star$ and $N_{GC} - M_h$ scaling relations, and compare the positions of classical dwarfs to those of ultra diffuse galaxies (UDGs), extremely low surface-brightness galaxies (ELSBGs, see Section 4.4.3), and massive galaxies in Section 4.4. Finally we discuss the implications of these results and summarize our findings in Sections 4.5 and 4.6 and briefly discuss necessary future work in this field in Section 4.7.

4.2 Catalog and Individual Survey Notes

This literature catalog is comprised of eight dwarf galaxy surveys and previously published literature catalogs. These surveys and catalogs vary in the data available for their GCSs and host galaxies, but all have N_{GC} estimates as well as total V-band absolute magnitudes and/or total stellar masses of the host galaxies. For the sake of purity of the combined sample, some data from the original surveys and catalogs have been omitted from the analysis done in this work. Data with the following criteria have been culled:

1. **Systems with N_{GC} estimates ≤ 0:** While there exist a large number of dwarf galaxies which host no GCs (see Section 4.1), in this work we will be considering only GC-hosting galaxies. This is because it is still unclear whether or not current non-GC-hosting galaxies originally hosted GCSs and have since had them fully disrupted, and/or because current non-GC-hosting galaxies may in fact host a handful of low-mass, dim GCs that we are

currently unable to reliably detect. As such, at this time we are omitting these galaxies from the combined catalog.

2. **Systems with N_{GC} uncertainties greater than N_{GC} estimates:** In line with the above reasoning, we are restricting our combined sample to galaxies with N_{GC} estimates with at least *one* confident GC candidate.

The above criteria biases our GCS catalog to somewhat more massive dwarf GCSs. Future steps to address this bias and include systems with no GCs are discussed in Section 4.7.

Below we lay out the differing photometric methods and assumptions used by each survey and catalog included in our combined catalog. At the end of this section we summarize the important differences and similarities that should be taken into consideration when comparing the results of each of these GCS samples.

4.2.1 ACS Virgo Cluster Survey and ACS Fornax Cluster Survey

The data from the ACS Virgo Cluster Survey is taken from Peng et al. 2008, which studied the GCSs of early-type galaxies in the Virgo cluster, resulting in a large, homogeneous GCS catalog. This catalog spans a large range of host galaxy stellar masses, so we only include 63 galaxies with $M_\star \leq 2 \times 10^{10} M_\odot$ in our combined catalog. The data from the ACS Fornax Cluster survey is taken from Liu et al. 2019, which used nearly identical methods and imaging to the ACS Virgo Cluster Survey but applied to the Fornax Cluster, functionally homogeneously extending the Virgo survey. We include 16 galaxies from this survey in our combined catalog.

All imaging for these two surveys was conducted with the Hubble Space Telescope (HST) advanced camera for surveys (ACS) using the F475W and F850LP filters, which roughly correspond to the Sloan Digital Sky Survey (SDSS) g and z bands. GC candidates were only included if they were detected in both filters. GC candidates were selected on the basis of colour, size, and magnitude. They selected objects with colours between $0.5 < g - z < 2.0$, which is a wide range intended to include the full range of ages and metallicities typical of old star clusters. They next plotted all potential GC candidates on a size-magnitude diagram and determined a maximum likelihood estimation for each galaxy's objects to assign a GC probability value. Only objects with a GC probability > 0.5 were selected.

Finally, to obtain a N_{GC} estimate they conducted completeness corrections based on their limiting magnitudes and adopted dwarf galaxy GC luminosity function (GCLF). This correction was minimal, as they estimate that at the depth of their imaging the brightest $\sim 90\%$ of each galaxy's GCSs was recovered. They adopted the GCLF derived in Jordán et al. 2007, which was determined through stacking GC photometry data from 89 of the galaxies in the ACS Virgo Cluster survey.

The stellar masses of these galaxies were determined using $M_\star/L_B$ mass-to-light ratios determined for each galaxy from the Bruzual and Charlot 2003 models. To determine these ratios they used a combination of their $g-z$ colours and J - K colours from the Two Micron All Sky Survey Extended Source Catalog.

4.2.2 Fornax Deep Survey

The data from the Deep Fornax Cluster Survey is taken from Prole et al. 2019, which studied the GCSs of low surface brightness galaxies around the central brightest cluster galaxy of the ACS Fornax Survey. We include 170 galaxies for this survey in our combined catalog.

The imaging for these galaxies was obtained using the VLT Survey Telescope/OmegaCAM instrument in the *u, g, r* & *i* bands. GC candidates were selected based on ellipticity, magnitude, and colour. Objects were selected if they had minor-to-major axis ratios greater than $(b/a) > 0.95$, g-band apparent magnitudes greater than $m_g > 19$, and had colours within the following ranges: $-0.18 < g-r < 1.23$, $0.32 < g-i < 2.00$, and $0.37 < u-g < 5.07$.

Total GC counts were determined using a Bayesian mixture model to determine dwarf galaxy and background GC membership, represented by a Plummer profile and a uniform distribution, respectively. An MCMC code was run to determine the half-light radius of each galaxy and the fraction of GC candidates belonging to the target galaxy.

They also applied GC completeness corrections adopting a GCLF with the same form as in Villegas et al. 2010 which studied the GCSs of Fornax galaxy dwarfs, although at brighter total magnitudes than the dwarfs in the Fornax Deep Survey. They estimate their GC completeness to be between $\sim 60\% - 90\%$, resulting in somewhat higher corrections needed for their lower-luminosity galaxies than was needed for the other surveys. The stellar masses of their galaxies were determined using equation 8 in Taylor et al. 2011 and their M_i magnitudes and $g-i$ colours, shown below.

$$\log(M_\star/M_\odot) = 1.15 + 0.70(g - i) - 0.4M_i \tag{4.1}$$

4.2.3 ELVES Survey

The data from the Exploration of Local VolumE Satellites (ELVES) Survey is taken from Carlsten et al. 2022, which studied the GCSs of early-type satellites of Milky Way-like and small group galaxies in the Local Volume. We include 25 galaxies from this survey in our combined catalog.

The imaging for these galaxies came from a mixture of archival CFHT/MegaCam, DECam Legacy Survey (DeCaLs), and Subaru/Hyper Suprime-Cam imaging. They note that the CFHT and Subaru imaging are both deeper than the DeCaLs imaging. All galaxies were imaged in the g-band as well as either the i-band or r-band. The individual filters used are all SDSS-like, but do differ somewhat between cameras. However the authors show that this difference is less than 0.1 magnitude and does not significantly affect their results.

GC candidates were selected via colour and magnitude cuts. They restricted their candidates to objects with colours between $0.1 < g - r < 0.9$ or $0.2 < g - i < 1.1$, intended to cover the full range of dwarf galaxy GC colours observed in Prole et al. 2019 (see section 4.2.2). Candidates were also restricted to absolute g-band magnitudes between $-9.5 < M_g < -5.5$ to cover the expected GCLF. They then applied two different methods to determine GC abundance; a simple background selection and a likelihood-based inference.

They perform completeness corrections assuming a Jordán et al. 2007 GCLF for their galaxies, as they found that the properties of this GCLF are very similar to those for Local Volume and Virgo cluster dwarf galaxies. Their imaging is also deep enough that these corrections are minimal, resulting in corrections of $\lesssim 5\%$ for their N_{GC} estimates. The stellar masses of their galaxies were determined using a mass-to-light ratio of $M_\star/L_g = 1.24$, derived from Into and Portinari 2013 using $g - i = 0.74$, the average galaxy colour in their sample.

4.2.4 MATLAS Survey

The data from the Mass Assembly of early-Type GaLAxies with their fine Structures (MATLAS) Survey is taken from Marleau et al. 2024, which studied 74 UDGs within the larger survey. We include 27 galaxies from this study in our combined catalog.

The GC imaging for these galaxies was taken with HST using the ACS in the F606W and F814W filters, which roughly correspond to the SDSS r and i bands. We also used global colour information for these galaxies taken from Poulain et al. 2021, which imaged them using CFHT in the g and r bands (with the exception of MATLAS-342, which was imaged in the g and i bands).

GC candidates were selected based on colour and concentration. GCs were selected with colours between $0.5 < (m_{F606W} - m_{F814W})_0 < 1.2$ and concentration indices between $0.1 < \Delta m_{4-8} < 0.5$ for galaxies within 25 Mpc and between $-0.1 < \Delta m_{4-8} < 0.5$ for galaxies beyond 25 Mpc. The concentration indices here represent the difference in apparent magnitude in the F606W band for a GC when observed using a 4 vs 8 pixel diameter aperture. GCs were considered hosted by the target galaxy if they are within $2R_e$, and those found beyond $2R_e$ were used to determine GC background contamination.

Finally, they performed a completeness correction assuming a GCLF of the form used in Miller and Lotz 2007, which was determined using dwarf galaxies in the Virgo and Fornax Clusters and the Leo Group. The stellar masses of these galaxies were not listed in Marleau et al. 2024, so they were determined independently here using the colours from Poulain et al. 2021 and the colour-mass-to-light ratio relations in Into and Portinari 2013, for consistency with the ELVES survey stellar masses.

4.2.5 Georgiev Catalog

Georgiev et al. 2010 compiles the GCSs of 41 faint, late-type dwarf galaxies in low-density environment, of which we include 40 in our combined catalog. The only galaxy to be omitted from this catalog was the SMC, as since the publication of Georgiev et al. 2010, it has been determined that the SMC could actually be two distinct structures which are superimposed on each other in our line of sight (Murray et al. 2019; Murray et al. 2024). As a result, the stellar mass estimate of the SMC quoted in Georgiev et al. 2010 is very likely an overestimate and should not be included in this combined dwarf catalog.

This catalog uses HST archival imaging in the F606W and F814W filters. GC candidates were selected based on colour, ellipticity, size, and concentration cuts. GCs were selected with colours between $-0.4 < (m_{F606W} - m_{F814W})_o < 0.15$, ellipticities below $e < 0.15$, full width half maxima (FWHM) between $2 < FWHM < 9$ pixels, and concentration indices above $\Delta m_{2-3} > 0.4$.

They estimate, due to the depth of their imaging, that they have $\sim 90\%$ completeness for the GCSs and as a result choose not to apply a GCLF-based completeness correction. They determined their galaxy stellar masses using the colour-mass-to-light ratio relations in Bell et al. 2003.

4.2.6 Gannon Catalog

Gannon et al. 2024 compiles the GCSs of 33 UDGs, of which we include 19 in our combined catalog. This is a literature catalog which drew from studies of individual galaxies, oftentimes combining data from multiple studies of the same galaxy, and as such does not have any singularly standardized photometric parameters or GC detection methodology. As such, while the GC detection methods for these galaxies may vary, the N_{GC} estimates can be taken as reliable lower bounds. In addition, half of the UDGs included here from the Gannon et al. 2024 catalog had data taken from the same two studies (N_{GC} values taken from Lim et al. 2020 and stellar masses taken from Toloba et al. 2023), which would make them internally self-consistent. A full list of the original papers this catalog draws from can be found in Appendix A. For more information on this data, please refer to the original papers.

4.2.7 Comparison of Surveys and Catalogs

Broadly, the assumptions made for determining the GCS properties of the dwarf galaxies in each survey are similar enough to be compared to one another, however there are differences that can have systematic impacts on the final N_{GC} estimates.

Table 4.1: Survey Comparison

Survey	Instrument	Mag Limit	Resolution (“/pixel)	Distance (Mpc)	Filters	Colour Cuts	GCLF Peak M_g
ACS Virgo/Fornax	ACS	$m_g \sim 26$	0.05	$\sim 16/19$	g,z	$0.5 < g - z < 2.0$	-7.2 ± 0.2
Fornax Deep	OmegaCAM	$m_g \sim 25$	0.21	~ 19	u,g,r,i	$-0.18 < g - r < 1.23$ $0.32 < g - i < 2.00$ $0.37 < u - g < 5.07$	-7.1 ± 0.2
ELVES	HSC MegaCam DECam	$m_g \sim 24$	0.4 0.19 0.26	< 12	g,r,i	$0.1 < g - r < 0.9$ $0.2 < g - i < 1.1$	-7.2 ± 0.2
MATLAS	ACS	$m_g \sim 24$	0.05	$17 - 46$	r,i	$0.5 < r - i < 1.2$	-7.1 ± 0.1
Georgiev+ (2010)	ACS	$m_V \sim 26$	0.05	< 9	r,i	$-0.4 < r - i < 0.15$	N/A

Key to columns: (1) Survey name; (2) Instrument used for imaging. ACS corresponds to HST, OmegaCam corresponds to VLT, HSC corresponds to Subaru, MegaCam corresponds to CFHT, and DECam corresponds to Víctor M. Blanco 4-meter Telescope; (3) Limiting GC magnitude of photometry; (4) Spatial resolution of photometry; (5) Distance to target galaxies; (6) SDSS-like filters used; (7) colour cuts applied for GC selection; (8) peak magnitude of the GCLF used for completeness corrections.

- **Depth of Imaging:** Deeper imaging allows for a more complete photometric census of the GCS. With deeper imaging, fainter GCs can be detected and completeness corrections become more minor.
- **Resolution of Imaging:** Higher resolution imaging also allows for smaller on-sky GC sizes to be reliably detected. Lower resolution imaging could result in larger (and therefore higher mass) GCs to be comparatively easier to detect, skewing average GC properties. Lower resolutions could also contribute to misidentifications of GC candidates, as it would make it more difficult to accurately determine object size and ellipticity.
- **Distance to Target:** Related to the above, targets that are closer will not require as deep imaging or high resolution to detect GCs of the same faintness or size as at further distances.
- **Filters Used:** All of the surveys included in this study select GCs based on colour cuts, so the same GC could be included or excluded when using different filters.
- **GC Candidate Selection:** In addition to differing filters, the specific criteria for GC selection can also vary, including the bounds for those criteria. Even with standardized GC criteria, however, there are also differing definitions for GC association with its target galaxy and methods of subtraction of background GCs.
- **GCLF Used for Completeness Corrections:** Finally, adopting a different GCLF will

change the completeness correction applied to the N_{GC} estimate. Thankfully, the majority of the surveys used here make minor corrections for completeness and used very similar GCLFs. See Figure 4.1 for a comparison of the GCLFs used by the different sources in this catalog.

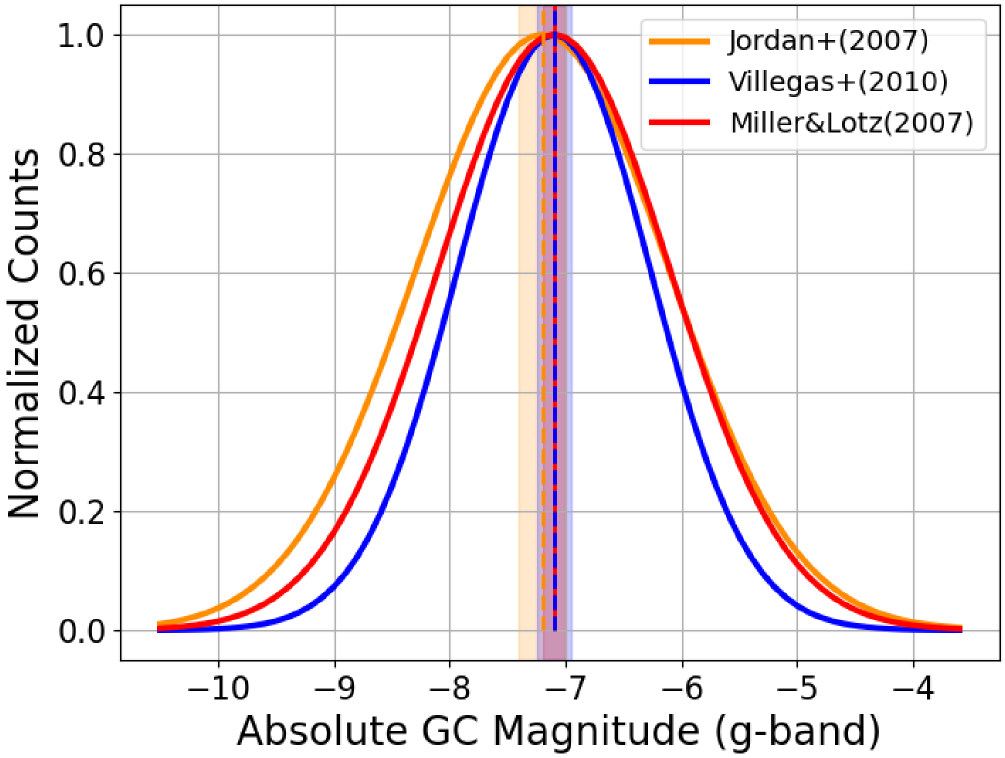

FIGURE 4.1: A comparison of the shapes of the three GCLFs used by the sources included in this catalog, from Jordán et al. 2007, Miller and Lotz 2007, and Villegas et al. 2010. All three GCLFs use a Gaussian form. The turnover magnitudes for all three are within uncertainties of each other. The low-luminosity ends of the GCLFs are similar in shape, but the high-luminosity ends begin to differ, however this does not affect the analysis, as the the GCs in these magnitude ranges are much more readily detectable and the GCLF is not being relied on for a completeness correction.

A direct comparison of the photometry, GC selection criteria, target properties, and GCLFs used by each survey is listed in Table 4.1. Overall, differences between the limiting magnitudes and GCLFs used for completeness corrections for these surveys are very small, however, the surveys begin to differ in terms of resolution, distance, and colour cuts.

Three of the surveys use HST/ACS imaging, resulting in identical resolutions. The Fornax Deep and ELVES surveys use a variety of ground-based telescopes with similar resolutions, but which are all nearly 4 times lower than HST/ACS. In addition, there is little agreement between the surveys in terms of the filters used for colour cuts. Those that do use the same filters still define their bounds quite differently, typically because they are trying to identify an area in a colour-colour or colour-concentration space for their GC selection. Each of these surveys make different trade-offs in terms of purity of their samples vs. completeness and should be considered when comparing the results in Section 4.4.

4.3 Mass Conversions

We plot given N_{GC} and $M_\star$ estimates for all of these surveys and catalogs in Figure 4.2. Many works which have studied GCS scaling relations for dwarf galaxies focus on the $N_{GC} - M_\star$ relation as a way to avoid having to make mass conversions with large uncertainties to obtain the more well-studied $M_{GCS} - M_h$ relation. However, to properly connect and compare the GCSs of dwarf galaxies to their more massive counterparts, the more linear $N_{GC} - M_h$ or $M_{GCS} - M_h$ relation is needed. First, let us begin with converting stellar masses to halo masses.

4.3.1 Stellar-to-Halo Masses

As was mentioned in the previous section, different surveys and catalogs in this work have used slightly different mass-to-light ratios to obtain their galaxy stellar masses, however from now on in our analysis we will treat them as consistent. Obtaining accurate halo masses for dwarf galaxies can be much more difficult than for higher mass galaxies. Dwarf galaxies' smaller sizes result in less material in the outer regions to be used to get accurate velocity dispersions to estimate the total dynamical masses. Although some of the works included in this combined catalog determine the dynamical masses of their galaxies, they take wildly different approaches.

The galaxies included in the sample from the Georgiev et al. 2010 catalog had stellar and HI gas kinematic data available to allow for mass estimates to be made, which was done by Forbes et al. 2018. Prole et al. 2019, on the other hand, determined the halo masses of their sample using the very $N_{GC} - M_h$ relation we are studying in this paper. As it currently stands, the most accurate way to estimate total masses for dwarf galaxies requires deep spectroscopic imaging to obtain the most complete kinematic data possible (Buzzo et al. 2025b; Haacke et al. 2025), an approach which is difficult to apply to a large sample of galaxies, and which may still fail for the faintest dwarfs with low stellar membership.

In order to be able to most accurately compare this combined catalog of dwarf galaxies to each other on the $M_{GCS} - M_h$ relation, we will apply a simple, but standard, conversion from stellar mass to peak halo mass. While there have been many recent studies of the behaviour of the stellar-to-halo-mass-relation (SHMR) (Garrison-Kimmel et al. 2017; Read et al. 2017; Behroozi et al. 2019; Nadler et al. 2020; Munshi et al. 2021; Manwadkar and Kravtsov 2022; Christensen et al. 2024), in the past decade the majority of these models have begun to converge for dwarf galaxies. While the choice of one model to use over the other for our mass conversions can affect the resulting halo masses of our sample slightly, due to the similarity of many of the most recent models (in fact, many are within uncertainties of each other for the mass range concerned here), that choice will not significantly affect our final results. Here we choose to apply the SHMR modeled by Danieli et al. 2023b, as it was determined using a semi-analytic model sampled from the ELVES survey, which is included in this combined catalog. This SHMR takes the following form:

$$\log(M_\star) = 10.457 - \log(10^{-2.10x} + 10^{-0.464x}) - 0.812 \exp\Big[- 0.5\Big(\frac{x}{0.319}\Big)^2\Big] \tag{4.2}$$

where:

$$x = \log\left(\frac{M_{peak}}{10^{11.889}}\right) \tag{4.3}$$

For galaxies in our sample, this $M_{peak} - M_\star$ relation behaves linearly with a constant scatter of $\sigma = 0.06^{+0.07}_{-0.05}$ (Danieli et al. 2023b). We incorporate this scatter into the error propagation for our peak halo mass estimates alongside the quoted uncertainties for the galaxies' stellar masses.

We would like to note that this SHMR is not necessarily between the stellar mass of the dwarf galaxy and its *present-day* halo mass, but rather with its *peak* halo mass. Other studies of the SHMR for dwarfs have found that when linking it to present-day halo mass there is significant degeneracy and scatter dependent on galaxies' interaction history with other, more massive galaxies (Munshi et al. 2021; Christensen et al. 2024). This degeneracy is significantly limited when instead comparing the current stellar mass to the highest halo mass the galaxy had in its lifetime. This difference in the SHMR for peak and present-day halo masses is driven by satellite galaxies, rather than centrals, which is also why this difference most affects the low-mass end of the SHMR. As galaxies originally form, they lie on the linear SHMR, but their dark matter halos can become stripped after infall into their parent halo, losing mass. On the other hand, their more centrally concentrated stellar populations largely survive this stripping and their stellar masses are retained (Munshi et al. 2021; Christensen et al. 2024). A more in-depth discussion of the implications of this use of peak halo mass over current halo mass for the $M_{GCS} - M_h$ relation can be found in Section 4.5. Regardless, we will still refer to the scaling relation as the $M_{GCS} - M_h$ relation in this work.

4.3.2 N_{GC}-to-GCS Masses

We also apply a simple, standard conversion from N_{GC} to GCS mass using the properties of the GC luminosity function (GCLF), and by extension GC mass function (GCMF), observed in dwarf galaxies. We take the peak of the GCLF to determine an average GC mass for a given galaxy ($\langle M_{GC} \rangle$), with the uncertainty on that mass equivalent to 1σ on the GCLF. We then simply multiply our N_{GC} estimates by $\langle M_{GC} \rangle$ to get an estimate of the total mass of the system.

Other studies have taken a single GCLF peak and $\langle M_{GC} \rangle$ and applied it to all of their galaxies to obtain M_{GCS} estimates (Forbes et al. 2018). However, there exists a shallow relation between $\langle M_{GC} \rangle$ and host galaxy dynamical mass (Harris et al. 2013), driven by the fact that the GCLF peak shifts to dimmer magnitudes for smaller galaxies (Jordán et al. 2007; Villegas et al. 2010). We adopt $\langle M_{GC} \rangle$ values for our galaxies based on this relation, as although the shift to lower average GC masses is small, for galaxies with only a handful of GCs it can more noticeably impact their position on the $M_{GCS} - M_h$ relation. This scaling relation takes the following form (Harris et al. 2013):

$$\langle M_{GC} \rangle = (2.26 \pm 10^4) \times M_{dyn}^{0.098} \tag{4.4}$$

We quote the uncertainty in our $\log\langle M_{GC}\rangle$ estimate as the vertical dispersion in the $\langle M_{GC}\rangle - M_{dyn}$ relation, stated in Harris et al. 2013 to be $\sigma_{\log\langle M_{GC}\rangle} = 0.086$. We incorporate this uncertainty into our error propagation for M_{GCS} alongside the quoted N_{GC} errors from the surveys and catalogs. For the Georgiev et al. 2010 catalog no errors on their N_{GC} estimates are stated so we use the same approach as Forbes et al. 2018, which adopted a 0.3 dex uncertainty on M_{GCS} for galaxies hosting less than 10 GCs, assuming Poisson-like uncertainties dominated systems of this size.

An important fact to note about the use of this $\langle M_{GC}\rangle - M_{dyn}$ relation, is that here we use the peak halo masses that were obtained from the SHMR as an estimate of M_{dyn}. While these peak halo masses are not identical to current M_{dyn}, and can in fact vary by up to an order of magnitude (Munshi et al. 2021; Christensen et al. 2024), the shallow dependence on M_{dyn} of the $\langle M_{GC}\rangle - M_{dyn}$ relation means that the changes in M_h from peak to present day results in only a minor change to the $\langle M_{GC}\rangle$ used. For example, a galaxy with $M_{h,peak} = 10^9 M_\odot$ and $M_{h,0} = 10^8 M_\odot$ would have its estimated $\langle M_{GC}\rangle$ values differ by less than $0.2 \times 10^4 M_\odot$, which is less than the uncertainty on the scatter in the $\langle M_{GC}\rangle - M_{dyn}$ relation itself.

4.4 Results

4.4.1 Scaling Relations

Here we plot where the galaxies included in this combined catalog sit on three different scaling relations: $N_{GC} - M_\star$, $N_{GC} - M_h$, and $M_{GCS} - M_h$. The first, N_{GC} vs stellar mass is commonly investigated by dwarf galaxy GCS studies (Eadie et al. 2022; Berek et al. 2024), and can be seen in Figure 4.2.

While this scaling relation limits the assumptions necessary when converting N_{GC} to M_{GCS} and $M_\star$ to M_h, it is a globally non-linear relation, with a break-point at $M_\star \sim 10^{11} M_\odot$. This is due to the fact that although this scaling relation is a by-product of that between N_{GC} and M_h, which remains linear even to the highest mass galaxies, this break in linearity arises from the same break in the non-linear SHMR.

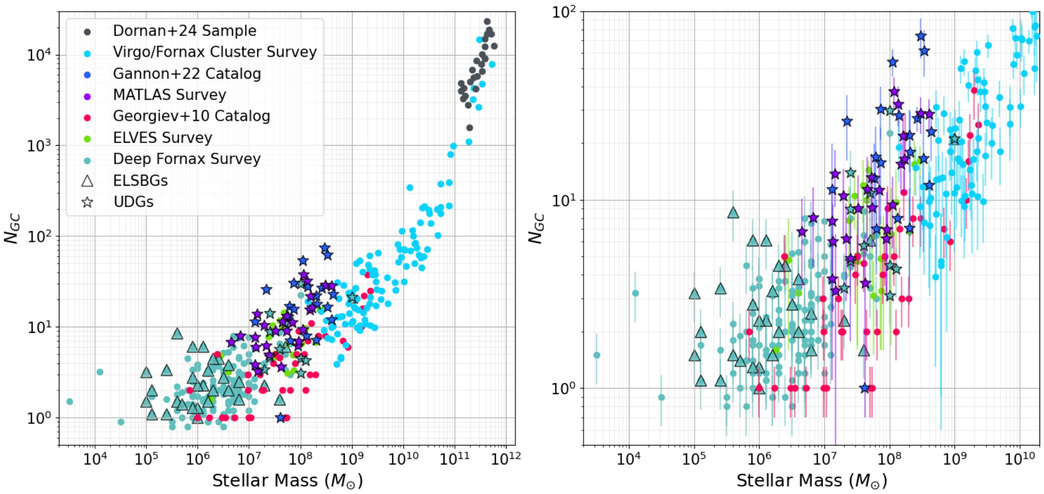

FIGURE 4.2: *Left:* N_{GC} vs host galaxy $M_\star$ for all galaxies in the combined sample and the more massive galaxies in the Virgo Cluster Catalog (Peng et al. 2008) and the BCGs in the Dornan and Harris 2025 sample. *Right:* Same as the left panel, but zoomed-in on the combined dwarf galaxy catalog only, and including N_{GC} errors. Stars denote galaxies classified as UDGs, triangles denote extremely low surface brightness galaxies ($\mu_{g,0} > 27$).

As such, it is more relevant to plot the $N_{GC} - M_h$ relation, as can be seen in Figure 4.3. Here, the scaling relation tightens and becomes linear across decades of peak halo mass. However, this linearity is still not fully universal. As we move to the lowest-mass dwarf galaxies in our combined catalog it is impossible to have fewer than ~ 1 GC, resulting in a flattening of the relation. However, as was discussed in section 4.3.2, the average mass of a GC in a galaxy scales with that host galaxy's dynamical mass.

In Figure 4.4 we plot the $M_{GCS} - M_h$ relation for our combined sample alongside the full ACS Virgo Cluster Survey and the Dornan and Harris 2025 BCG sample. The stellar masses adopted for these more massive galaxies were determined using the Hudson et al. 2015 SHMR. This is because the Danieli et al. 2023b SHMR was sampled from galaxies in the ELVES Survey, but did not include any galaxies with stellar masses above $M_\star > 10^{11} M_\odot$, with the majority of the galaxies having stellar masses well below that. However, the Hudson et al. 2015 SHMR sampled galaxies past $M_\star > 10^{11} M_\odot$ up into the BCG regime. This SHMR take the following form:

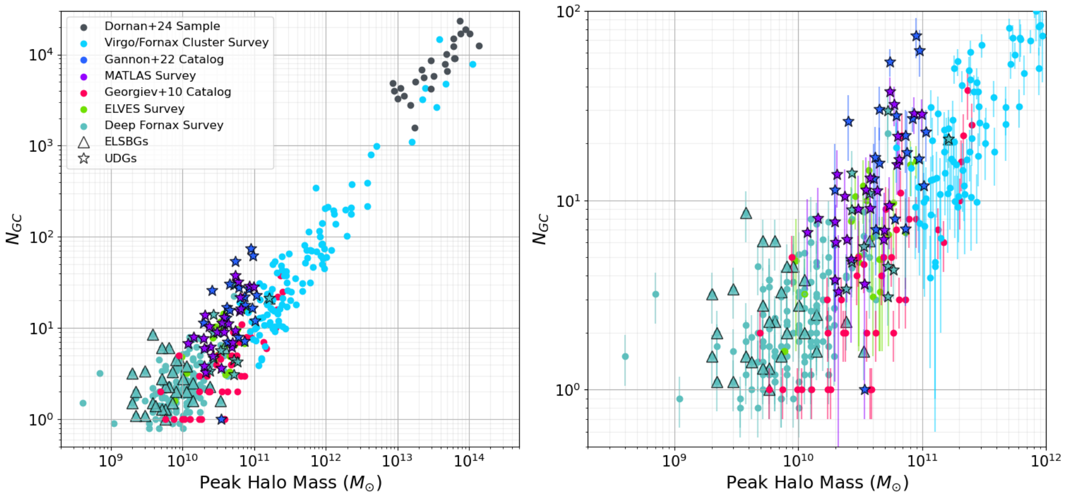

Figure 4.3: *Left:* N_{GC} vs peak M_h for all galaxies in the combined sample and the more massive galaxies in the Virgo Cluster Catalog (Peng et al. 2008) and the BCGs in the Dornan and Harris 2025 sample. *Right:* Same as the left panel, but zoomed-in on the combined dwarf galaxy catalog only, and including N_{GC} errors. Stars denote galaxies classified as UDGs, triangles denote extremely low surface brightness galaxies ($\mu_{g,0} > 27$).

$$M_\star/M_h = 2f_1\left[\left(\frac{M_\star}{M_1}\right)^{-0.43} + \frac{M_\star}{M_1}\right]^{-1} \tag{4.5}$$

Where M_1 is the transition or pivot halo mass, set to $10^{10.76}M_\odot$, and f_1 is the mass ratio at M_1, which is $f_1 = 0.0227$. Both SHMRs agree at $M_\star \sim 2.5\times10^{10}M_\odot$, the “knee” in the SHMR. Thus, for galaxies above this mass we use the Hudson et al. 2015 SHMR, and for galaxies below this mass we use the Danieli et al. 2023b SHMR, allowing for a smooth transition between the two SHMRs. We would like to note that, at this time, there has been no single study of the SHMR that has sampled galaxies from the full range of galactic stellar masses currently observed.

4.4.2 Fits to The $M_{GCS} - M_h$ Relation

Here we fit a linear regression to the full combined sample for both galaxies with stellar masses below $M_\star < 2\times10^{10}M_\odot$ and for an additional sample up to the BCG regime. This relation from massive galaxies to dwarf galaxies was previously studied in Dornan and Harris 2025, which used the full ACS Virgo Cluster Survey, a subset of Local Group dwarfs (Harris et al. 2013; Forbes et al. 2018; Forbes 2020), and a sample of BCGs. They found the $M_{GCS} - M_h$ relation for their

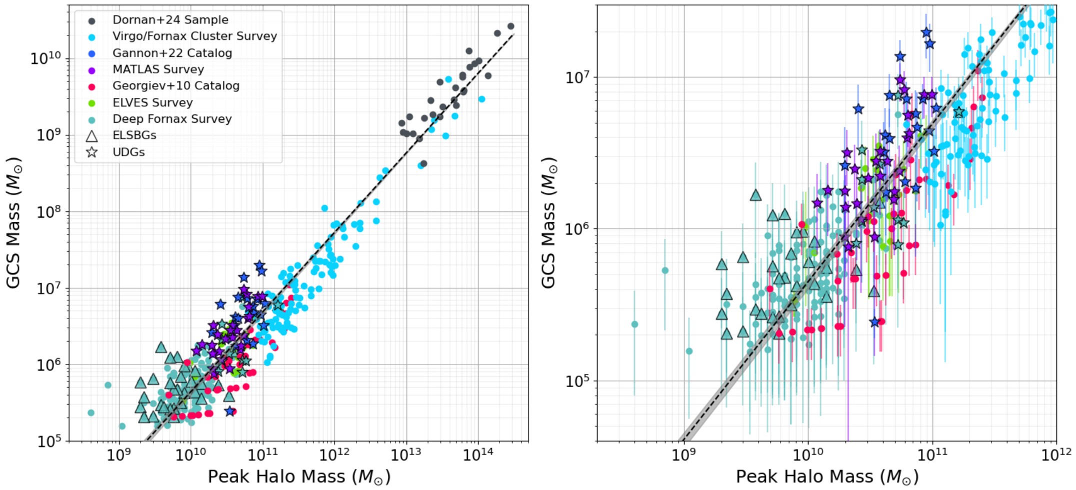

FIGURE 4.4: *Left:* M_{GCS} vs peak M_h for all galaxies in the combined sample and the more massive galaxies in the Virgo Cluster Catalog (Peng et al. 2008) and the BCGs in the Dornan and Harris 2025 sample. *Right:* Same as the left panel, but zoomed-in on the combined dwarf galaxy catalog only, and including M_{GCS} errors. Stars denote galaxies classified as UDGs, triangles denote extremely low surface brightness galaxies ($\mu_{g,0} > 27$).

TABLE 4.2: Linear Fit Solutions for $M_{GCS} - M_h$ Relation

Sample Combination (1)	Slope (2)	Intercept (3)
Dwarfs + Full Virgo + BCGs	1.04 ± 0.01	-4.75 ± 0.15
Non-UDG/ELSBG Dwarfs + Full Virgo	0.95 ± 0.02	-3.85 ± 0.19
Dwarf Catalog Only	0.89 ± 0.02	-3.14 ± 0.26
Non-UDG/ELSBG Dwarfs Only	0.90 ± 0.02	-3.37 ± 0.25
UDGs Only	1.42 ± 0.18	-8.61 ± 1.93
ESLBGs Only	0.46 ± 0.12	1.26 ± 1.21
UDGs + ESLBGs	1.02 ± 0.08	-4.31 ± 0.86

Key to columns: (1) Combination of observational samples used for the linear fits: either all of them, only one, or a combination of two; (2) The slope of the fit in log-log space; (3) The intercept of the fit in log-log space.

full sample to behave as $\log(M_{GCS}) = (1.10 \pm 0.02)\log(M_h) - (5.64 \pm 0.89)$, with the BCG sample being offset above this fit due to richer merger histories than other galaxies in the sample.

We replaced the Local Group sample used in Dornan and Harris 2025 with our combined dwarf galaxy catalog and fit it alongside the same massive galaxies used by them. We find that the $M_{GCS} - M_h$ relation behaves as $\log(M_{GCS}) = (1.04 \pm 0.01)\log(M_h) - (4.75 \pm 0.15)$, resulting in a slightly shallower slope, but with intercepts in agreement within errorbars.

When fitting for only the galaxies in our combined dwarf catalog, the $M_{GCS} - M_h$ relation behaves as $\log(M_{GCS}) = (0.89 \pm 0.02)\log(M_h) - (3.14 \pm 0.26)$, which is much shallower and offset lower than the global fit. This is driven by the exclusion of the positively offset BCG sample.

4.4.3 Ultra Diffuse Galaxies and Extremely Low Surface Brightness Galaxies

Within our combined dwarf galaxy catalog we also identify galaxies which meet the UDG classification criteria; with surface brightnesses above $\langle\mu_{g,0}\rangle > 24$ mag arcsec^2 and effective radii above $R_e > 1.5$ kpc (van Dokkum et al. 2015b). We also identify a subset of galaxies with effective radii below $R_e < 1.5$ kpc but with extreme surface brightnesses greater than $\langle\mu_{g,0}\rangle > 27$mag/arcsec^2, which we will refer to as extremely low surface brightness galaxies (ELSBGs). Our aim is to investigate if these galaxies are significantly, systematically offset from the $M_{GCS} - M_h$ relation and if this is unique to UDGs or if it is a byproduct of the mechanisms that create significantly low surface brightness galaxies, regardless of size and concentration.

First, we note that galaxies classified as UDGs occupy a narrow range in peak halo masses but a comparatively large range in GCS masses. The UDGs in our sample have peak halo masses between $10^{10}M_\odot \leq M_{h,peak} \leq 10^{11}M_\odot$ and GCS masses between $2 \times 10^5 M_\odot \leq M_{GCS} \leq 2 \times 10^7 M_\odot$. When determining the $M_{GCS} - M_h$ relation for our UDG subset we obtain a fit of $\log(M_{GCS}) = (1.42 \pm 0.18)\log(M_h) - (8.61 \pm 1.93)$.

We also fit the UDG and ELSBG subsample together. The ESLBGs occupy a similar range in peak halo masses as the UDGs, although shifted lower, but have a much smaller range in GCS mass ($2 \times 10^5 M_\odot \leq M_{GCS} \leq 2 \times 10^6 M_\odot$). When fitting the UDGs and the ELSBGs together we obtain a fit of $\log(M_{GCS}) = (1.02 \pm 0.08)\log(M_h) - (4.31 \pm 0.86)$, which has steeper slope compared to the non-UDG/ELSBG subsample, and shifted higher.

This shows that many very low-mass galaxies in our sample have similar positions on the $M_{GCS} - M_h$ relation as the ELSBGs, while the UDGs systematically occupy higher GCS masses than classical dwarfs of the same peak halo mass. It should be noted, however, that the majority of galaxies in this combined catalog with peak halo masses below $M_{peak} < 10^{10}M_\odot$ are part of the Fornax Deep Survey and all have surface brightnesses above $\langle\mu_{g,0}\rangle > 24$ mag arcsec^2 to begin with.

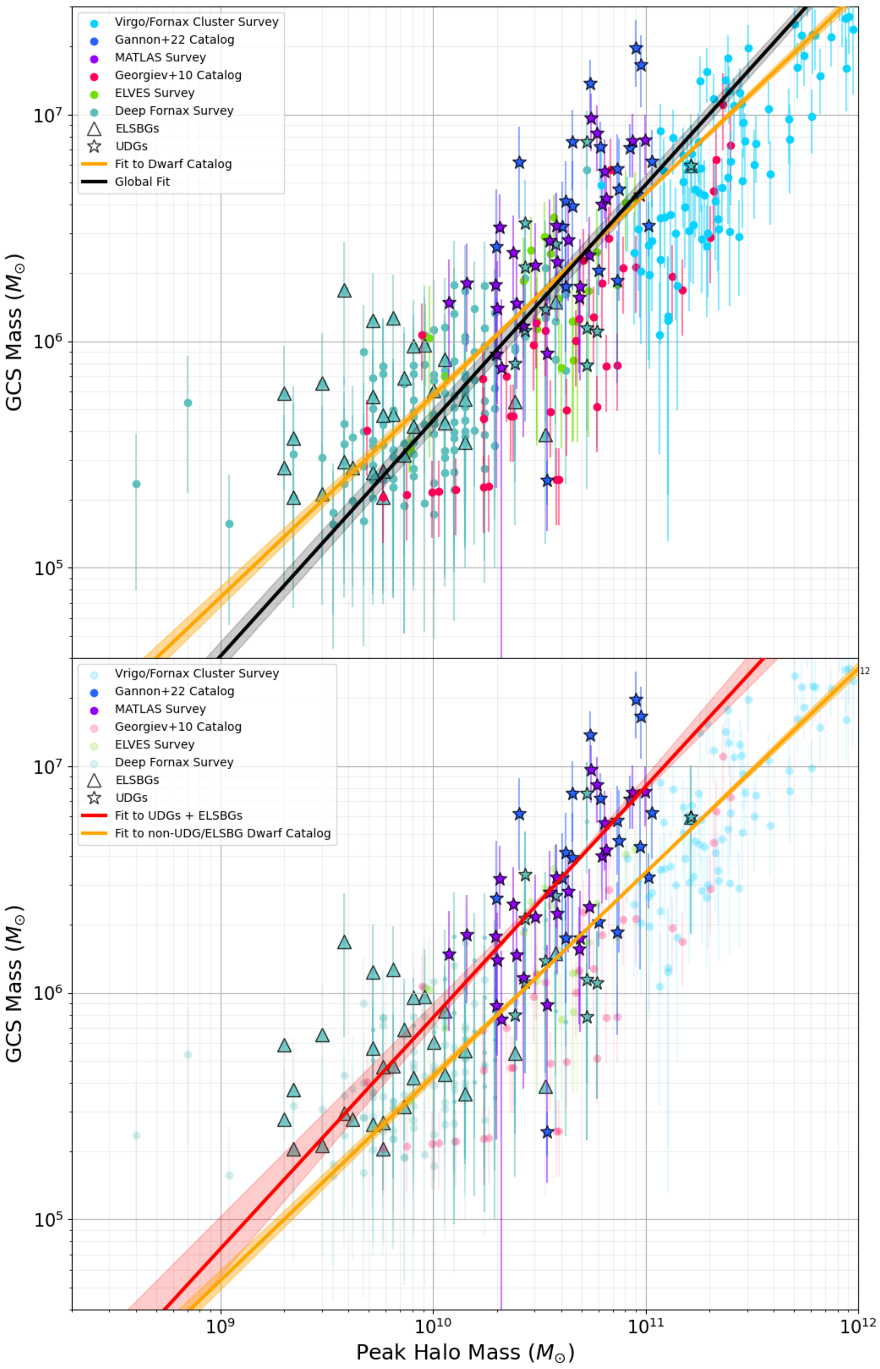

FIGURE 4.5: *Top:* M_{GCS} vs peak M_h for all galaxies in the combined catalog. *Bottom:* Same as the top panel, but now comparing the fit for the full dwarf catalog to the fit for only the UDGs and ELSBGs.

We find that low-mass ELSBGs lie in alignment with UDGs on the $M_{GCS} - M_h$ relation, with both being, on average, systematically positively offset from the relation in comparison to higher surface brightness dwarfs. This is in support of the result from Forbes et al. 2020, which studied the GCSs of 85 Coma cluster UDGs and found that rich GCSs were more likely to be hosted by UDGs of lower luminosity, smaller size, and fainter surface brightness. We will note however, that while UDGs almost exclusively occupy the highest GC specific mass frequencies for their stellar mass range here, other non-ELSBGs at very low stellar masses can also have as high GC specific frequencies as ELSBGs. We calculated the GC specific mass frequencies for all galaxies in our combined catalog, defined by equation 4.6 below (Zepf and Ashman 1993; Peng et al. 2008; Carlsten et al. 2022).

$$T_N = (10^9 M_\odot) \times N_{GC}/M_\star \tag{4.6}$$

Figure 4.6 plots GC specific mass frequency against stellar mass and illustrates this higher GC-richness for UDGs and ELSBGs, particularly the lowest mass ELSBGs, in our sample. We fit linear relations to all dwarfs in the catalog, the ESLBG sub-sample, and the UDG subsample in Figure 4.6, the parameters for which can be found in Table 4.3. We find that GC specific mass frequency scales tightly with stellar mass for the members of our dwarf galaxy catalog, with lower mass galaxies having higher T_N values. This relation between T_N and galaxy mass has been studied previously, sometimes comparing GC number specific frequency or GCS mass specific frequency, and sometimes comparing it to host galaxy absolute magnitude or dynamical mass. Regardless, a similar “U-shape” is consistently found, with a negative linear slope for low-mass galaxies, followed by an inflection around $M_\star \sim 10^{10} M_\odot$, and then a positive linear slope for high-mass galaxies (Peng et al. 2008; Harris et al. 2013; Choksi and Gnedin 2019).

When studying the relation between T_N and host galaxy stellar mass for low-mass galaxies, we notice that the UDG sub-sample has a similar slope to the dwarfs as a whole, but is shifted higher. This is consistent with UDGs, on average, having systematically higher GC specific mass frequencies than classical dwarfs. On the other hand, the ELSBG sub-sample has a steeper negative slope than the dwarfs as a whole, with only the lowest mass ESLBGs having T_N values

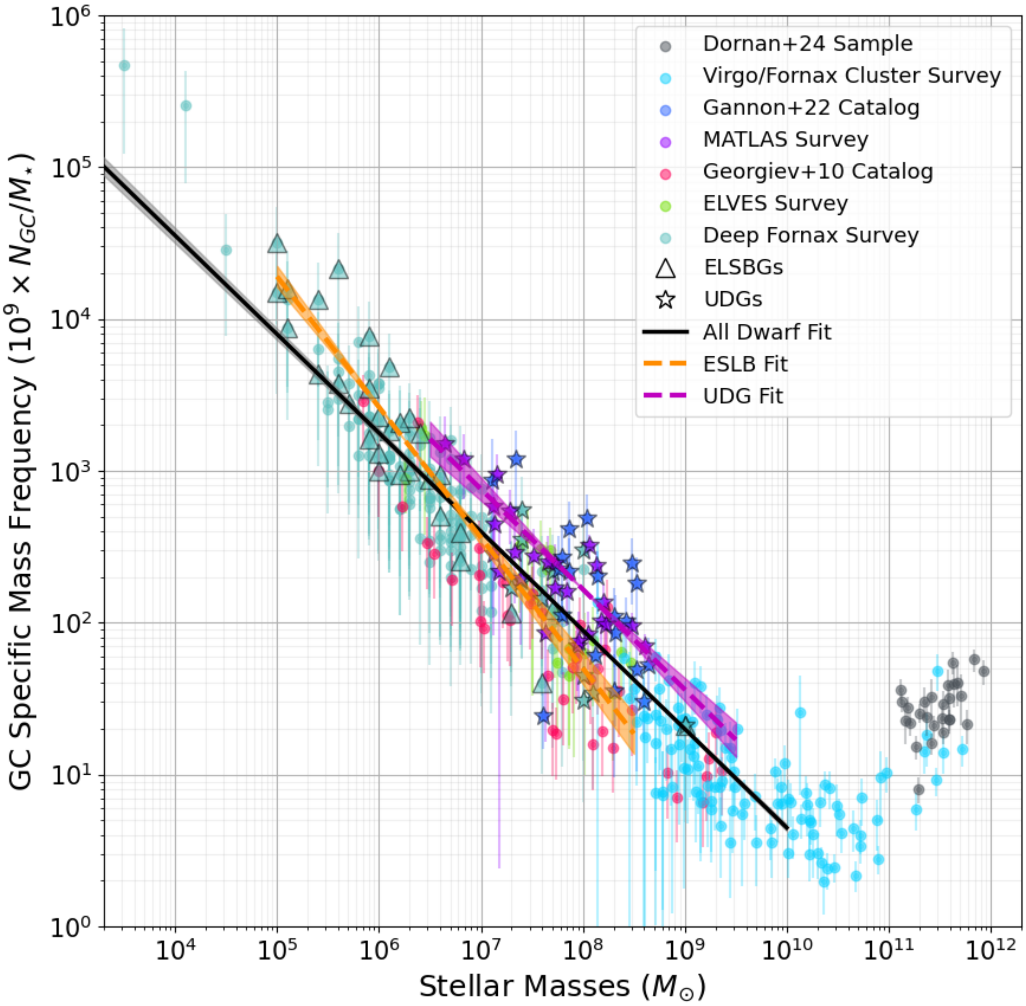

FIGURE 4.6: GC specifc mass frequency plotted against stellar mass for the combined dwarf galaxy catalog plus the massive Virgo cluster galaxies and the BCG sample. UDGs and ELSBGs are denoted by stars and triangles respectively. The fit for all dwarfs is plotted in black, the fit for UDGs only is plotted in purple, and the fit for ESLBGs only is plotted in red.

TABLE 4.3: Linear Fit Solutions for $T_N - M_\star$ Relation

Sample (1)	Slope (2)	Intercept (3)
All Dwarfs	-0.65 ± 0.01	7.15 ± 0.10
ESLBGs Only	-0.86 ± 0.06	8.58 ± 0.36
UDGs Only	-0.66 ± 0.08	7.50 ± 0.61

Key to columns: (1) Combination of sub-samples used for the linear fits; (2) The slope of the fit in log-log space; (3) The intercept of the fit in log-log space.

comparable to UDGs, and the highest mass ESLBGs having lower T_N values than the average dwarf galaxy.

4.5 Discussion

In this section we will discuss the implications these results have on various fields of study for dwarf galaxy GCSs.

4.5.1 Implications for UDGs and ELSBGs

The properties of the GCSs of UDGs have been found to vary quite a bit, with many studies finding that UDGs can host extremely rich GC systems (Ferré-Mateu et al. 2023b; Gannon et al. 2024; Janssens et al. 2024; Forbes and Gannon 2024), or be GC-deficient for their masses (Jones et al. 2023; Buzzo et al. 2025a). While this catalog does not have sufficient data to investigate the question of what may drive this difference in GC-richness for UDGs, others have found that this may be related to formation pathways.

On average, UDGs with richer GC systems tend to be older, have lower metallicities, are found in denser environments like galaxy clusters, and have signs that their stellar populations formed early, quickly, and all at once throughout the galaxy (Jones et al. 2023; Ferré-Mateu et al. 2023b; Buzzo et al. 2025a; Ferré-Mateu et al. 2025). These could all be signs of a formation mechanism dependent on early tidal interactions or dwarf galaxy mergers which would "puff-up" a classical dwarf galaxy through tidal heating and also trigger a burst of GC formation (Ferré-Mateu et al. 2023b; Fielder et al. 2024).

While most UDGs found in galaxy clusters are associated with very early infall times, there exists no trend with GC-richness and time of infall (Forbes et al. 2023). However, this was only investigated by categorizing UDGs as either GC-rich, with $N_{GC} > 20$ or GC-poor, with $N_{GC} < 20$. As can be seen in Figure 4.2, some UDGs with $N_{GC} \sim 10$ could still be considered GC-rich for their stellar mass. It would be useful for the analysis of Forbes et al. 2023 to be re-conducted considering $N_{GC}/M_\star$ ratio, rather than simply N_{GC}.

Regardless, both GC-rich and GC-poor UDGs could still be formed via tidal heating and shocks due to cluster infall, but differ based on initial, internal galaxy properties that would encourage either GC formation and survival or GC destruction (Forbes et al. 2025). Gas and GC density prior to infall could be a contributing factor, as higher gas densities would encourage GC formation (Forbes et al. 2025), while higher densities in GC spatial distribution would encourage GC disruption from internal kinematics (Moreno-Hilario et al. 2024a).

This work indicates that similar mechanisms that produce GC-rich UDGs could potentially also produce the $N_{GC}/M_\star$ ratios and low surface-brightnesses seen in ELSBGs. This is similar to the work done by Saifollahi et al. 2025a, who also found that diffuse and low surface-brightness galaxies in the Perseus Cluster had systematically higher N_{GC} counts per unit stellar mass, similar to the UDGs studied in the same environment.

4.5.2 Dwarf Galaxy GCLFs

The GCLF is extremely important to consider in studies of dwarf galaxy GCSs. Not only is it used to estimate N_{GC} through completeness corrections, but its peak is also used to estimate average GC mass, and by extension total GCS mass for galaxies. However, due to the very low GC numbers hosted by dwarf galaxies, often it is not possible to construct an accurate GCLF for each individual galaxy. Instead, GCLFs are determined through stacking the GCS of a sample of dwarf galaxies. While on a whole this stacking yields a reasonable estimate of the average dwarf galaxy GCLF, the GCLFs of individual dwarf galaxies may vary from this average, sometimes significantly.

This was the method applied by Miller and Lotz 2007, Jordán et al. 2007, and Villegas et al. 2010 to obtain the GCLFs used by the surveys in this catalog. However, these studies used samples of dwarfs to construct their GCLFs which did not go to the lowest dwarf galaxy luminosities included in this combined catalog. The lowest galaxy magnitude bin in Miller and Lotz 2007 and Jordán et al. 2007 was $M_V \sim -13$, while the lowest magnitude bin in Villegas et al. 2010 was $M_V \sim -17.5$. More recently Saifollahi et al. 2025b determined the stacked dwarf GCLF in the Fornax cluster using a dwarf galaxy sample ranging from $-17 \lesssim M_V \lesssim -14$. For context, the magnitude range for the galaxies in this catalog span from $-21.4 \leq M_V \leq -9.4$.

Multiple studies have shown that both the peak magnitude and the dispersion in the GCLF can shift lower as a function of host galaxy luminosity (Jordán et al. 2007; Harris et al. 2013). As it currently stands, there is no broad study of the GCLF in galaxies with $M_V < -13$, of which nearly a third of this combined dwarf catalog would be classified. If the peak of the GCLF is actually at fainter magnitudes for these galaxies, it would mean that their N_{GC} values could be under-estimations, or that their M_{GCS} values could be over-estimations.

In addition, all studies of the GCLF of dwarfs has been limited to the Fornax and Virgo galaxy clusters. This is due to the large number of dwarfs at similar distances, all of which have been included in deep, high resolution surveys with HST and Euclid. However, this can also introduce an environmental bias, with the GCLF of dwarf galaxies in the Local Volume currently poorly studied.

4.5.3 A Present or Past Scaling Relation?

Finally, we would like to discuss the choice to have this scaling relation be dependent on peak halo mass rather than present halo mass. This choice immediately brings up the issue with comparing a past property of a galaxy (the highest halo mass hosted during its evolutionary history), against a present property (current GCS mass).

The linear $M_{GCS} - M_h$ scaling relation likely originated immediately after GCS formation, and the scatter we observe today is due to galaxy evolution mechanisms that have affected both dark matter halo and GCS masses (Choksi and Gnedin 2019). Ideally, we would also be able to plot "original" GCS mass alongside peak halo mass, but that is not currently possible. Through limiting one of these galaxy properties to what it would have been originally, we can better study the variations in GCS mass per unit halo mass that have since occurred in dwarf galaxies.

Several different theoretical studies of the $M_{GCS} - M_h$ relation have found that their fiducial models, where GC formation is limited to above a high gas surface density threshold, predict declining M_{GCS}/M_h ratios for dwarf galaxies, with the relation for dwarfs being steeper, and the galaxies themselves sitting lower, than is found in Figure 4.5 (El-Badry et al. 2019b; Choksi and Gnedin 2019; Valenzuela et al. 2021). However, allowing for more varied GC formation (El-Badry et al. 2019b), or accounting for GC formation via gas-rich galaxy mergers (Valenzuela et al. 2021) re-creates the larger spread in the $M_{GCS} - M_h$ relation for dwarfs that is observed, and recovers the continuation of linearity in the $M_{GCS} - M_h$ relation as well. While galaxy mergers have been shown to affect the scatter in this relation, less has been done to study the effect of tidal disruption.

By studying the $M_{GCS} - M_{peak}$ relation we can begin to form an observational understanding of the properties and evolutionary histories of dwarf galaxies which relate to the growth or destruction of the GCSs over time. This is turn can inform future studies of GCS evolution as a product of galaxy-galaxy interactions.

4.6 Summary

In this study we compiled a literature catalog of six systematic surveys of dwarf galaxy GCSs as well as a previous literature catalog encompassing various individual galaxy studies. For this combined catalog we determined both GCS masses and peak halo masses for each galaxy included using a consistent and standardized method to ensure that comparisons of these masses between surveys would be accurate. The result is the most complete, standardized study of the $M_{GCS} - M_h$ relation for the entire dwarf galaxy regime to date. We summarize the results of our analysis of this catalog below:

1. We find that for galaxies with stellar masses $M_\star \gtrsim 5 \times 10^9 M_\odot$ the linearity in the $M_{GCS} - M_h$ relation holds, with the majority of the increasing scatter compared to higher mass galaxies being driven by UDGs and ELSBGs.
2. When excluding BCGs, UDGs, and ELSBGs which we find to have systematically higher GC counts per unit mass, the slope of the $M_{GCS} - M_h$ relation is consistent from dwarf galaxies to massive galaxies up to $M_h \sim 10^{13} M_\odot$, taking on the form: $\log(M_{GCS}) = 0.95 \log(M_h) - 3.85$.
3. We found that, for dwarf galaxies, GC specific mass frequency (T_N) scales tightly with host galaxy stellar mass, with lower mass dwarfs having consistently higher T_N values.
4. We found that UDGs follow the same $T_N - M_\star$ relation as for classical dwarfs, but shifted to systematically higher T_N values. ESLBGs, on the other hand, follow a steeper $T_N - M_\star$

relation compared to classical dwarfs, with higher mass ESLBGs having lower T_N values than the average classical dwarf of the same stellar mass.

5. While the UDGs in our sample occupied a very wide range in GCS masses, galaxies with the highest T_N values for their stellar masses were exclusively UDGs, not classical dwarfs. In addition, the lowest mass ELSBGs had similar T_N values to UDGs, although having smaller effective radii. This implies that similar mechanisms that could also form GC-rich UDGs could also form low-mass ELSBGs.

4.7 Future Work

There are further steps required to expand and improve upon this dwarf galaxy GCS catalog in order to draw wider conclusions about what dictates where dwarf galaxies lie on the $M_{GCS} - M_h$ relation. Importantly, galaxies which host no GCs should be included to gain a fuller picture of the scatter observed in the scaling relation. This will also allow for the analysis of what galaxy properties are most closely correlated with a lack of GCs, as opposed to the GC-hosting dwarfs in this catalog currently.

In addition, more consistent data must be collected for global dwarf galaxy properties which could be indicators of the galaxies' GCS evolution histories, or of the galaxy's hospitality to GC formation and survival. Properties of note would be gas mass, gas surface density, and time of infall within their galaxy clusters. Systematic surveys, such as Euclid and LSST, could provide some of this data in the near future.

Chapter 5

Conclusions

Now we can begin to thread together the narrative told by this thesis, by looking back at where we began, seeing where we have arrived, and looking forward to where we will go next. As introduced in Chapter 1, while the connection between galaxy and GCS evolution has been well known, our understanding of how it affects the $M_{GCS} - M_h$ scaling relation has had observational gaps. The work presented here has filled in some of these gaps in the most extreme galaxy mass regimes.

While the extremely rich GCSs of BCGs have made them excellent laboratories for the study of GCS evolution, certain properties of these BCGs have made it difficult for them to be accurately compared to one another. First, these galaxies both have very large physical sizes and are very distant from us, with the closest BCG being M87 (D $\sim$ 16 Mpc). This results in deep, high-resolution, and wide-field imaging being necessary for precise GC photometry to be conducted, but the fields of view of which typically cannot include the entirety of the GCSs. Secondly, the clustered environments these BCGs reside in make defining the boundary between their own GCSs and the GCSs of their satellite galaxies or the intracluster medium difficult as well. The result of this has been a lack of studies of the GCSs of BCGs, and the studies that have been conducted suffer from a lack of uniformity in their methods.

In addition, GCS density profiles of BCGs, which are then integrated to obtain N_{GC} estimates, have been determined in the literature by dividing images into concentric annuli and estimating GC surface density for each annulus and plotting this against radius from the centre of the BCG. The drawbacks to this method were discussed in Chapter 2, and are particularly problematic for systems with high N_{GC} counts, like those hosted by BCGs. GCSs around BCGs also suffer from potential areas of GC overdensities, some associated with the BCG's GCS, tracing out substructures caused by mergers (Lim et al. 2017; Ennis et al. 2024), others not associated by the BCG's GCS, like the GCSs of nearby satellite galaxies.

Chapter 2 detailed a novel method to replace this annulus method for the determination not only of GCS radial density profiles, but the density profiles of any large system of discrete objects. While Voronoi tessellations have been applied to astronomical research before, including in cluster and void finding algorithms, and in creating moving meshes for magneto-hydrodynamical simulations, this was first time they have been applied to the determination of radial density profiles. We compared this Voronoi method to the traditional annulus method on a series of simulated GCSs, of varying sizes and steepnesses. We found that the Voronoi tessellations outperformed the annuli in both accuracy and precision, especially for the largest systems. We found that this was because the Voronoi tessellations provided very local density information compared to the annuli, which while being an excellent tool for identifying and removing GC overdensities caused by satellite galaxies, could result in more statistical noise for smaller systems. As a result, for systems with $N_{GC} \lesssim 2000$, Voronoi tessellations and annuli returned N_{GC} estimates within uncertainties of each other making their improvement only minimal for smaller systems, but most noticeable for very large systems.

The Voronoi tessellations also fared better than the annuli at accurately returning the radial density profiles of the steepest GCSs. Annuli, even small annuli, find it difficult to "keep up" with this high rate of change in the slope of the GC density profile at the innermost radii, resulting in under-estimates of the overall slope of the GCS, and by extension N_{GC}. The Voronoi tessellations on the other hand, with their higher spatial density resolution, are able to continue to return accurate estimates for both steep and shallow GCSs.

The necessity of this new method becomes readily apparent in Chapter 3, as it is applied to the GCSs of a sample of 27 BCGs. Firstly, the GCS radial density profiles of BCGs are very steep, with the majority of the systems in the sample having profiles steeper than what was simulated in Chapter 2. Thus, in order for the most accurate study of these observed BCGs' GCSs to be conducted the application of the Voronoi tessellation method was necessary. Eleven of the

27 BCGs included in the sample had their N_{GC} counts estimated using the annulus method in Dornan and Harris 2023, and it was found that those N_{GC} counts were higher for all 11 when determined using Voronoi tessellations (although still within uncertainties of the previous estimates).

Applying the Voronoi tessellation method to this sample of BCGs allowed for the highest mass end of the $M_{GCS} - M_h$ relation, spanning over a magnitude in halo mass, to be studied using consistent methodology. In addition to an accurate, standard determination of GCS radial density profiles, the determination of each galaxy's N_{GC} and M_{GCS} was also done consistently through a single definition of GCS size. Previous studies of BCGs used differing assumptions of GCS radius (R_{GCS}) to account for the limited field of view of their imaging, which prevented the bounds of the GCSs from being more accurately estimated. Chapter 3 applies a definition of R_{GCS} based on the virial radii (R_{vir}), which have previously been shown to scale with each other (Hudson and Robison 2018).

In addition, results of Chapter 3 also emphasized the need for accurate fits to the GCS radial density profiles of BCGs, as offset from the $M_{GCS} - M_h$ relation was found to most tightly correlate with the steepness of these profiles. For 16 of the 27 BCGs in the sample with colour information, it was found that this correlation was driven by the profiles of the red GCs, rather than the blue GCs. These red GCs were found to have systematically steeper profiles and were more centrally concentrated, properties of systems which the Voronoi tessellation method was found to better handle than the annulus method. Thus, the choice of determination method for radial density profiles is very important for the study of these GCSs.

This dependence of $M_{GCS} - M_h$ relation offset with red GC profile steepness, with more shallow profiles linked with higher GCS masses for the same halo mass, is suggested to be the result of the varying merger histories of the BCGs in the sample. Red GCs are more likely to have been formed in more metal-rich massive elliptical galaxies like BCGs, while blue GCs found in BCGs are more likely to have originally formed in smaller, more metal-poor satellite galaxies that have since been accreted onto the current BCG (Choksi and Gnedin 2019; Valenzuela et al. 2024). In addition, shallower, more extended GCS profiles can be indicators of major mergers, with the energy injected into the system from said merger capable of kicking the accreted GCs to higher galactic orbits (Chen and Gnedin 2023; Kluge and Bender 2023).

This paints a picture of major mergers between very massive, central ellipticals changing the distribution of the GCs in the resulting system, and pushing the final BCG up the $M_{GCS} - M_h$ relation, although positively offset in GCS mass. The answer to why exactly the growth in GCS mass outpaces that in halo mass from this major merger may lie in the one galaxy studied in Chapter 3 that did not follow this red GC steepness - relation offset trend. NGC 1129, although having the steepest red GC profile studied, was negatively offset from the $M_{GCS} - M_h$ relation, having a lower GCS mass for its halo mass than was average for the BCGs in the sample. If NGC 1129 was to follow the trend found in Chapter 3 it would be expected to be the *most positively offset* from $M_{GCS} - M_h$ relation, having a higher GCS mass for its halo mass than was average.

NGC 1129 is also the only galaxy in the sample to have obvious, visual indicators of having undergone a more recent major merger than the other BCGs studied. NGC 1129 has been found to have a boxy, twisted isophotal profile (Peletier et al. 1990; Goullaud et al. 2018; Ene et al. 2020), a twisted stellar kinematic profile to its major axis (Veale et al. 2017), and a double-core at its centre (Lyman et al. 2016). Combining the properties of this outlier with what was discussed in Sections 1.2.2 and 1.3.3, this could suggest that the timing of major mergers can also affect a galaxy's placement on the $M_{GCS} - M_h$ relation.

If these major mergers occurred at early enough times for the host galaxies to still have star-forming gas available ($z > 3$), they would have not only increased their GCSs through accretion, but also through a burst of GC formation. On the other hand, if perhaps NGC 1129 underwent a major merger after it had depleted its star-forming gas, it would not have been able to form any new GCs. Both its halo mass and GCS mass would have only been able to increase via accretion, and its GCS mass could have even decreased due to GC disruption, as was discussed in Section 1.2.3. The effects of mergers between massive elliptical galaxies with low gas mass fractions – referred to as "dry mergers", as opposed to their "wet" gas-rich counterparts – have been studied previously (Liu et al. 2009; Ennis et al. 2024), with the N-body simulations conducted by Shin and Kawata 2009 also finding that dry mergers can result in a flattening of red GC density profiles.

The results of Chapter 3 emphasize the role of galaxy-galaxy interactions in determining a galaxy's position on the $M_{GCS} - M_h$ relation. While the dominant processes for BCGs are major mergers, dwarf galaxies can be affected by a wide range of tidal interactions and offer an important opportunity to study smaller-scale GCS evolution. Both the shape and the scatter in the $M_{GCS} - M_h$ relation for dwarfs are not fully understood, partially due to a lack of complete, standardized data for low-mass galaxies.

Chapter 4 compiled a literature catalog of 366 galaxies with stellar masses below $M_\star \leq 2 \times 10^{10} M_\odot$ taken from six surveys and one previous literature catalog. To reduce scatter in the $M_{GCS} - M_h$ relation caused by differing methods to determine GCS and halo masses for these galaxies, these masses were determined for all catalog members using the same, standardized conversions from N_{GC} to M_{GCS} and from $M_\star$ to M_{peak}.

Crucially here we are not plotting the relation between current GCS mass and current halo mass, but rather current GCS mass and the highest halo mass hosted by the galaxies in their lifetimes (M_{peak}). This is because there is significant scatter in the stellar to halo mass relation for dwarf galaxies, but semi-analytical models have found that the stellar to peak halo mass relation is much tighter, allowing for a more reliable mass conversion. This distinction is not necessary for more massive galaxies like BCGs as their peak halo mass is equivalent to their current halo mass, as it has continuously grown through major mergers. Dwarf galaxies, on the other hand, can also have their halo masses decreased through tidal stripping. The degree to which dwarf galaxies are susceptible to having their dark matter halos stripped, however, is environmentally dependent. Christensen et al. 2024 found that, for their sample of simulated dwarf galaxies, the present-day SHMR was tighter and steeper for central or isolated dwarfs, with satellite dwarfs having lower halo masses for the same stellar mass.

We studied the positions of ultra diffuse galaxies (UDGs) on the $M_{GCS} - M_h$ relation and found that the UDGs included in our catalog were more likely to sit positively offset from the relation than their classical dwarf counterparts. We also found that extremely low surface brightness galaxies (ELSBGs) with surface brightnesses greater than $\langle \mu_{g,o} \rangle \geq 27$ mags/arcsec^2 (of any size) were also more likely to sit positively offset from the relation, although to a lesser extent than the UDGs. This implies that the same mechanisms that produce GC-rich UDGs could also be responsible for more compact dwarf galaxies with extremely low surface brightnesses.

While the formation mechanisms of UDGs are not fully understood at this point, with multiple formation pathways being likely as well, this result shows that mechanisms that can create the low-surface brightness and diffuse properties of these galaxies can also increase their GCS mass. One formation pathway proposed is that tidal heating caused by infall into galaxy clusters or dwarf-dwarf galaxy mergers can result in a "puffing up" of classical dwarfs (Ferré-Mateu et al. 2023b; Fielder et al. 2024). This formation mechanism, if having occurred early enough when the initial dwarf galaxy was still sufficiently gas-rich, could also result in a burst of GC formation, as was discussed in Section 1.2.2.

While the GCS density profiles of dwarf galaxies were not able to be studied in Chapter 4, these results are similar to those found in Chapter 3 with the BCGs: major, gas-rich galaxy mergers or tidal interactions have the capacity to push galaxies' GCS masses up, driving intrinsic scatter in the $M_{GCS} - M_h$ relation, in both extremes in host galaxy masses. We also find that there is still a somewhat large amount of variation in position on the relation for both BCGs and UDGs, showing that even for merger/interaction-rich galaxies differences in these evolutionary histories can be observed in their GCSs.

By standardizing our determination of masses for the dwarf galaxies in Chapter 4 using the same scaling relations applied to the BCG sample from Chapter 3, putting the data from both chapters together results in the most comprehensive, homogeneous observational study of the $M_{GCS} - M_h$ relation to date. This study spans six orders of magnitude in peak halo mass and encompasses the most extreme examples of galaxy morphology, including the least massive, extremely low surface brightness galaxies, to the most massive brightest cluster galaxies. This end-to-end observational definition of the relation, determined with a complete, up to date sample of GCSs, is the major result of this thesis. With this, we find that the linearity of the $M_{GCS} - M_h$ relation is indeed universal across all mass scales, from giant elliptical galaxies down to dwarf galaxies.

5.1 Future Work in The Field

The results of this thesis, as is typical of many scientific works, provide some answers and many more questions. While it is clear that mergers and tidal interactions between galaxies are driving the scatter in the $M_{GCS} - M_h$ relation, what specific types of physical processes play the largest role at different galaxy masses and/or environments needs to be further investigated. This can be probed by studying the ways in which multiple host galaxy and GCS properties are related to each other, including global metallicity, gas mass, GCS velocity dispersion, GCS spatial distribution, and GCS metallicity. Studying these properties in a systematic approach for a wide range of galaxy masses and environments will thus be necessary.

The recent launch of the Euclid Space Telescope and resulting survey mission will begin to provide much needed data for this research area. Euclid's Wide Field Survey will cover 15,000 square degrees in the sky, which will include 24,719 known galaxies within 100 Mpc (Euclid Collaboration et al. 2022) which will potentially host a combined $\sim 830,000$ GCs, $\sim 350,000$ of which would be photometrically detectable. Euclid will provide standardized imaging depth in visible and near-infrared filters for these GCs, many of which within 20 Mpc will be semi-resolved, allowing for extragalactic studies of GC structural parameters and light profiles (Euclid Collaboration et al. 2025).

Very recently, the Rubin Observatory saw first light and has begun the Legacy Survey of Space and Time (LSST). Rubin/LSST's Wide Fast Deep survey will cover 18,000 square degrees of the Southern sky, overlapping with the Euclid Wide Field Survey footprint (Usher et al. 2023; Dage et al. 2023). While Rubin's angular resolution will not be as high as Euclid, it will still be able to conduct reliable GC photometry for distances up to 10 Mpc, which will include several known GC-hosting Local Volume dwarf galaxies also included in the Euclid footprint (Usher et al. 2023).

The Roman Space Telescope is set to launch in 2027 and will conduct the High Latitude Wide Area Survey, covering 5,000 square degrees of the sky, half of which will include multiple filters and spectroscopy (Montes et al. 2023). Roman's angular resolution will be similar to Euclid's, allowing for GC photometry to be conducted out to distances of 100 Mpc. In addition, Roman is optimized for low surface brightness photometry, and will likely discover many new Local Volume dwarf galaxies and extragalactic tidal streams (Aganze et al. 2024). The ability to study both GC and stream populations in nearby dwarf galaxies will open up new opportunities for studies of extragalactic archaeology and GCS disruption.

Combining all three of these upcoming surveys will not only allow for a large, homogeneous study of GCSs spanning a variety of masses, but also environments. The vast majority of dwarf galaxies included in the sample presented in Chapter 4 reside in clustered environments, with few from groups or the field. Euclid, Rubin/LSST, and Roman will allow for GCSs of galaxies in the Local Volume and beyond to be more closely studied in order to constrain the role environment has on GCS evolution. This systematic expansion of dwarf galaxy GCS data will also allow for higher confidence confirmations of GC-free dwarf galaxies. By being able to study these non-GC-hosting galaxies more closely we will be able to understand what properties they have that would make them more susceptible to extreme GC disruption, or potentially would allow them to form without GCs to begin with.

In addition, Euclid's wide field of view will also be able to study the GCs on the outskirts of BCGs and in the intracluster medium. With a field of view covering 0.57 square degrees, Euclid's imaging will provide enough information for more sophisticated, statistical methods of GC membership to be developed. Rather than defining the GCS size of a BCG based on its virial radius, the probability of each GC belonging to the BCG, a satellite galaxy, or the intracluster medium can be determined. By being able to study the full GC population of galaxy clusters, both the GCSs of member galaxies and GCs within the intracluster medium, we will be able to accurately determine M_{GCS}/M_h ratios for galaxy clusters as a whole. With this, we can investigate if the largest structures in our universe adhere to or deviate from the $M_{GCS} - M_h$ relation, which we began to estimate in Chapter 3. Not only will these wide field telescopes allow for a better understanding of BCG and galaxy cluster GCSs, but it will also allow for the population of intracluster GCs to be studied more closely than ever before.

By being able to study the properties and distributions of GCs between galaxies in galaxy clusters we can begin to understand what the biggest factors are which contribute to the stripping of GCs from their original host galaxies. Topics of particular interest will be which galaxy masses/morphologies have contributed the most to the intracluster medium GC population, and on what timescales these GCs become stripped. Recent work has also highlighted the strength of GCs as tracers of dark matter distribution within galaxies (Kluge et al. 2023; Reina-Campos et al. 2023), raising the possibility of intracluster GCs to be used to trace dark matter distribution within massive galaxy clusters.

The evolutionary history of GCSs and their host galaxies are deeply linked, and evidence for this link can be found across galaxy mass and morphology. These GCSs, although having undergone profound changes in some cases, including bursts of formation, tidally induced destruction, and rapid periods of ex-situ GC accretion, continue to serve as excellent observational tracers of the evolutionary changes that they have undergone. As our observational capabilities to study the extremes of these GCSs and their host galaxies expand, so too will our understanding of the complexities of galaxy evolution which produce the wide variety of global galaxy properties we observe today.

Appendix A

Gannon Catalog Attributions

Here we list the galaxies from the Gannon et al. 2024 catalog which were included in our combined literature catalog presented in Chapter 4 and listed in Appendix B.

TABLE A1.1: Gannon Catalog Citations

Name	Citation
DF44	van Dokkum et al.(2016,2017, 2019), Gannon et al. 2021; Villaume et al. 2022; Webb et al. 2022; Saifollahi et al. 2022
DF07	van Dokkum et al. 2015a; Gu et al. 2018; Lim et al. 2018; Saifollahi et al. 2022; Ferré-Mateu et al. 2023a
DF17	Peng and Lim 2016; Beasley et al. 2016; van Dokkum et al. 2017; Gu et al. 2018; Saifollahi et al. 2022
DFX1	van Dokkum et al. 2017; Gannon et al. 2021; Saifollahi et al. 2022; Ferré-Mateu et al. 2023a
DGSAT-I	Martínez-Delgado et al. 2016; Martín-Navarro et al. 2019; Janssens et al. 2022
Hydra-I UDG 11	Iodice et al. 2020; Iodice et al. 2023
NGC 1052-DF2	van Dokkum et al. 2018; Fensch et al. 2019; Danieli et al. 2019; Shen et al. 2021; Shen et al. 2023
NGC 5846 UDG1	Forbes et al. 2019, Müller et al. (2020 2021), Forbes et al. 2021; Danieli et al. 2022; Ferré-Mateu et al. 2023a
NGVSUDG-19	Lim et al. 2020; Toloba et al. 2023
NGVSUDG-20	Lim et al. 2020; Toloba et al. 2023
Sag dSph	McConnachie 2012; Karachentsev et al. 2017; Forbes et al. 2018
VCC 1017	Lim et al. 2020; Toloba et al. 2023
VCC 1052	Lim et al. 2020; Toloba et al. 2023
VCC 1287	Beasley et al. 2016, Gannon et al. (2020, 2021), Lim et al. 2020; Toloba et al. 2023
VCC 615	Lim et al. 2020; Toloba et al. 2023
VCC 811	Lim et al. 2020; Toloba et al. 2023
VLSB-B	Toloba et al. 2018; Lim et al. 2020; Toloba et al. 2023
VLSB-D	Toloba et al. 2018; Lim et al. 2020; Toloba et al. 2023
WLM	McConnachie 2012; Forbes et al. 2018
Y358	van Dokkum et al. 2017; Lim et al. 2018; Gannon et al. 2023

Appendix B

Dwarf Galaxy Literature Catalog

Here we list the full dwarf galaxy literature catalog presented in Chapter 4.

Table A2.1: Dwarf Galaxy Literature Catalog

Name	Survey	$\log(M_\star)$	$\sigma_{\log(M_\star)}$	N_{GC}	$\sigma_{N_{GC}}$	M_V	Class
UGC8882	ELVES	7.8	7.2	3.1	1.6	0	reg
M101-DF1	ELVES	6.3	5.7	1.6	0.0	0	reg
dw1234p2531	ELVES	7.7	7.1	10.0	3.3	0	reg
dw1240p3216	ELVES	6.2	5.7	1.6	0.0	0	reg
KDG101	ELVES	7.7	7.2	6.3	3.1	0	reg
dw0932p2127	ELVES	7.9	7.3	3.3	1.7	0	reg
dw1906m6357	ELVES	7.5	6.9	10.5	3.5	0	reg
dw1312p4147	ELVES	8.1	7.6	9.7	4.8	0	reg
UGC05428	ELVES	7.5	7.0	4.7	3.1	0	reg
dw1122p1326	ELVES	8.5	7.9	16.2	3.2	0	reg
dw1119p1419	ELVES	7.6	7.1	11.9	4.4	0	reg
dw1119p1404	ELVES	7.7	7.2	14.4	1.7	0	reg
dw1050p1316	ELVES	8.4	7.9	15.5	5.0	0	reg
dw1048p1408	ELVES	8.3	7.8	6.8	3.4	0	reg
dw1051p1250	ELVES	7.9	7.3	4.9	3.3	0	reg

Continued on next page

Table A2.1

Continunued from previous page

Name	Survey	$\log(M_\star)$	$\sigma_{\log(M_\star)}$	N_{GC}	$\sigma_{N_{GC}}$	M_V	Class
dw1046p1401	ELVES	7.5	7.0	5.1	3.4	0	reg
dw1055p1220	ELVES	7.4	6.9	7.8	3.9	0	reg
dw1047p1248	ELVES	6.4	5.9	4.8	3.2	0	reg
dw1049p1233	ELVES	6.6	6.1	3.2	1.7	0	reg
dw1005m0744	ELVES	8.0	7.5	6.6	4.9	0	reg
dw1000m0821	ELVES	7.9	7.4	4.9	3.3	0	reg
dw1006m0730-n2	ELVES	6.4	5.9	4.9	1.6	0	reg
MATLAS-42	MATLAS	8.2	7.7	21.7	6.8	-15.62	UDG
MATLAS-49	MATLAS	7.9	7.4	1.2	2.0	-13.82	UDG
MATLAS-138	MATLAS	8.2	7.7	15.5	4.8	-14.56	UDG
MATLAS-262	MATLAS	7.2	6.7	3.3	3.2	-12.67	UDG
MATLAS-342	MATLAS	7.5	6.9	8.0	3.6	-14.27	UDG
MATLAS-401	MATLAS	7.9	7.4	13.2	4.4	-14.76	UDG
MATLAS-405	MATLAS	7.5	7.0	9.0	4.5	-13.67	UDG
MATLAS-585	MATLAS	7.3	6.8	10.5	4.1	-13.68	UDG
MATLAS-627	MATLAS	7.4	6.9	4.9	3.1	-13.46	UDG
MATLAS-799	MATLAS	8.2	7.7	16.4	5.5	-14.97	UDG
MATLAS-984	MATLAS	7.3	6.8	6.2	3.3	-13.64	UDG
MATLAS-1154	MATLAS	7.6	7.1	3.6	2.9	-13.37	UDG
MATLAS-1321	MATLAS	8.1	7.5	9.4	3.9	-14.67	UDG
MATLAS-1332	MATLAS	8.5	8.0	28.7	6.3	-15.52	UDG
MATLAS-1412	MATLAS	7.1	6.6	3.8	2.7	-13.32	UDG
MATLAS-1413	MATLAS	8.1	7.6	32.2	7.7	-14.68	UDG
MATLAS-1470	MATLAS	8.0	7.4	6.2	3.0	-14.42	UDG
MATLAS-1485	MATLAS	8.0	7.4	6.9	4.0	-13.59	UDG
MATLAS-1534	MATLAS	7.2	6.6	13.8	4.6	-13.02	UDG

Continued on next page

Table A2.1

Continunued from previous page

Name	Survey	$\log(M_\star)$	$\sigma_{\log(M_\star)}$	N_{GC}	$\sigma_{N_{GC}}$	M_V	Class
MATLAS-1589	MATLAS	7.1	6.6	6.0	3.5	-13.56	UDG
MATLAS-1616	MATLAS	7.8	7.3	11.2	4.6	-14.01	UDG
MATLAS-1779	MATLAS	7.7	7.1	11.4	5.4	-13.97	UDG
MATLAS-1865	MATLAS	7.1	6.6	7.7	3.5	-13.93	UDG
MATLAS-1938	MATLAS	8.6	8.1	28.5	5.7	-15.03	UDG
MATLAS-2019	MATLAS	8.1	7.5	37.6	6.8	-14.04	UDG
MATLAS-2176	MATLAS	7.7	7.2	9.1	3.5	-14.80	UDG
MATLAS-2184	MATLAS	6.7	6.1	6.8	3.4	-13.24	UDG
DF44	Gannon	8.5	8.0	74.0	18.0	-16.2	UDG
DF07	Gannon	8.6	8.1	23.0	7.0	-16.2	UDG
DF17	Gannon	8.4	7.9	27.0	4.0	-15.3	UDG
DFX1	Gannon	8.5	8.0	62.0	17.0	-15.8	UDG
DGSAT-I	Gannon	8.6	8.1	12.0	2.0	-16.3	UDG
Hydra-I UDG 11	Gannon	7.8	7.3	7.0	3.0	-14.62	UDG
NGC 1052-DF2	Gannon	8.3	7.8	7.1	4.3	-15.3	UDG
NGC 5846 UDG1	Gannon	8.0	7.5	54.0	9.0	-15	UDG
NGVSUDG-19	Gannon	7.8	7.3	16.8	7.5	-13.8	UDG
NGVSUDG-20	Gannon	7.1	6.6	11.3	8.6	-13.2	UDG
Sag dSph	Gannon	8.1	7.6	8.0	0.0	-15.5	UDG
VCC 1017	Gannon	8.5	8.0	16.5	11.2	-16.7	UDG
VCC 1052	Gannon	8.3	7.8	17.9	11.5	-15.2	UDG
VCC 1287	Gannon	8.3	7.8	22.0	8.0	-15.6	UDG
VCC 615	Gannon	7.9	7.3	30.3	9.6	-14.2	UDG
VCC 811	Gannon	7.9	7.3	15.8	8.4	-14.3	UDG
VLSB-B	Gannon	7.3	6.8	26.1	9.9	-12.3	UDG
VLSB-D	Gannon	7.8	7.2	13.0	6.9	-13.7	UDG

Continued on next page

Table A2.1

Continuned from previous page

Name	Survey	$\log(M_\star)$	$\sigma_{\log(M_\star)}$	N_{GC}	$\sigma_{N_{GC}}$	M_V	Class
WLM	Gannon	7.6	7.1	1.0	0.0	-14.25	UDG
Y358	Gannon	8.1	7.6	28.0	5.3	-14.8	UDG
D634-03	Georgiev	6.5	6.0	1.0	0.3	-11.94	reg
ESO269-66	Georgiev	7.5	7.0	4.0	1.2	-13.89	reg
ESO349-031	Georgiev	6.5	6.0	1.0	0.3	-11.87	reg
IKN	Georgiev	6.4	5.9	5.0	1.5	-11.51	reg
KK197	Georgiev	7.0	6.5	3.0	0.9	-13.04	reg
KK27	Georgiev	5.8	5.3	2.0	0.6	-10.14	reg
KKS55	Georgiev	6.2	5.7	1.0	0.3	-11.17	reg
UGC3974	Georgiev	7.9	7.4	4.0	1.2	-15.33	reg
UGC7369	Georgiev	8.2	7.7	22.0	6.6	-16.17	reg
UGC8638	Georgiev	7.2	6.7	3.0	0.9	-13.69	reg
LMC	Georgiev	9.2	8.7	16.0	4.8	-18.36	reg
DDO52	Georgiev	7.8	7.3	2.0	0.6	-14.98	reg
ESO059-01	Georgiev	7.7	7.2	1.0	0.3	-14.6	reg
ESO121-20	Georgiev	7.0	6.5	1.0	0.3	-13.64	reg
ESO137-18	Georgiev	8.8	8.3	7.0	2.1	-17.21	reg
ESO154-023	Georgiev	8.3	7.8	3.0	0.9	-16.38	reg
ESO223-09	Georgiev	8.4	7.8	8.0	2.4	-16.47	reg
ESO269-58	Georgiev	8.5	8.0	8.0	2.4	-15.78	reg
ESO274-01	Georgiev	9.2	8.7	10.0	3.0	-17.47	reg
ESO381-20	Georgiev	7.7	7.2	1.0	0.3	-14.8	reg
ESO384-016	Georgiev	7.3	6.7	2.0	0.6	-13.72	reg
IC1959	Georgiev	8.1	7.6	7.0	2.1	-15.99	reg
KK16	Georgiev	6.7	6.2	1.0	0.3	-12.38	reg
KK17	Georgiev	6.0	5.5	1.0	0.3	-10.57	reg

Continued on next page

Table A2.1

Continunued from previous page

Name	Survey	$\log(M_\star)$	$\sigma_{\log(M_\star)}$	N_{GC}	$\sigma_{N_{GC}}$	M_V	Class
KK246	Georgiev	7.0	6.5	2.0	0.6	-13.77	reg
KKH77	Georgiev	7.6	7.1	4.6	4.1	-14.58	reg
NGC1311	Georgiev	8.1	7.5	5.0	1.5	-15.76	reg
NGC247	Georgiev	9.4	8.8	25.0	7.5	-18.76	reg
NGC4163	Georgiev	7.3	6.8	2.0	0.6	-14.21	reg
NGC4605	Georgiev	9.2	8.7	22.0	6.6	-18.41	reg
NGC5237	Georgiev	8.2	7.7	3.0	0.9	-15.45	reg
NGC784	Georgiev	8.9	8.4	6.0	1.8	-16.87	reg
UGC1281	Georgiev	8.1	7.6	2.0	0.6	-15.3	reg
UGC3755	Georgiev	8.0	7.4	9.0	2.7	-15.5	reg
UGC4115	Georgiev	7.9	7.4	5.0	1.5	-15.12	reg
UGC685	Georgiev	7.5	7.0	5.0	1.5	-14.35	reg
UGC8760	Georgiev	7.0	6.5	1.0	0.3	-13.16	reg
UGCA86	Georgiev	8.2	7.7	11.0	3.3	-16.13	reg
UGCA92	Georgiev	7.7	7.1	2.0	0.6	-14.71	reg
NGC1427A	Georgiev	9.3	8.8	38.0	11.4	-18.5	reg
FDS10 LSB2	Fornax Deep	6.3	5.8	3.7	2.3	-11	reg
FDS10 LSB3	Fornax Deep	6.3	5.8	2.0	1.2	-9.8	ELSB
FDS10 LSB4	Fornax Deep	6.5	6.0	1.1	0.7	-11.7	reg
FDS10 LSB5	Fornax Deep	5.6	5.1	8.6	5.0	-11.1	ELSB
FDS10 LSB6	Fornax Deep	5.8	5.3	1.4	0.9	-10.4	reg
FDS10 LSB8	Fornax Deep	6.3	5.8	2.0	1.3	-11.3	reg
FDS10 LSB9	Fornax Deep	5.8	5.3	2.0	1.2	-9.9	reg
FDS10 LSB10	Fornax Deep	6.2	5.7	0.9	0.6	-11.3	reg
FDS10 LSB13	Fornax Deep	5.9	5.4	1.8	1.1	-10.2	reg
FDS10 LSB14	Fornax Deep	5.6	5.1	1.2	0.8	-11.1	reg

Continued on next page

Table A2.1

Continunued from previous page

Name	Survey	$\log(M_\star)$	$\sigma_{\log(M_\star)}$	N_{GC}	$\sigma_{N_{GC}}$	M_V	Class
FDS10 LSB15	Fornax Deep	6.5	6.0	2.2	1.3	-11.3	reg
FDS10 LSB16	Fornax Deep	6.1	5.6	1.5	0.9	-10.6	reg
FDS10 LSB23	Fornax Deep	6.7	6.2	2.3	1.5	-12.6	reg
FDS10 LSB25	Fornax Deep	7.6	7.1	5.7	3.7	-14.2	UDG
FDS10 LSB29	Fornax Deep	7.1	6.6	2.2	1.4	-13.4	reg
FDS10 LSB35	Fornax Deep	6.6	6.1	1.4	-0.6	-12.3	reg
FDS10 LSB38	Fornax Deep	6.5	6.0	2.8	1.6	-12	reg
FDS10 LSB40	Fornax Deep	6.1	5.6	6.1	3.1	-11	ELSB
FDS10 LSB41	Fornax Deep	6.8	6.3	2.3	1.5	-12.3	reg
FDS10 LSB43	Fornax Deep	6.2	5.7	0.9	0.6	-11.1	reg
FDS10 LSB44	Fornax Deep	6.3	5.8	1.7	0.9	-11.1	reg
FDS10 LSB45	Fornax Deep	6.7	6.2	1.7	1.1	-12.1	reg
FDS10 LSB46	Fornax Deep	5.9	5.4	1.4	0.9	-10.7	reg
FDS10 LSB49	Fornax Deep	6.8	6.3	1.7	1.1	-12.3	reg
FDS10 LSB51	Fornax Deep	6.8	6.3	2.6	1.7	-12.1	reg
FDS10 LSB52	Fornax Deep	7.4	6.9	4.7	2.7	-13.8	UDG
FDS10 LSB53	Fornax Deep	6.5	6.0	1.8	1.1	-11.5	reg
FDS10 LSB54	Fornax Deep	6.7	6.2	1.2	0.7	-9.7	reg
FDS10 LSB55	Fornax Deep	7.0	6.5	5.0	3.0	-12.4	reg
FDS10 LSB56	Fornax Deep	5.4	4.9	1.1	0.7	-9.7	reg
FDS11 LSB4	Fornax Deep	5.9	5.4	1.7	1.1	-11.2	reg
FDS11 LSB6	Fornax Deep	6.6	6.1	2.0	1.2	-10.3	reg
FDS11 LSB7	Fornax Deep	7.7	7.2	6.1	3.5	-10.8	UDG
FDS11 LSB8	Fornax Deep	6.2	5.7	1.5	1.0	-10.3	reg
FDS11 LSB10	Fornax Deep	6.5	6.0	2.1	1.2	-11.9	reg
FDS11 LSB11	Fornax Deep	6.3	5.8	2.6	1.7	-10.9	reg

Continued on next page

Table A2.1

Continunued from previous page

Name	Survey	$\log(M_\star)$	$\sigma_{\log(M_\star)}$	N_{GC}	$\sigma_{N_{GC}}$	M_V	Class
FDS11 LSB13	Fornax Deep	6.3	5.8	2.2	1.5	-11.1	reg
FDS11 LSB14	Fornax Deep	7.3	6.8	2.3	1.6	-11.8	reg
FDS11 LSB15	Fornax Deep	7.3	6.8	3.9	2.5	-12.3	reg
FDS11 LSB18	Fornax Deep	5.6	5.1	2.2	1.2	-10.9	reg
FDS11 LSB30	Fornax Deep	7.4	6.9	8.9	5.2	-13.7	UDG
FDS11 LSB35	Fornax Deep	6.0	5.5	3.8	2.3	-11.3	reg
FDS11 LSB36	Fornax Deep	6.1	5.6	2.3	1.5	-10.9	reg
FDS11 LSB38	Fornax Deep	8.0	7.5	29.8	9.2	-14.9	UDG
FDS11 LSB39	Fornax Deep	5.0	4.5	3.2	1.9	-10.2	ELSB
FDS11 LSB40	Fornax Deep	4.5	4.0	0.9	0.5	-9.5	reg
FDS11 LSB41	Fornax Deep	7.0	6.5	2.4	1.6	-13	reg
FDS11 LSB42	Fornax Deep	6.5	6.0	3.1	2.0	-12.1	reg
FDS11 LSB43	Fornax Deep	5.6	5.1	1.5	1.0	-9.8	reg
FDS11 LSB44	Fornax Deep	5.7	5.2	1.9	1.2	-10	reg
FDS11 LSB45	Fornax Deep	6.3	5.8	1.5	1.0	-11.4	reg
FDS11 LSB46	Fornax Deep	6.0	5.5	1.3	0.9	-10.9	ELSB
FDS11 LSB47	Fornax Deep	7.0	6.5	7.7	4.1	-13	reg
FDS11 LSB49	Fornax Deep	7.4	6.9	4.4	2.3	-13.7	reg
FDS11 LSB51	Fornax Deep	6.5	6.0	2.8	1.6	-10.3	ELSB
FDS11 LSB53	Fornax Deep	6.0	5.5	3.8	2.1	-10.8	reg
FDS11 LSB55	Fornax Deep	6.0	5.5	2.3	1.6	-11.4	reg
FDS11 LSB56	Fornax Deep	6.1	5.6	1.1	0.7	-11.2	reg
FDS11 LSB57	Fornax Deep	6.8	6.3	7.5	4.1	-12.3	reg
FDS11 LSB58	Fornax Deep	5.9	5.4	6.1	3.5	-11.2	reg
FDS11 LSB59	Fornax Deep	7.1	6.6	3.7	2.3	-13	reg
FDS11 LSB60	Fornax Deep	7.4	6.9	8.0	3.4	-13.8	reg

Continued on next page

Table A2.1

Continunued from previous page

Name	Survey	$\log(M_\star)$	$\sigma_{\log(M_\star)}$	N_{GC}	$\sigma_{N_{GC}}$	M_V	Class
FDS11 LSB61	Fornax Deep	6.6	6.1	2.7	1.7	-11.9	reg
FDS11 LSB62	Fornax Deep	7.7	7.2	3.4	2.3	-14.4	reg
FDS11 LSB63	Fornax Deep	6.0	5.5	2.1	1.3	-10.9	reg
FDS11 LSB64	Fornax Deep	6.2	5.7	1.7	1.1	-10.8	reg
FDS11 LSB65	Fornax Deep	6.7	6.2	8.0	4.2	-12.5	reg
FDS11 LSB66	Fornax Deep	6.3	5.8	1.3	0.9	-10.9	reg
FDS11 LSB67	Fornax Deep	6.4	5.9	5.0	3.0	-11.7	reg
FDS11 LSB68	Fornax Deep	6.4	5.9	3.7	2.3	-12.3	reg
FDS11 LSB69	Fornax Deep	6.9	6.4	6.2	3.6	-12.9	reg
FDS11 LSB71	Fornax Deep	6.0	5.5	1.2	0.8	-11.6	reg
FDS11 LSB72	Fornax Deep	6.5	6.0	2.0	1.2	-11.9	reg
FDS11 LSB73	Fornax Deep	5.1	4.6	1.7	1.1	-10.3	reg
FDS11 LSB74	Fornax Deep	7.3	6.8	4.0	2.5	-14	reg
FDS11 LSB76	Fornax Deep	5.9	5.4	1.3	0.9	-10.2	reg
FDS11 LSB77	Fornax Deep	7.0	6.5	1.2	0.8	-12.7	reg
FDS11 LSB78	Fornax Deep	7.6	7.1	5.2	3.3	-14.3	reg
FDS11 LSB79	Fornax Deep	6.8	6.3	2.3	1.3	-12.4	reg
FDS11 LSB80	Fornax Deep	6.8	6.3	2.0	1.3	-12.6	reg
FDS11 LSB81	Fornax Deep	7.1	6.6	5.8	3.0	-13.1	reg
FDS12 LSB3	Fornax Deep	7.3	6.8	3.4	2.3	-13.4	UDG
FDS12 LSB4	Fornax Deep	7.0	6.5	1.7	1.2	-13.2	reg
FDS12 LSB5	Fornax Deep	5.0	4.5	1.5	1.0	-9.9	reg
FDS12 LSB6	Fornax Deep	5.1	4.6	1.1	0.7	-9.4	ELSB
FDS12 LSB8	Fornax Deep	4.1	3.6	3.2	1.8	-10.5	reg
FDS12 LSB9	Fornax Deep	6.8	6.3	4.5	2.9	-13.4	reg
FDS12 LSB10	Fornax Deep	6.8	6.3	2.8	1.9	-13.5	reg

Continued on next page

Table A2.1

Continunued from previous page

Name	Survey	$\log(M_\star)$	$\sigma_{\log(M_\star)}$	N_{GC}	$\sigma_{N_{GC}}$	M_V	Class
FDS12 LSB11	Fornax Deep	6.5	6.0	2.1	1.4	-12.1	reg
FDS12 LSB12	Fornax Deep	5.9	5.4	3.4	2.3	-12.1	reg
FDS12 LSB13	Fornax Deep	6.8	6.3	4.7	3.1	-13.1	reg
FDS12 LSB14	Fornax Deep	5.7	5.2	1.0	0.6	-10.3	reg
FDS12 LSB16	Fornax Deep	6.1	5.6	2.4	1.6	-11.5	reg
FDS12 LSB17	Fornax Deep	6.1	5.6	1.6	1.1	-11.4	reg
FDS12 LSB19	Fornax Deep	5.4	4.9	1.6	1.0	-10.2	reg
FDS12 LSB20	Fornax Deep	6.5	6.0	5.2	3.3	-11.8	reg
FDS12 LSB21	Fornax Deep	6.7	6.2	6.0	3.3	-12.5	reg
FDS12 LSB22	Fornax Deep	6.7	6.2	1.5	1.0	-12.9	reg
FDS12 LSB23	Fornax Deep	6.0	5.5	1.7	1.2	-11.2	reg
FDS12 LSB24	Fornax Deep	6.8	6.3	1.6	1.1	-10.4	reg
FDS12 LSB25	Fornax Deep	3.5	3.0	1.5	0.9	-9.7	reg
FDS12 LSB26	Fornax Deep	6.3	5.8	2.3	1.4	-12.3	reg
FDS12 LSB28	Fornax Deep	6.0	5.5	3.5	2.1	-12.3	reg
FDS12 LSB29	Fornax Deep	6.6	6.1	5.3	3.2	-13	reg
FDS12 LSB30	Fornax Deep	7.7	7.2	10.9	7.0	-14.7	UDG
FDS12 LSB31	Fornax Deep	5.4	4.9	3.4	2.1	-10.2	ELSB
FDS12 LSB32	Fornax Deep	5.6	5.1	1.8	1.2	-10.7	reg
FDS12 LSB33	Fornax Deep	6.1	5.6	1.2	0.8	-11.2	reg
FDS12 LSB35	Fornax Deep	6.1	5.6	1.5	1.0	-11.5	reg
FDS12 LSB46	Fornax Deep	5.9	5.4	1.0	0.6	-11.1	reg
FDS12 LSB50	Fornax Deep	8.0	7.5	3.1	2.1	-15	UDG
FDS12 LSB52	Fornax Deep	6.2	5.7	3.1	2.0	-12.1	reg
FDS12 LSB53	Fornax Deep	7.0	6.5	2.1	1.4	-13.2	reg
FDS12 LSB54	Fornax Deep	6.6	6.1	3.4	2.1	-12.4	reg

Continued on next page

Table A2.1

Continuned from previous page

Name	Survey	$\log(M_\star)$	$\sigma_{\log(M_\star)}$	N_{GC}	$\sigma_{N_{GC}}$	M_V	Class
FDS16 LSB6	Fornax Deep	6.4	5.9	2.0	1.0	-12	reg
FDS16 LSB7	Fornax Deep	7.8	7.3	6.5	3.9	-14.7	reg
FDS16 LSB10	Fornax Deep	6.5	6.0	0.8	0.5	-11.9	reg
FDS16 LSB11	Fornax Deep	7.7	7.2	5.0	3.0	-14.4	reg
FDS16 LSB12	Fornax Deep	5.8	5.3	1.4	0.9	-10.3	reg
FDS16 LSB14	Fornax Deep	5.9	5.4	1.8	1.2	-10.1	reg
FDS16 LSB16	Fornax Deep	5.5	5.0	0.8	0.5	-9.9	reg
FDS16 LSB20	Fornax Deep	7.6	7.1	8.7	4.9	-14.4	reg
FDS16 LSB24	Fornax Deep	6.1	5.6	1.6	1.0	-11	reg
FDS16 LSB25	Fornax Deep	8.0	7.5	22.5	7.9	-15.1	reg
FDS16 LSB26	Fornax Deep	5.8	5.3	0.8	0.5	-9.9	reg
FDS16 LSB28	Fornax Deep	6.6	6.1	1.5	1.0	-11.9	reg
FDS16 LSB30	Fornax Deep	5.9	5.4	1.2	0.8	-10.4	reg
FDS16 LSB31	Fornax Deep	6.4	5.9	4.5	2.6	-11.4	UDG
FDS16 LSB32	Fornax Deep	6.8	6.3	2.8	1.6	-12.5	reg
FDS16 LSB33	Fornax Deep	6.7	6.2	1.8	1.0	-12.2	reg
FDS16 LSB34	Fornax Deep	6.9	6.4	3.0	1.9	-12.7	reg
FDS16 LSB35	Fornax Deep	6.5	6.0	3.3	2.0	-11.6	reg
FDS16 LSB36	Fornax Deep	7.1	6.6	2.7	1.7	-13.2	reg
FDS16 LSB37	Fornax Deep	6.8	6.3	3.1	1.8	-12.6	reg
FDS16 LSB38	Fornax Deep	7.0	6.5	4.2	2.7	-13.2	reg
FDS16 LSB39	Fornax Deep	5.9	5.4	2.8	1.6	-10.8	reg
FDS16 LSB40	Fornax Deep	6.3	5.8	4.5	2.5	-10.2	reg
FDS16 LSB41	Fornax Deep	6.4	5.9	0.9	0.6	-11.4	reg
FDS16 LSB42	Fornax Deep	6.8	6.3	1.8	1.2	-12.2	reg
FDS16 LSB43	Fornax Deep	7.6	7.1	6.5	3.6	-14.4	reg

Continued on next page

Table A2.1

Continuned from previous page

Name	Survey	$\log(M_\star)$	$\sigma_{\log(M_\star)}$	N_{GC}	$\sigma_{N_{GC}}$	M_V	Class
FDS16 LSB44	Fornax Deep	5.1	4.6	2.0	1.3	-10	ELSB
FDS16 LSB45	Fornax Deep	7.4	6.9	14.0	7.0	-13.6	UDG
FDS16 LSB47	Fornax Deep	6.2	5.7	3.3	2.1	-11.3	reg
FDS16 LSB49	Fornax Deep	5.9	5.4	2.5	1.6	-11.5	reg
FDS16 LSB50	Fornax Deep	7.0	6.5	2.1	1.4	-13.1	reg
FDS16 LSB52	Fornax Deep	6.0	5.5	1.0	0.7	-10.3	reg
FDS16 LSB54	Fornax Deep	5.7	5.2	1.4	0.9	-11.2	ELSB
FDS16 LSB55	Fornax Deep	6.8	6.3	2.7	1.7	-12.3	reg
FDS16 LSB56	Fornax Deep	11.6	11.1	0.7	0.5	-10.4	reg
FDS16 LSB58	Fornax Deep	8.0	7.5	4.5	2.7	-15.1	UDG
FDS16 LSB59	Fornax Deep	6.3	5.8	1.2	0.8	-10.9	reg
FDS16 LSB60	Fornax Deep	6.6	6.1	3.8	2.0	-11.6	ELSB
FDS16 LSB63	Fornax Deep	6.7	6.2	1.0	0.7	-11.9	reg
FDS16 LSB64	Fornax Deep	6.6	6.1	3.2	2.1	-12.3	reg
FDS16 LSB65	Fornax Deep	7.6	7.1	1.6	1.0	-10.3	reg
FDS16 LSB66	Fornax Deep	6.8	6.3	2.5	1.6	-11	ELSB
FDS16 LSB67	Fornax Deep	5.5	5.0	0.9	0.5	-10.2	reg
FDS16 LSB70	Fornax Deep	6.3	5.8	3.4	2.0	-11.7	reg
FDS16 LSB71	Fornax Deep	6.9	6.4	4.0	2.2	-12.7	reg
FDS16 LSB72	Fornax Deep	6.7	6.2	2.6	1.7	-12	reg
FDS16 LSB74	Fornax Deep	6.9	6.4	1.8	1.2	-12.4	reg
FDS16 LSB75	Fornax Deep	5.8	5.3	4.5	2.5	-10.8	reg
FDS16 LSB77	Fornax Deep	6.6	6.1	1.2	0.8	-12.1	reg
FDS16 LSB78	Fornax Deep	6.1	5.6	1.1	0.7	-10.8	reg
FDS16 LSB79	Fornax Deep	7.1	6.6	1.5	1.0	-12.6	reg
FDS16 LSB83	Fornax Deep	6.7	6.2	3.7	2.3	-12.5	reg

Continued on next page

Table A2.1

Continuned from previous page

Name	Survey	$\log(M_\star)$	$\sigma_{\log(M_\star)}$	N_{GC}	$\sigma_{N_{GC}}$	M_V	Class
FDS16 LSB84	Fornax Deep	6.8	6.3	3.2	2.1	-11.5	reg
FDS16 LSB85	Fornax Deep	8.1	7.6	4.3	2.8	-15.7	UDG
FDS16 LSB87	Fornax Deep	6.7	6.2	2.0	1.3	-12.6	reg
FDS11 LSB2	Fornax Deep	9.0	8.5	21.1	13.9	-15.4	UDG
FDS10 LSB27	Fornax Deep	7.8	7.3	3.0	2.0	-14.7	reg
FCC43	Virgo/Fornax	9.5	9.0	31.3	6.6	-18.94	reg
FCC335	Virgo/Fornax	9.1	8.6	9.9	3.6	-17.81	reg
FCC95	Virgo/Fornax	9.4	8.9	9.8	3.9	-17.9	reg
FCC136	Virgo/Fornax	9.3	8.8	16.4	4.6	-17.56	reg
FCC182	Virgo/Fornax	9.4	8.9	37.5	8.3	-17.71	reg
ESO358-43	Virgo/Fornax	9.3	8.7	12.0	4.2	-17.55	reg
FCC119	Virgo/Fornax	9.0	8.5	11.6	4.6	-17.21	reg
FCC26	Virgo/Fornax	8.4	7.9	14.8	4.3	-17.32	reg
FCC90	Virgo/Fornax	9.1	8.6	16.0	4.7	-17.44	reg
FCC106	Virgo/Fornax	9.2	8.6	10.5	4.5	-17.38	reg
FCC19	Virgo/Fornax	8.5	8.0	7.6	3.6	-16.89	reg
ESO358-56	Virgo/Fornax	8.8	8.3	13.1	5.0	-16.92	reg
ESO358-66	Virgo/Fornax	8.8	8.2	12.9	4.4	-16.9	reg
FCC100	Virgo/Fornax	8.9	8.4	23.6	5.7	-16.8	reg
ESO358-42	Virgo/Fornax	9.0	8.4	21.6	5.7	-16.97	reg
FCC303	Virgo/Fornax	8.7	8.2	12.8	4.2	-17.34	reg
VCC 355	Virgo/Fornax	10.2	9.6	100.0	31.0	-19.42	reg
VCC 1619	Virgo/Fornax	10.2	9.5	84.0	19.0	-19.36	reg
VCC 1883	Virgo/Fornax	10.2	9.6	83.0	25.0	-19.68	reg
VCC 1242	Virgo/Fornax	10.2	9.5	116.0	24.0	-19.38	reg
VCC 784	Virgo/Fornax	10.2	9.5	50.0	14.0	-19.31	reg

Continued on next page

Table A2.1

Continunued from previous page

Name	Survey	$\log(M_\star)$	$\sigma_{\log(M_\star)}$	N_{GC}	$\sigma_{N_{GC}}$	M_V	Class
VCC 1537	Virgo/Fornax	10.0	9.4	31.4	7.2	-18.99	reg
VCC 778	Virgo/Fornax	10.3	9.6	74.0	32.0	-19.56	reg
VCC 1321	Virgo/Fornax	9.8	9.2	31.0	9.0	-18.8	reg
VCC 828	Virgo/Fornax	10.1	9.5	69.5	9.8	-19.15	reg
VCC 1250	Virgo/Fornax	9.6	9.3	20.1	7.3	-18.98	reg
VCC 1630	Virgo/Fornax	10.1	9.4	47.0	11.0	-19.07	reg
VCC 1146	Virgo/Fornax	9.9	9.3	72.0	12.0	-18.93	reg
VCC 1025	Virgo/Fornax	10.3	9.6	141.0	34.0	-19.58	reg
VCC 1303	Virgo/Fornax	10.0	9.4	72.0	18.0	-18.84	reg
VCC 1913	Virgo/Fornax	10.0	9.4	71.0	14.0	-18.87	reg
VCC 1327	Virgo/Fornax	10.2	9.4	11.0	12.0	-19.1	reg
VCC 1125	Virgo/Fornax	9.9	9.5	52.3	8.5	-19.07	reg
VCC 1475	Virgo/Fornax	9.9	9.2	81.0	10.0	-18.56	reg
VCC 1178	Virgo/Fornax	9.9	9.2	25.3	9.2	-18.35	reg
VCC 1283	Virgo/Fornax	10.0	9.3	58.6	9.3	-18.65	reg
VCC 1261	Virgo/Fornax	9.7	9.2	35.1	7.6	-18.42	reg
VCC 698	Virgo/Fornax	10.0	9.4	114.0	12.0	-18.78	reg
VCC 1422	Virgo/Fornax	9.6	9.1	24.9	6.0	-17.97	reg
VCC 2048	Virgo/Fornax	9.5	9.0	17.2	5.4	-17.85	reg
VCC 1871	Virgo/Fornax	9.4	8.8	10.4	5.0	-17.31	reg
VCC 9	Virgo/Fornax	9.5	8.8	25.7	6.4	-18.04	reg
VCC 575	Virgo/Fornax	9.7	9.2	18.0	6.1	-18.42	reg
VCC 1910	Virgo/Fornax	9.3	8.9	48.7	8.4	-17.39	reg
VCC 1049	Virgo/Fornax	8.7	8.6	8.4	4.5	-16.69	reg
VCC 856	Virgo/Fornax	9.3	8.9	43.4	7.9	-17.57	reg
VCC 140	Virgo/Fornax	9.4	8.9	21.3	6.1	-17.51	reg

Continued on next page

Table A2.1

Continunued from previous page

Name	Survey	$\log(M_\star)$	$\sigma_{\log(M_\star)}$	N_{GC}	$\sigma_{N_{GC}}$	M_V	Class
VCC 1355	Virgo/Fornax	9.3	8.5	10.8	5.6	-17.51	reg
VCC 1087	Virgo/Fornax	9.5	9.0	66.0	9.5	-17.79	reg
VCC 1861	Virgo/Fornax	9.5	9.0	37.6	7.4	-17.6	reg
VCC 543	Virgo/Fornax	9.3	8.8	18.1	5.5	-17.41	reg
VCC 1431	Virgo/Fornax	9.3	8.9	60.6	9.3	-17.39	reg
VCC 1528	Virgo/Fornax	9.2	8.7	40.7	7.6	-17.16	reg
VCC 1695	Virgo/Fornax	9.2	8.9	14.4	5.7	-17.49	reg
VCC 1833	Virgo/Fornax	8.9	8.7	18.1	5.5	-17.13	reg
VCC 437	Virgo/Fornax	9.4	9.1	42.1	7.9	-17.82	reg
VCC 2019	Virgo/Fornax	9.0	8.9	23.9	6.1	-17.36	reg
VCC 200	Virgo/Fornax	9.1	8.7	15.5	5.8	-17.12	reg
VCC 571	Virgo/Fornax	9.0	8.8	10.9	5.6	-17.32	reg
VCC 21	Virgo/Fornax	8.7	8.6	20.7	6.5	-16.83	reg
VCC 1488	Virgo/Fornax	8.6	8.6	7.3	4.2	-16.78	reg
VCC 1895	Virgo/Fornax	8.9	8.6	6.3	4.3	-16.6	reg
VCC 1499	Virgo/Fornax	8.1	8.3	19.0	6.6	-16.53	reg
VCC 1545	Virgo/Fornax	9.1	8.6	54.2	8.8	-16.91	reg
VCC 1857	Virgo/Fornax	8.9	8.1	10.8	5.9	-16.64	reg
VCC 1075	Virgo/Fornax	9.0	8.7	16.5	5.2	-16.78	reg
VCC 1440	Virgo/Fornax	9.1	8.6	26.7	6.8	-16.86	reg
VCC 230	Virgo/Fornax	8.8	8.5	28.7	6.7	-16.21	reg
VCC 2050	Virgo/Fornax	8.5	8.4	9.2	4.3	-16.36	reg
VCC 751	Virgo/Fornax	9.1	8.7	9.2	4.3	-16.97	reg
VCC 1828	Virgo/Fornax	9.1	8.7	20.4	5.8	-16.78	reg
VCC 1407	Virgo/Fornax	9.1	8.6	49.7	8.6	-16.72	reg
VCC 1886	Virgo/Fornax	8.7	8.0	3.9	2.6	-16.25	reg

Continued on next page

Table A2.1

Continunued from previous page

Name	Survey	$\log(M_\star)$	$\sigma_{\log(M_\star)}$	N_{GC}	$\sigma_{N_{GC}}$	M_V	Class
VCC 1743	Virgo/Fornax	8.6	8.5	9.8	6.4	-16.33	reg
VCC 1539	Virgo/Fornax	8.7	8.0	31.0	7.0	-16.05	reg
VCC 1185	Virgo/Fornax	8.9	8.7	14.0	5.7	-16.77	reg
VCC 1826	Virgo/Fornax	8.8	8.3	4.5	3.9	-16.03	reg
VCC 1512	Virgo/Fornax	8.8	8.1	4.7	3.8	-16.25	reg
VCC 1489	Virgo/Fornax	8.5	7.8	11.7	4.8	-15.61	reg
VCC 1661	Virgo/Fornax	8.6	7.9	10.2	4.7	-15.81	reg

Bibliography

Adamo, A., Bradley, L. D., Vanzella, E., Claeyssens, A., Welch, B., Diego, J. M., Mahler, G., Oguri, M., Sharon, K., Abdurro'uf, Hsiao, T. Y.-Y., Xu, X., Messa, M., Lassen, A. E., Zackrisson, E., Brammer, G., Coe, D., Kokorev, V., Ricotti, M., Zitrin, A., Fujimoto, S., Inoue, A. K., Resseguier, T., Rigby, J. R., Jiménez-Teja, Y., Windhorst, R. A., Hashimoto, T., and Tamura, Y. (Aug. 2024). Bound star clusters observed in a lensed galaxy 460 Myr after the Big Bang. *Nature* 632(8025), 513–516.

Adamo, A., Usher, C., Pfeffer, J., and Claeyssens, A. (Oct. 2023). The ages and metallicities of the globular clusters in the Sparkler. *MNRAS* 525(1), L6–L10.

Aganze, C., Pearson, S., Starkenburg, T., Contardo, G., Johnston, K. V., Tavangar, K., Price-Whelan, A. M., and Burgasser, A. J. (Feb. 2024). Prospects for Detecting Gaps in Globular Cluster Stellar Streams in External Galaxies with the Nancy Grace Roman Space Telescope. *ApJ* 962(2) 151, 151.

Alamo-Martínez, K. A., Blakeslee, J. P., Jee, M. J., Côté, P., Ferrarese, L., González-Lópezlira, R. A., Jordán, A., Meurer, G. R., Peng, E. W., and West, M. J. (Sept. 2013). The Rich Globular Cluster System of Abell 1689 and the Radial Dependence of the Globular Cluster Formation Efficiency. *ApJ* 775(1) 20, 20.

Alavi, A., Siana, B., Richard, J., Rafelski, M., Jauzac, M., Limousin, M., Freeman, W. R., Scarlata, C., Robertson, B., Stark, D. P., Teplitz, H. I., and Desai, V. (Nov. 2016). The Evolution of the Faint End of the UV Luminosity Function during the Peak Epoch of Star Formation ($1 < z < 3$). *ApJ* 832(1) 56, 56.

Alfonso, J. and García-Varela, A. (Sept. 2023). A Gaia astrometric view of the open clusters Pleiades, Praesepe, and Blanco 1. *A&A* 677 A163, A163.

Ashman, K. M. and Zepf, S. E. (Jan. 1992). The Formation of Globular Clusters in Merging and Interacting Galaxies. *ApJ* 384, 50.

El-Badry, K., Quataert, E., Weisz, D. R., Choksi, N., and Boylan-Kolchin, M. (Feb. 2019a). The formation and hierarchical assembly of globular cluster populations. *MNRAS* 482(4), 4528–4552.

El-Badry, K., Quataert, E., Weisz, D. R., Choksi, N., and Boylan-Kolchin, M. (Feb. 2019b). The formation and hierarchical assembly of globular cluster populations. *MNRAS* 482(4), 4528–4552.

Baker, W. M., Maiolino, R., Belfiore, F., Bluck, A. F. L., Curti, M., Wylezalek, D., Bertemes, C., Bothwell, M. S., Lin, L., Thorp, M., and Pan, H.-A. (Jan. 2023). The molecular gas main sequence and Schmidt-Kennicutt relation are fundamental, the star-forming main sequence is a (useful) byproduct. *MNRAS* 518(3), 4767–4781.

Bastian, N., Pfeffer, J., Kruijssen, J. M. D., Crain, R. A., Trujillo-Gomez, S., and Reina-Campos, M. (Oct. 2020). The globular cluster system mass-halo mass relation in the E-MOSAICS simulations. *MNRAS* 498(1), 1050–1061.

Beasley, M. A. (2020). Globular Cluster Systems and Galaxy Formation. In: *Reviews in Frontiers of Modern Astrophysics; From Space Debris to Cosmology.* Ed. by P. Kabáth, D. Jones, and M. Skarka, 245–277.

Beasley, M. A., Romanowsky, A. J., Pota, V., Navarro, I. M., Martinez Delgado, D., Neyer, F., and Deich, A. L. (Mar. 2016). An Overmassive Dark Halo around an Ultra-diffuse Galaxy in the Virgo Cluster. *ApJL* 819(2) L20, L20.

Behroozi, P., Wechsler, R. H., Hearin, A. P., and Conroy, C. (Sept. 2019). UNIVERSEMACHINE: The correlation between galaxy growth and dark matter halo assembly from z = 0-10. *MNRAS* 488(3), 3143–3194.

Bell, E. F., McIntosh, D. H., Katz, N., and Weinberg, M. D. (Dec. 2003). The Optical and Near-Infrared Properties of Galaxies. I. Luminosity and Stellar Mass Functions. *ApJS* 149(2), 289–312.

Belokurov, V. and Kravtsov, A. (Nov. 2023). Nitrogen enrichment and clustered star formation at the dawn of the Galaxy. *MNRAS* 525(3), 4456–4473.

Belokurov, V. and Kravtsov, A. (Feb. 2024). In-situ versus accreted Milky Way globular clusters: a new classification method and implications for cluster formation. *MNRAS* 528(2), 3198–3216.

Belwal, K., Bisht, D., Bisht, M. S., Rangwal, G., Raj, A., Dattatrey, A. K., Yadav, R. K. S., and Bhatt, B. C. (May 2024). Exploring NGC 2345: A Comprehensive Study of a Young Open Cluster through Photometric and Kinematic Analysis. *AJ* 167(5) 188, 188.

Berek, S. C., Eadie, G. M., Speagle, J. S., and Wang, S. Y. (Sept. 2024). Should Zeros Count? Modeling the Galaxy–Globular Cluster Scaling Relation with(out) Zero-inflated Count Models. *ApJ* 972(1) 104, 104.

Bisht, D., Bisht, D., Raj, A., Rangwal, G., Sariya, D. P., and Manu, M. (July 2024). Berkeley 76: An intermediate age open star cluster in Gaia Era. *New Astron.* 109 102205, 102205.

Blakeslee, J. P. (Oct. 1999). Globular Clusters in Dense Clusters of Galaxies. *AJ* 118(4), 1506–1525.

Blakeslee, J. P., Tonry, J. L., and Metzger, M. R. (Aug. 1997). Globular Clusters in 19 Northern Abell Clusters. *AJ* 114, 482–506.

Blom, C., Forbes, D. A., Foster, C., Romanowsky, A. J., and Brodie, J. P. (Apr. 2014). The SLUGGS Survey: new evidence for a tidal interaction between the early-type galaxies NGC 4365 and NGC 4342. *MNRAS* 439(3), 2420–2431.

Bonaca, A., Naidu, R. P., Conroy, C., Caldwell, N., Cargile, P. A., Han, J. J., Johnson, B. D., Kruijssen, J. M. D., Myeong, G. C., Speagle, J. S., Ting, Y.-S., and Zaritsky, D. (Mar. 2021). Orbital Clustering Identifies the Origins of Galactic Stellar Streams. *ApJ* 909(2) L26, L26.

Boylan-Kolchin, M. (Dec. 2017). The globular cluster-dark matter halo connection. *MNRAS* 472(3), 3120–3130.

Brodie, J. P. and Strader, J. (Sept. 2006). Extragalactic Globular Clusters and Galaxy Formation. *ARA&A* 44(1), 193–267.

Bruzual, G. and Charlot, S. (Oct. 2003). Stellar population synthesis at the resolution of 2003. *MNRAS* 344(4), 1000–1028.

Burkert, A. and Forbes, D. A. (Feb. 2020). High-precision Dark Halo Virial Masses from Globular Cluster Numbers: Implications for Globular Cluster Formation and Galaxy Assembly. *AJ* 159(2) 56, 56.

Buzzo, M. L., Forbes, D. A., Jarrett, T. H., Marleau, F. R., Duc, P.-A., Brodie, J. P., Romanowsky, A. J., Ferré-Mateu, A., Hilker, M., Gannon, J. S., Pfeffer, J., and Haacke, L. (Jan.

2025a). The multiple classes of ultra-diffuse galaxies: can we tell them apart?. *MNRAS* 536(3), 2536–2557.

Buzzo, M. L., Forbes, D. A., Romanowsky, A. J., Haacke, L., Gannon, J. S., Tang, Y., Hilker, M., Ferré-Mateu, A., Janssens, S. R., Brodie, J. P., and Valenzuela, L. M. (Mar. 2025b). A new class of dark matter-free dwarf galaxies?: I. Clues from FCC 224, NGC 1052-DF2, and NGC 1052-DF4. *A&A* 695 A124, A124.

Callingham, T. M., Cautun, M., Deason, A. J., Frenk, C. S., Grand, R. J. J., and Marinacci, F. (July 2022). The chemo-dynamical groups of Galactic globular clusters. *MNRAS* 513(3), 4107–4129.

Capuzzo-Dolcetta, R. and Mastrobuono-Battisti, A. (Nov. 2009). Globular cluster system erosion in elliptical galaxies. *A&A* 507(1), 183–193.

Carlsten, S. G., Greene, J. E., Beaton, R. L., and Greco, J. P. (Mar. 2022). ELVES II: Globular Clusters and Nuclear Star Clusters of Dwarf Galaxies: the Importance of Environment. *ApJ* 927(1) 44, 44.

Caso, J. P., Ennis, A. I., and De Bórtoli, B. J. (Jan. 2024). Scaling relations for globular cluster systems in early-type galaxies - III. The inner flattening of the radial distributions. *MNRAS* 527(3), 6993–7004.

Catinella, B., Schiminovich, D., Kauffmann, G., Fabello, S., Wang, J., Hummels, C., Lemonias, J., Moran, S. M., Wu, R., Giovanelli, R., Haynes, M. P., Heckman, T. M., Basu-Zych, A. R., Blanton, M. R., Brinchmann, J., Budavári, T., Gonçalves, T., Johnson, B. D., Kennicutt, R. C., Madore, B. F., Martin, C. D., Rich, M. R., Tacconi, L. J., Thilker, D. A., Wild, V., and Wyder, T. K. (Apr. 2010). The GALEX Arecibo SDSS Survey - I. Gas fraction scaling relations of massive galaxies and first data release. *MNRAS* 403(2), 683–708.

Chen, Y. and Gnedin, O. Y. (July 2023). Formation of globular clusters in dwarf galaxies of the Local Group. *MNRAS* 522(4), 5638–5653.

Chen, Y. and Gnedin, O. Y. (Mar. 2024). Galaxy assembly revealed by globular clusters. *The Open Journal of Astrophysics* 7 23, 23.

Choksi, N. and Gnedin, O. Y. (Oct. 2019). Origins of scaling relations of globular cluster systems. *MNRAS* 488(4), 5409–5419.

Choksi, N., Gnedin, O. Y., and Li, H. (Oct. 2018). Formation of globular cluster systems: from dwarf galaxies to giants. *MNRAS* 480(2), 2343–2356.

Chow, G. C. (1960). Tests of Equality Between Sets of Coefficients in Two Linear Regressions. *Econometrica* 28(3), 591–605.

Christensen, C. R., Brooks, A. M., Munshi, F., Riggs, C., Van Nest, J., Akins, H., Quinn, T. R., and Chamberland, L. (Feb. 2024). Environment Matters: Predicted Differences in the Stellar Mass–Halo Mass Relation and History of Star Formation for Dwarf Galaxies. *ApJ* 961(2) 236, 236.

Chu, A., Durret, F., and Márquez, I. (May 2021). Physical properties of brightest cluster galaxies up to redshift 1.80 based on HST data. *A&A* 649 A42, A42.

Claeyssens, A., Adamo, A., Richard, J., Mahler, G., Messa, M., and Dessauges-Zavadsky, M. (Apr. 2023). Star formation at the smallest scales: a JWST study of the clump populations in SMACS0723. *MNRAS* 520(2), 2180–2203.

Collins, M. L. M. and Read, J. I. (May 2022). Observational constraints on stellar feedback in dwarf galaxies. *Nature Astronomy* 6, 647–658.

Contreras-Santos, A., Buitrago, F., Knebe, A., Rasia, E., Pearce, F. R., Cui, W., Power, C., and Winstanley, J. (Oct. 2024). The Three Hundred: The existence of massive dark matter-deficient satellite galaxies in cosmological simulations. *A&A* 690 A109, A109.

Côté, P., Marzke, R. O., and West, M. J. (July 1998). The Formation of Giant Elliptical Galaxies and Their Globular Cluster Systems. *ApJ* 501(2), 554–570.

Dage, K. C., Usher, C., Sobeck, J., Chies Santos, A. L., Szabó, R., Reina-Campos, M., Girardi, L., Ripepi, V., Di Criscienzo, M., Sarajedini, A., Clarkson, W., McGehee, P., Gizis, J., Rhode, K., Blakeslee, J., Cantiello, M., Theissen, C. A., Calamida, A., Ennis, A., Chamba, N., Gerasimov, R., Rich, R. M., Barmby, P., Ferguson, A. M. N., and Williams, B. F. (June 2023). Extragalactic Star Cluster Science with the Nancy Grace Roman Space Telescope's High Latitude Wide Area Survey and the Vera C. Rubin Observatory. *arXiv e-prints* arXiv:2306.12620, arXiv:2306.12620.

Dalal, R., Strauss, M. A., Sunayama, T., Oguri, M., Lin, Y.-T., Huang, S., Park, Y., and Takada, M. (Nov. 2021). Brightest cluster galaxies are statistically special from z = 0.3 to z = 1. *MNRAS* 507(3), 4016–4029.

Dalessandro, E., Ferraro, F. R., Massari, D., Lanzoni, B., Miocchi, P., and Beccari, G. (Sept. 2015). No Evidence of Mass Segregation in the Low-mass Galactic Globular Cluster NGC 6101. *ApJ* 810(1) 40, 40.

Danieli, S., Greene, J. E., Carlsten, S., Jiang, F., Beaton, R., and Goulding, A. D. (Oct. 2023a). ELVES. IV. The Satellite Stellar-to-halo Mass Relation Beyond the Milky Way. *ApJ* 956(1) 6, 6.

Danieli, S., Greene, J. E., Carlsten, S., Jiang, F., Beaton, R., and Goulding, A. D. (Oct. 2023b). ELVES. IV. The Satellite Stellar-to-halo Mass Relation Beyond the Milky Way. *ApJ* 956(1) 6, 6.

Danieli, S., van Dokkum, P., Conroy, C., Abraham, R., and Romanowsky, A. J. (Apr. 2019). Still Missing Dark Matter: KCWI High-resolution Stellar Kinematics of NGC1052-DF2. *ApJL* 874(2) L12, L12.

Danieli, S., van Dokkum, P., Trujillo-Gomez, S., Kruijssen, J. M. D., Romanowsky, A. J., Carlsten, S., Shen, Z., Li, J., Abraham, R., Brodie, J., Conroy, C., Gannon, J. S., and Greco, J. (Mar. 2022). NGC 5846-UDG1: A Galaxy Formed Mostly by Star Formation in Massive, Extremely Dense Clumps of Gas. *ApJL* 927(2) L28, L28.

de Boer, T. J. L., Gieles, M., Balbinot, E., Hénault-Brunet, V., Sollima, A., Watkins, L. L., and Claydon, I. (June 2019). Globular cluster number density profiles using Gaia DR2. *MNRAS* 485(4), 4906–4935.

De Lucia, G., Kruijssen, J. M. D., Trujillo-Gomez, S., Hirschmann, M., and Xie, L. (May 2024). On the origin of globular clusters in a hierarchical universe. *MNRAS* 530(3), 2760–2777.

Dehnen, W., Odenkirchen, M., Grebel, E. K., and Rix, H.-W. (May 2004). Modeling the Disruption of the Globular Cluster Palomar 5 by Galactic Tides. *AJ* 127(5), 2753–2770.

Dekel, A., Sari, R., and Ceverino, D. (Sept. 2009). Formation of Massive Galaxies at High Redshift: Cold Streams, Clumpy Disks, and Compact Spheroids. *ApJ* 703(1), 785–801.

Dolphin, A. E. (Oct. 2000). WFPC2 Stellar Photometry with HSTPHOT. *PASP* 112(776), 1383–1396.

Dornan, V. and Harris, W. E. (June 2023). Investigating the M $_{GCS}$-M $_{h}$ Relation in the Most Massive Galaxies. *ApJ* 950(2) 179, 179.

Dornan, V. and Harris, W. E. (Aug. 2024). Utilizing Voronoi Tessellations to Determine Radial Density Profiles. *AJ* 168(2) 48, 48.

Dornan, V. and Harris, W. E. (July 2025). Major Mergers Mean Major Offset: Drivers of Intrinsic Scatter in the $M_{GCS} - M_h$ Scaling Relation for Massive Elliptical Galaxies. *The Astrophysical Journal* 988(1), 70.

Durrell, P. R., Côté, P., Peng, E. W., Blakeslee, J. P., Ferrarese, L., Mihos, J. C., Puzia, T. H., Lançon, A., Liu, C., Zhang, H., Cuillandre, J.-C., McConnachie, A., Jordán, A., Accetta, K., Boissier, S., Boselli, A., Courteau, S., Duc, P.-A., Emsellem, E., Gwyn, S., Mei, S., and Taylor, J. E. (Oct. 2014). The Next Generation Virgo Cluster Survey. VIII. The Spatial Distribution of Globular Clusters in the Virgo Cluster. *ApJ* 794(2) 103, 103.

Eadie, G. M., Harris, W. E., and Springford, A. (Feb. 2022). Clearing the Hurdle: The Mass of Globular Cluster Systems as a Function of Host Galaxy Mass. *ApJ* 926(2) 162, 162.

Ene, I., Ma, C.-P., Walsh, J. L., Greene, J. E., Thomas, J., and Blakeslee, J. P. (Mar. 2020). The MASSIVE Survey XIV—Stellar Velocity Profiles and Kinematic Misalignments from 200 pc to 20 kpc in Massive Early-type Galaxies. *ApJ* 891(1) 65, 65.

Ennis, A. I., Caso, J. P., and Bassino, L. P. (Oct. 2024). Imprints of interaction processes in the globular cluster system of NGC 3640. *The Open Journal of Astrophysics* 7 93, 93.

Escudero, C. G., Cortesi, A., Faifer, F. R., Sesto, L. A., Smith Castelli, A. V., Johnston, E. J., Reynaldi, V., Chies-Santos, A. L., Salinas, R., Menéndez-Delmestre, K., Gonçalves, T. S., Grossi, M., and Mendes de Oliveira, C. (Mar. 2022). The complex globular cluster system of the S0 galaxy NGC 4382 in the outskirts of the Virgo Cluster. *MNRAS* 511(1), 393–412.

Euclid Collaboration et al. (June 2022). Euclid preparation. I. The Euclid Wide Survey. *A&A* 662 A112, A112.

Euclid Collaboration et al. (Jan. 2025). Euclid preparation: LVIII. Detecting extragalactic globular clusters in the Euclid survey. *A&A* 693 A251, A251.

Fahrion, K., Lyubenova, M., Hilker, M., van de Ven, G., Falcón-Barroso, J., Leaman, R., Martín-Navarro, I., Bittner, A., Coccato, L., Corsini, E. M., Gadotti, D. A., Iodice, E., McDermid, R. M., Pinna, F., Sarzi, M., Viaene, S., de Zeeuw, P. T., and Zhu, L. (May 2020a). The Fornax 3D project: Globular clusters tracing kinematics and metallicities. *A&A* 637 A26, A26.

Fahrion, K., Lyubenova, M., Hilker, M., van de Ven, G., Falcón-Barroso, J., Leaman, R., Martín-Navarro, I., Bittner, A., Coccato, L., Corsini, E. M., Gadotti, D. A., Iodice, E., McDermid, R. M., Pinna, F., Sarzi, M., Viaene, S., de Zeeuw, P. T., and Zhu, L. (May 2020b). The Fornax 3D project: Non-linear colour-metallicity relation of globular clusters. *A&A* 637 A27, A27.

Fall, S. M. and Rees, M. J. (Nov. 1985). A theory for the origin of globular clusters. *ApJ* 298, 18–26.

Fall, S. M., Chandar, R., and Whitmore, B. C. (Oct. 2009). New Tests for Disruption Mechanisms of Star Clusters: Methods and Application to the Antennae Galaxies. *ApJ* 704(1), 453–468.

Fall, S. M. and Zhang, Q. (Nov. 2001). Dynamical Evolution of the Mass Function of Globular Star Clusters. *ApJ* 561(2), 751–765.

Fassbender, R., Nastasi, A., Santos, J. S., Lidman, C., Verdugo, M., Koyama, Y., Rosati, P., Pierini, D., Padilla, N., Romeo, A. D., Menci, N., Bongiorno, A., Castellano, M., Cerulo, P., Fontana, A., Galametz, A., Grazian, A., Lamastra, A., Pentericci, L., Sommariva, V., Strazzullo, V., Šuhada, R., and Tozzi, P. (Aug. 2014). Galaxy population properties of the massive X-ray luminous galaxy cluster <ASTROBJ>XDCP J0044.0-2033</ASTROBJ> at z = 1.58. Red-sequence formation, massive galaxy assembly, and central star formation activity. *A&A* 568 A5, A5.

Federle, S., Gómez, M., Mieske, S., Harris, W. E., Hilker, M., Yegorova, I. A., and Harris, G. L. H. (Sept. 2024). The turbulent life of NGC 4696 as told by its globular cluster system. *A&A* 689 A342, A342.

Fensch, J., van der Burg, R. F. J., Jeřábková, T., Emsellem, E., Zanella, A., Agnello, A., Hilker, M., Müller, O., Rejkuba, M., Duc, P.-A., Durrell, P., Habas, R., Lim, S., Marleau, F. R., Peng, E. W., and Sánchez Janssen, R. (May 2019). The ultra-diffuse galaxy NGC 1052-DF2 with MUSE. II. The population of DF2: stars, clusters, and planetary nebulae. *A&A* 625 A77, A77.

Ferré-Mateu, A., Gannon, J., Forbes, D. A., Romanowsky, A. J., Buzzo, M. L., and Brodie, J. P. (Feb. 2025). Signs of 'Everything Everywhere All at Once' formation in low-surface-brightness globular-cluster-rich dwarf galaxies. *A&A* 694 L6, L6.

Ferré-Mateu, A., Gannon, J. S., Forbes, D. A., Buzzo, M. L., Romanowsky, A. J., and Brodie, J. (2023a). The star formation histories of quiescent ultra-diffuse galaxies and their dependence on environment and globular cluster richness. *MNRAS*.

Ferré-Mateu, A., Gannon, J. S., Forbes, D. A., Buzzo, M. L., Romanowsky, A. J., and Brodie, J. P. (Dec. 2023b). The star formation histories of quiescent ultra-diffuse galaxies and their dependence on environment and globular cluster richness. *MNRAS* 526(3), 4735–4754.

Fielder, C., Jones, M. G., Sand, D. J., Bennet, P., Crnojević, D., Karunakaran, A., Mutlu-Pakdil, B., and Spekkens, K. (Nov. 2024). All Puffed Up: Exploring Ultra-diffuse Galaxy Origins Through Galaxy Interactions. *AJ* 168(5) 212, 212.

Forbes, D. A. (Nov. 2017). How large are the globular cluster systems of early-type galaxies and do they scale with galaxy halo properties? *MNRAS* 472(1), L104–L108.

Forbes, D. A. (Mar. 2020). Reverse engineering the Milky Way. *MNRAS* 493(1), 847–854.

Forbes, D. A., Alabi, A., Romanowsky, A. J., Brodie, J. P., and Arimoto, N. (Mar. 2020). Globular clusters in Coma cluster ultra-diffuse galaxies (UDGs): evidence for two types of UDG? *MNRAS* 492(4), 4874–4883.

Forbes, D. A. and Bridges, T. (May 2010). Accreted versus in situ Milky Way globular clusters. *MNRAS* 404(3), 1203–1214.

Forbes, D. A., Buzzo, M. L., Ferre-Mateu, A., Romanowsky, A. J., Gannon, J., Brodie, J. P., and Collins, M. L. M. (Jan. 2025). Why do some ultra diffuse Galaxies have rich globular cluster systems? *MNRAS* 536(2), 1217–1225.

Forbes, D. A. and Gannon, J. (Feb. 2024). Do ultra diffuse galaxies with rich globular clusters systems have overly massive haloes? *MNRAS* 528(1), 608–619.

Forbes, D. A., Gannon, J., Couch, W. J., Iodice, E., Spavone, M., Cantiello, M., Napolitano, N., and Schipani, P. (June 2019). An ultra diffuse galaxy in the NGC 5846 group from the VEGAS survey. *A&A* 626 A66, A66.

Forbes, D. A., Gannon, J., Iodice, E., Hilker, M., Doll, G., Buttitta, C., Marca, A. L., Arnaboldi, M., Cantiello, M., D'Ago, G., Falcon Barroso, J., Greggio, L., Gullieuszik, M., Hartke, J., Mieske, S., Mirabile, M., Rampazzo, R., Rejkuba, M., Spavone, M., Spiniello, C., and Capasso, G. (Oct. 2023). Ultra diffuse galaxies in the Hydra I cluster from the LEWISProject: Phase-Space distribution and globular cluster richness. *MNRAS* 525(1), L93–L97.

Forbes, D. A., Gannon, J. S., Romanowsky, A. J., Alabi, A., Brodie, J. P., Couch, W. J., and Ferré-Mateu, A. (Jan. 2021). Stellar velocity dispersion and dynamical mass of the ultra diffuse galaxy NGC 5846_UDG1 from the keck cosmic web imager. *MNRAS* 500(1), 1279–1284.

Forbes, D. A., Read, J. I., Gieles, M., and Collins, M. L. M. (Dec. 2018). Extending the globular cluster system-halo mass relation to the lowest galaxy masses. *MNRAS* 481(4), 5592–5605.

Fujimoto, S., Ouchi, M., Kohno, K., Valentino, F., Gim\'enez-Arteaga, C., Brammer, G. B., Furtak, L. J., Kohandel, M., Oguri, M., Pallottini, A., Richard, J., Zitrin, A., Bauer, F. E., Boylan-Kolchin, M., Dessauges-Zavadsky, M., Egami, E., Finkelstein, S. L., Ma, Z., Smail, I., Watson, D., Hutchison, T. A., Rigby, J. R., Welch, B. D., Ao, Y., Bradley, L. D., Caminha, G. B., Caputi, K. I., Espada, D., Endsley, R., Fudamoto, Y., Gonz\'alez-L\'opez, J., Hatsukade, B., Koekemoer, A. M., Kokorev, V., Laporte, N., Lee, M., Magdis, G. E., Ono, Y., Rizzo, F., Shibuya, T., Shimasaku, K., Sun, F., Toft, S., Umehata, H., Wang, T., and Yajima, H. (Feb. 2024). Primordial Rotating Disk Composed of $\geq$15 Dense Star-Forming Clumps at Cosmic Dawn. *arXiv e-prints* arXiv:2402.18543, arXiv:2402.18543.

Gannon, J. S., Dullo, B. T., Forbes, D. A., Rich, R. M., Román, J., Couch, W. J., Brodie, J. P., Ferré-Mateu, A., Alabi, A., and Mould, J. (Apr. 2021). A photometric and kinematic analysis of UDG1137+16 (dw1137+16): Probing ultradiffuse galaxy formation in a group environment. *MNRAS* 502(3), 3144–3157.

Gannon, J. S., Ferré-Mateu, A., Forbes, D. A., Brodie, J. P., Buzzo, M. L., and Romanowsky, A. J. (June 2024). A Catalogue and analysis of ultra-diffuse galaxy spectroscopic properties. *MNRAS* 531(1), 1856–1869.

Gannon, J. S., Forbes, D. A., Brodie, J. P., Romanowsky, A. J., Couch, W. J., and Ferré-Mateu, A. (Jan. 2023). Keck spectroscopy of the coma cluster ultra-diffuse galaxy Y358: dynamical mass in a wider context. *MNRAS* 518(3), 3653–3666.

Gannon, J. S., Forbes, D. A., Romanowsky, A. J., Ferré-Mateu, A., Couch, W. J., and Brodie, J. P. (July 2020). On the stellar kinematics and mass of the Virgo ultradiffuse galaxy VCC 1287. *MNRAS* 495(3), 2582–2598.

Gannon, J. S., Forbes, D. A., Romanowsky, A. J., Ferré-Mateu, A., Couch, W. J., Brodie, J. P., Huang, S., Janssens, S. R., and Okabe, N. (Feb. 2022). Ultra-diffuse galaxies in the perseus cluster: comparing galaxy properties with globular cluster system richness. *MNRAS* 510(1), 946–958.

Garrison-Kimmel, S., Bullock, J. S., Boylan-Kolchin, M., and Bardwell, E. (Jan. 2017). Organized chaos: scatter in the relation between stellar mass and halo mass in small galaxies. *MNRAS* 464(3), 3108–3120.

Geisler, D., Lee, M. G., and Kim, E. (Apr. 1996). Washington Photometry of the Globular Cluster System of NGC 4472.I.Analysis of the Metallicities. *AJ* 111, 1529.

Georgiev, I. Y., Puzia, T. H., Goudfrooij, P., and Hilker, M. (Aug. 2010). Globular cluster systems in nearby dwarf galaxies - III. Formation efficiencies of old globular clusters. *MNRAS* 406(3), 1967–1984.

Gnedin, O. Y., Lee, H. M., and Ostriker, J. P. (Sept. 1999). Effects of Tidal Shocks on the Evolution of Globular Clusters. *ApJ* 522(2), 935–949.

Goullaud, C. F., Jensen, J. B., Blakeslee, J. P., Ma, C.-P., Greene, J. E., and Thomas, J. (Mar. 2018). The MASSIVE Survey. IX. Photometric Analysis of 35 High-mass Early-type Galaxies with HST WFC3/IR. *ApJ* 856(1) 11, 11.

Gu, M., Conroy, C., Law, D., van Dokkum, P., Yan, R., Wake, D., Bundy, K., Merritt, A., Abraham, R., Zhang, J., Bershady, M., Bizyaev, D., Brinkmann, J., Drory, N., Grabowski, K., Masters, K., Pan, K., Parejko, J., Weijmans, A.-M., and Zhang, K. (May 2018). Low Metallicities and Old Ages for Three Ultra-diffuse Galaxies in the Coma Cluster. *ApJ* 859(1) 37, 37.

Haacke, L., Forbes, D. A., Gannon, J. S., Danieli, S., Brodie, J. P., Pfeffer, J., Romanowsky, A. J., van Dokkum, P., Janssens, S. R., Buzzo, M. L., and Shen, Z. (May 2025). Investigating the Ultra-diffuse Galaxy NGC5846_UDG1 through the Kinematics of its Rich Globular Cluster System. *MNRAS* 539(2), 674–689.

Harris, W. E. and van den Bergh, S. (Nov. 1981). Globular clusters in galaxies beyond the local group. I. New cluster systems in selected northern ellipticals. *AJ* 86, 1627–1642.

Harris, W. E. (Oct. 1996). A Catalog of Parameters for Globular Clusters in the Milky Way. *AJ* 112, 1487.

Harris, W. E. (Mar. 2023). A Photometric Survey of Globular Cluster Systems in Brightest Cluster Galaxies. *ApJS* 265(1) 9, 9.

Harris, W. E., Blakeslee, J. P., Whitmore, B. C., Gnedin, O. Y., Geisler, D., and Rothberg, B. (Jan. 2016). Globular Cluster Systems in Brightest Cluster Galaxies. II. NGC 6166. *ApJ* 817(1) 58, 58.

Harris, W. E., Brown, R. A., Durrell, P. R., Romanowsky, A. J., Blakeslee, J., Brodie, J., Janssens, S., Lisker, T., Okamoto, S., and Wittmann, C. (Feb. 2020). The PIPER Survey. I. An Initial Look at the Intergalactic Globular Cluster Population in the Perseus Cluster. *ApJ* 890(2) 105, 105.

Harris, W. E., Ciccone, S. M., Eadie, G. M., Gnedin, O. Y., Geisler, D., Rothberg, B., and Bailin, J. (Jan. 2017). Globular Cluster Systems in Brightest Cluster Galaxies. III: Beyond Bimodality. *ApJ* 835(1) 101, 101.

Harris, W. E., Harris, G. L., and Hudson, M. J. (June 2015). Dark Matter Halos in Galaxies and Globular Cluster Populations. II. Metallicity and Morphology. *ApJ* 806(1) 36, 36.

Harris, W. E., Harris, G. L. H., and Alessi, M. (Aug. 2013). A Catalog of Globular Cluster Systems: What Determines the Size of a Galaxy's Globular Cluster Population? *ApJ* 772(2) 82, 82.

Harris, W. E., Morningstar, W., Gnedin, O. Y., O'Halloran, H., Blakeslee, J. P., Whitmore, B. C., Côté, P., Geisler, D., Peng, E. W., Bailin, J., Rothberg, B., Cockcroft, R., and Barber DeGraaff, R. (Dec. 2014). Globular Cluster Systems in Brightest Cluster Galaxies: A Near-universal Luminosity Function? *ApJ* 797(2) 128, 128.

Harris, W. E. and Mulholland, C. J. (Apr. 2017a). Detection of the Stellar Intracluster Medium in Perseus (Abell 426). *ApJ* 839(2) 102, 102.

Harris, W. E. and Mulholland, C. J. (Apr. 2017b). Detection of the Stellar Intracluster Medium in Perseus (Abell 426). *ApJ* 839(2) 102, 102.

Harris, W. E. and Pudritz, R. E. (July 1994). Supergiant Molecular Clouds and the Formation of Globular Cluster Systems. *ApJ* 429, 177.

Harris, W. E., Whitmore, B. C., Karakla, D., Okoń, W., Baum, W. A., Hanes, D. A., and Kavelaars, J. J. (Jan. 2006). Globular Cluster Systems in Brightest Cluster Galaxies: Bimodal Metallicity Distributions and the Nature of the High-Luminosity Clusters. *ApJ* 636(1), 90–114.

Hartman, K., Harris, W. E., Blakeslee, J. P., Ma, C.-P., and Greene, J. E. (Aug. 2023). Comparing Globular Cluster System Properties with Host Galaxy Environment. *ApJ* 953(2) 154, 154.

He, H., Wilson, C., Brunetti, N., Finn, M., Bemis, A., and Johnson, K. (Mar. 2022). Embedded Young Massive Star Clusters in the Antennae Merger. *ApJ* 928(1) 57, 57.

Herrera, C. N. and Boulanger, F. (Apr. 2017). The impact of a massive star cluster on its surrounding matter in the Antennae overlap region. *A&A* 600 A139, A139.

Hinshaw, G., Larson, D., Komatsu, E., Spergel, D. N., Bennett, C. L., Dunkley, J., Nolta, M. R., Halpern, M., Hill, R. S., Odegard, N., Page, L., Smith, K. M., Weiland, J. L., Gold, B., Jarosik, N., Kogut, A., Limon, M., Meyer, S. S., Tucker, G. S., Wollack, E., and Wright, E. L. (Oct. 2013). Nine-year Wilkinson Microwave Anisotropy Probe (WMAP) Observations: Cosmological Parameter Results. *ApJS* 208(2) 19, 19.

Howard, C. S., Pudritz, R. E., and Harris, W. E. (June 2018). A universal route for the formation of massive star clusters in giant molecular clouds. *Nature Astronomy* 2, 725–730.

Hudson, M. J., Gillis, B. R., Coupon, J., Hildebrandt, H., Erben, T., Heymans, C., Hoekstra, H., Kitching, T. D., Mellier, Y., Miller, L., Van Waerbeke, L., Bonnett, C., Fu, L., Kuijken, K., Rowe, B., Schrabback, T., Semboloni, E., van Uitert, E., and Velander, M. (Feb. 2015). CFHTLenS: co-evolution of galaxies and their dark matter haloes. *MNRAS* 447(1), 298–314.

Hudson, M. J., Harris, G. L., and Harris, W. E. (May 2014). Dark Matter Halos in Galaxies and Globular Cluster Populations. *ApJ* 787(1) L5, L5.

Hudson, M. J. and Robison, B. (July 2018). The correlation between the sizes of globular cluster systems and their host dark matter haloes. *MNRAS* 477(3), 3869–3885.

Hughes, M. E., Pfeffer, J. L., Bastian, N., Martig, M., Kruijssen, J. M. D., Crain, R. A., Reina-Campos, M., and Trujillo-Gomez, S. (Mar. 2022). The physics governing the upper truncation mass of the globular cluster mass function. *MNRAS* 510(4), 6190–6200.

Huxor, A. P., Ferguson, A. M. N., Tanvir, N. R., Irwin, M. J., Mackey, A. D., Ibata, R. A., Bridges, T., Chapman, S. C., and Lewis, G. F. (June 2011). Exploring the properties of the M31 halo globular cluster system. *MNRAS* 414(1), 770–780.

Icke, V. and van de Weygaert, R. (June 1991). The galaxy distribution as a Voronoi foam. *QJRAS* 32, 85–112.

Into, T. and Portinari, L. (Apr. 2013). New colour-mass-to-light relations: the role of the asymptotic giant branch phase and of interstellar dust. *MNRAS* 430(4), 2715–2731.

Iodice, E., Cantiello, M., Hilker, M., Rejkuba, M., Arnaboldi, M., Spavone, M., Greggio, L., Forbes, D. A., D'Ago, G., Mieske, S., Spiniello, C., La Marca, A., Rampazzo, R., Paolillo, M., Capaccioli, M., and Schipani, P. (Oct. 2020). The first detection of ultra-diffuse galaxies in the Hydra I cluster from the VEGAS survey. *A&A* 642 A48, A48.

Iodice, E., Hilker, M., Doll, G., Mirabile, M., Buttitta, C., Hartke, J., Mieske, S., Cantiello, M., D'Ago, G., Forbes, D. A., Gullieuszik, M., Rejkuba, M., Spavone, M., Spiniello, C., Arnaboldi, M., Corsini, E. M., Greggio, L., Falcón-Barroso, J., Fahrion, K., Fritz, J., La Marca, A., Paolillo, M., Raj, M. A., Rampazzo, R., Sarzi, M., and Capasso, G. (Aug. 2023). Looking into the faintEst WIth MUSE (LEWIS): on the nature of ultra-diffuse galaxies in the Hydra-I cluster.I. Project description and preliminary results. *arXiv e-prints* arXiv:2308.11493, arXiv:2308.11493.

Janssens, S. R., Forbes, D. A., Romanowsky, A. J., Gannon, J., Pfeffer, J., Couch, W. J., Brodie, J. P., Harris, W. E., Durrell, P. R., and Bekki, K. (Oct. 2024). The PIPER survey. II. The globular cluster systems of low surface brightness galaxies in the Perseus cluster. *MNRAS* 534(1), 783–799.

Janssens, S. R., Romanowsky, A. J., Abraham, R., Brodie, J. P., Couch, W. J., Forbes, D. A., Laine, S., Martínez-Delgado, D., and van Dokkum, P. G. (Nov. 2022). The globular clusters and star formation history of the isolated, quiescent ultra-diffuse galaxy DGSAT I. *MNRAS* 517(1), 858–871.

Jarai-Szabo, F. and Neda, Z. (June 2004). On the size-distribution of Poisson Voronoi cells. *arXiv e-prints* cond-mat/0406116, cond–mat/0406116.

Johansson, P. H., Naab, T., and Ostriker, J. P. (May 2009). Gravitational Heating Helps Make Massive Galaxies Red and Dead. *ApJ* 697(1), L38–L43.

Jones, M. G., Karunakaran, A., Bennet, P., Sand, D. J., Spekkens, K., Mutlu-Pakdil, B., Crnojević, D., Janowiecki, S., Leisman, L., and Fielder, C. E. (Jan. 2023). Gas-rich, Field Ultra-diffuse Galaxies Host Few Globular Clusters. *ApJ* 942(1) L5, L5.

Jordán, A., McLaughlin, D. E., Côté, P., Ferrarese, L., Peng, E. W., Mei, S., Villegas, D., Merritt, D., Tonry, J. L., and West, M. J. (July 2007). The ACS Virgo Cluster Survey. XII. The Luminosity Function of Globular Clusters in Early-Type Galaxies. *ApJS* 171(1), 101–145.

Joschko, P. S., Kruijssen, J. M. D., Trujillo-Gomez, S., Pfeffer, J. L., Bastian, N., Crain, R. A., and Reina-Campos, M. (Dec. 2024). The cosmic globular cluster formation history in the E-MOSAICS simulations. *arXiv e-prints* arXiv:2412.04105, arXiv:2412.04105.

Karachentsev, I. D., Makarova, L. N., Sharina, M. E., and Karachentseva, V. E. (Oct. 2017). KDG218, a nearby ultra-diffuse galaxy. *Astrophysical Bulletin* 72(4), 376–383.

Katz, H. and Ricotti, M. (Nov. 2014). Clues on the missing sources of reionization from self-consistent modelling of Milky Way and dwarf galaxy globular clusters. *MNRAS* 444(3), 2377–2395.

Keller, B. W., Kruijssen, J. M. D., Pfeffer, J., Reina-Campos, M., Bastian, N., Trujillo-Gomez, S., Hughes, M. E., and Crain, R. A. (July 2020). Where did the globular clusters of the Milky Way form? Insights from the E-MOSAICS simulations. *MNRAS* 495(4), 4248–4267.

King, I. R. (May 1966). The structure of star clusters. IV. Photoelectric surface photometry in nine globular clusters. *AJ* 71, 276.

Kluge, M. and Bender, R. (Aug. 2023). Minor Mergers Are Not Enough: The Importance of Major Mergers during Brightest Cluster Galaxy Assembly. *ApJS* 267(2) 41, 41.

Kluge, M., Remus, R.-S., Babyk, I. V., Forbes, D. A., and Dolfi, A. (June 2023). A trail of the invisible: blue globular clusters trace the radial density distribution of the dark matter - case study of NGC 4278. *MNRAS* 521(4), 4852–4862.

Knödlseder, J. (Aug. 2000). Cygnus OB2 - a young globular cluster in the Milky Way. *A&A* 360, 539–548.

Koudmani, S., Sijacki, D., and Smith, M. C. (Oct. 2022). Two can play at that game: constraining the role of supernova and AGN feedback in dwarf galaxies with cosmological zoom-in simulations. *MNRAS* 516(2), 2112–2141.

Krause, M., Charbonnel, C., Decressin, T., Meynet, G., Prantzos, N., and Diehl, R. (Oct. 2012). Superbubble dynamics in globular cluster infancy. I. How do globular clusters first lose their cold gas? *A&A* 546 L5, L5.

Kravtsov, A. and Winney, S. (June 2024). Effect of the Large Magellanic Cloud on the kinematics of Milky Way satellites and virial mass estimate. *The Open Journal of Astrophysics* 7 50, 50.

Kravtsov, A. V. and Gnedin, O. Y. (Apr. 2005). Formation of Globular Clusters in Hierarchical Cosmology. *ApJ* 623(2), 650–665.

Kruijssen, J. M. D. (Dec. 2015). Globular clusters as the relics of regular star formation in 'normal' high-redshift galaxies. *MNRAS* 454(2), 1658–1686.

Kruijssen, J. M. D. (Jan. 2025). The Formation of Globular Clusters. *arXiv e-prints* arXiv:2501.16438, arXiv:2501.16438.

Kruijssen, J. M. D., Pelupessy, F. I., Lamers, H. J. G. L. M., Portegies Zwart, S. F., Bastian, N., and Icke, V. (Apr. 2012). Formation versus destruction: the evolution of the star cluster population in galaxy mergers. *MNRAS* 421(3), 1927–1941.

Kruijssen, J. M. D., Pelupessy, F. I., Lamers, H. J. G. L. M., Portegies Zwart, S. F., and Icke, V. (June 2011). Modelling the formation and evolution of star cluster populations in galaxy simulations. *MNRAS* 414(2), 1339–1364.

Kruijssen, J. M. D., Pfeffer, J. L., Chevance, M., Bonaca, A., Trujillo-Gomez, S., Bastian, N., Reina-Campos, M., Crain, R. A., and Hughes, M. E. (Oct. 2020). Kraken reveals itself - the merger history of the Milky Way reconstructed with the E-MOSAICS simulations. *MNRAS* 498(2), 2472–2491.

Lahén, N., Naab, T., Johansson, P. H., Elmegreen, B., Hu, C.-Y., and Walch, S. (July 2019). The Formation of Low-metallicity Globular Clusters in Dwarf Galaxy Mergers. *ApJ* 879(2) L18, L18.

Lahén, N., Naab, T., and Kauffmann, G. (Aug. 2022). A panchromatic view of star cluster formation in a simulated dwarf galaxy starburst. *MNRAS* 514(3), 4560–4580.

Lahén, N., Rantala, A., Naab, T., Partmann, C., Johansson, P. H., and Hislop, J. M. (Apr. 2025). The formation, evolution, and disruption of star clusters with improved gravitational dynamics in simulated dwarf galaxies. *MNRAS* 538(3), 2129–2148.

Le, M. N. and Cooper, A. P. (Jan. 2025). Globular Cluster Counts around 700 Nearby Galaxies. *ApJ* 978(1) 33, 33.

Leaman, R., VandenBerg, D. A., and Mendel, J. T. (Nov. 2013). The bifurcated age-metallicity relation of Milky Way globular clusters and its implications for the accretion history of the galaxy. *MNRAS* 436(1), 122–135.

Li, D., Eadie, G., Brown, P., Harris, W., Abraham, R., van Dokkum, P., Janssens, S., Berek, S., Danieli, S., Romanowsky, A., and Speagle, J. (Sept. 2024). Discovery of Two Ultra-Diffuse Galaxies with Unusually Bright Globular Cluster Luminosity Functions via a Mark-Dependently Thinned Point Process (MATHPOP). *arXiv e-prints* arXiv:2409.06040, arXiv:2409.06040.

Li, H. and Gnedin, O. Y. (Nov. 2014). Modeling the Formation of Globular Cluster Systems in the Virgo Cluster. *ApJ* 796(1) 10, 10.

Li, H. and Gnedin, O. Y. (July 2019). Star cluster formation in cosmological simulations - III. Dynamical and chemical evolution. *MNRAS* 486(3), 4030–4043.

Li, H., Vogelsberger, M., Bryan, G. L., Marinacci, F., Sales, L. V., and Torrey, P. (July 2022). Formation and evolution of young massive clusters in galaxy mergers: the SMUGGLE view. *MNRAS* 514(1), 265–279.

Li, Y., Mac Low, M.-M., and Klessen, R. S. (Oct. 2004). Formation of Globular Clusters in Galaxy Mergers. *ApJ* 614(1), L29–L32.

Lim, S., Côté, P., Peng, E. W., Ferrarese, L., Roediger, J. C., Durrell, P. R., Mihos, J. C., Wang, K., Gwyn, S. D. J., Cuillandre, J.-C., Liu, C., Sánchez-Janssen, R., Toloba, E., Sales, L. V., Guhathakurta, P., Lançon, A., and Puzia, T. H. (Aug. 2020). The Next Generation Virgo Cluster Survey (NGVS). XXX. Ultra-diffuse Galaxies and Their Globular Cluster Systems. *ApJ* 899(1) 69, 69.

Lim, S., Peng, E. W., Côté, P., Ferrarese, L., Roediger, J. C., Liu, C., Spengler, C., Sola, E., Duc, P.-A., Sales, L. V., Blakeslee, J. P., Cuillandre, J.-C., Durrell, P. R., Emsellem, E., Gwyn, S. D. J., Lançon, A., Marleau, F. R., Mihos, J. C., Müller, O., Puzia, T. H., and Sánchez-Janssen, R. (May 2024). The Next Generation Virgo Cluster Survey (NGVS). XXVII. The Size and Structure of Globular Cluster Systems and Their Connection to Dark Matter Halos. *ApJ* 966(2) 168, 168.

Lim, S., Peng, E. W., Côté, P., Sales, L. V., den Brok, M., Blakeslee, J. P., and Guhathakurta, P. (July 2018). The Globular Cluster Systems of Ultra-diffuse Galaxies in the Coma Cluster. *ApJ* 862(1) 82, 82.

Lim, S., Peng, E. W., Duc, P.-A., Fensch, J., Durrell, P. R., Harris, W. E., Cuillandre, J.-C., Gwyn, S., Lançon, A., and Sánchez-Janssen, R. (Feb. 2017). Globular Clusters as Tracers of Fine Structure in the Dramatic Shell Galaxy NGC 474. *ApJ* 835(2) 123, 123.

Limberg, G., Souza, S. O., Pérez-Villegas, A., Rossi, S., Perottoni, H. D., and Santucci, R. M. (Aug. 2022). Reconstructing the Disrupted Dwarf Galaxy Gaia-Sausage/Enceladus Using Its Stars and Globular Clusters. *ApJ* 935(2) 109, 109.

Liu, F. S., Mao, S., Deng, Z. G., Xia, X. Y., and Wen, Z. L. (July 2009). Major dry mergers in early-type brightest cluster galaxies. *MNRAS* 396(4), 2003–2010.

Liu, Y., Peng, E. W., Jordán, A., Blakeslee, J. P., Côté, P., Ferrarese, L., and Puzia, T. H. (Apr. 2019). The ACS Fornax Cluster Survey. III. Globular Cluster Specific Frequencies of Early-type Galaxies. *ApJ* 875(2) 156, 156.

Lomelí-Núñez, L., Mayya, Y. D., Rodríguez-Merino, L. H., Ovando, P. A., and Rosa-González, D. (Jan. 2022). Luminosity functions of globular clusters in five nearby spiral galaxies using HST/ACS images. *MNRAS* 509(1), 180–201.

Lyman, J. D., Levan, A. J., James, P. A., Angus, C. R., Church, R. P., Davies, M. B., and Tanvir, N. R. (May 2016). Hubble Space Telescope observations of the host galaxies and environments of calcium-rich supernovae. *MNRAS* 458(2), 1768–1777.

Madau, P., Lupi, A., Diemand, J., Burkert, A., and Lin, D. N. C. (Feb. 2020). Globular Cluster Formation from Colliding Substructure. *ApJ* 890(1) 18, 18.

Madrid, J. P., O'Neill, C. R., Gagliano, A. T., and Marvil, J. R. (Nov. 2018). A Wide-field Map of Intracluster Globular Clusters in Coma. *ApJ* 867(2) 144, 144.

Maji, M., Zhu, Q., Li, Y., Charlton, J., Hernquist, L., and Knebe, A. (Aug. 2017). The Formation and Evolution of Star Clusters in Interacting Galaxies. *ApJ* 844(2) 108, 108.

Malhan, K., Ibata, R. A., Sharma, S., Famaey, B., Bellazzini, M., Carlberg, R. G., D'Souza, R., Yuan, Z., Martin, N. F., and Thomas, G. F. (Feb. 2022). The Global Dynamical Atlas of the Milky Way Mergers: Constraints from Gaia EDR3-based Orbits of Globular Clusters, Stellar Streams, and Satellite Galaxies. *ApJ* 926(2) 107, 107.

Manwadkar, V. and Kravtsov, A. V. (Nov. 2022). Forward-modelling the luminosity, distance, and size distributions of the Milky Way satellites. *MNRAS* 516(3), 3944–3971.

Marleau, F. R., Duc, P.-A., Poulain, M., Müller, O., Lim, S., Durrell, P. R., Habas, R., Sánchez-Janssen, R., Paudel, S., and Fensch, J. (Oct. 2024). Dwarf galaxies in the MATLAS Survey: Hubble Space Telescope observations of the globular cluster systems of 74 ultra-diffuse galaxies. *A&A* 690 A339, A339.

Martín-Navarro, I., Romanowsky, A. J., Brodie, J. P., Ferré-Mateu, A., Alabi, A., Forbes, D. A., Sharina, M., Villaume, A., Pandya, V., and Martinez-Delgado, D. (Apr. 2019). Extreme chemical abundance ratio suggesting an exotic origin for an ultradiffuse galaxy. *MNRAS* 484(3), 3425–3433.

Martínez-Delgado, D., Läsker, R., Sharina, M., Toloba, E., Fliri, J., Beaton, R., Valls-Gabaud, D., Karachentsev, I. D., Chonis, T. S., Grebel, E. K., Forbes, D. A., Romanowsky, A. J., Gallego-Laborda, J., Teuwen, K., Gómez-Flechoso, M. A., Wang, J., Guhathakurta, P., Kaisin, S., and Ho, N. (Apr. 2016). Discovery of an Ultra-diffuse Galaxy in the Pisces–Perseus Supercluster. *AJ* 151(4) 96, 96.

Massari, D., Koppelman, H. H., and Helmi, A. (Oct. 2019). Origin of the system of globular clusters in the Milky Way. *A&A* 630 L4, L4.

Mateu, C. (Apr. 2023). galstreams: A library of Milky Way stellar stream footprints and tracks. *MNRAS* 520(4), 5225–5258.

McConnachie, A. W. (July 2012). The Observed Properties of Dwarf Galaxies in and around the Local Group. *AJ* 144(1) 4, 4.

Mihos, J. C. and Hernquist, L. (June 1996). Gasdynamics and Starbursts in Major Mergers. *ApJ* 464, 641.

Miller, B. W. and Lotz, J. M. (Dec. 2007). The Globular Cluster Luminosity Function and Specific Frequency in Dwarf Elliptical Galaxies. *ApJ* 670(2), 1074–1089.

Miocchi, P., Capuzzo Dolcetta, R., Di Matteo, P., and Vicari, A. (June 2006). Merging of Globular Clusters in Inner Galactic Regions. I. Do They Survive the Tidal Interaction? *ApJ* 644(2), 940–953.

Miocchi, P., Lanzoni, B., Ferraro, F. R., Dalessandro, E., Vesperini, E., Pasquato, M., Beccari, G., Pallanca, C., and Sanna, N. (Sept. 2013). Star Count Density Profiles and Structural Parameters of 26 Galactic Globular Clusters. *ApJ* 774(2) 151, 151.

Mirabile, M., Cantiello, M., Lonare, P., Ragusa, R., Paolillo, M., Hazra, N., La Marca, A., Iodice, E., Spavone, M., Mieske, S., Rejkuba, M., Hilker, M., Riccio, G., Habas, R. A., Brocato, E., Schipani, P., Grado, A., and Limatola, L. (Nov. 2024). VEGAS-SSS: Tracing globular cluster populations in the interacting NGC 3640 galaxy group. *A&A* 691 A104, A104.

Montero-Dorta, A. D., Rodriguez, F., Artale, M. C., Smith, R., and Chaves-Montero, J. (Jan. 2024). Tracking the evolution of satellite galaxies: mass stripping and dark-matter deficient galaxies. *MNRAS* 527(3), 5868–5885.

Montes, M., Annibali, F., Bellazzini, M., Borlaff, A. S., Brough, S., Buitrago, F., Chamba, N., Collins, C., Dell'Antonio, I., Escala, I., Gonzalez, A. H., Holwerda, B., Kaviraj, S., Knapen, J., Koekemoer, A., Laine, S., Marcum, P., Martin, G., Martinez-Delgado, D., Mihos, C., Ricotti, M., Trujillo, I., and Watkins, A. E. (June 2023). Optimizing Roman's High Latitude Wide Area Survey for Low Surface Brightness Astronomy. *arXiv e-prints* arXiv:2306.09414, arXiv:2306.09414.

Moreno-Hilario, E., Martinez-Medina, L. A., Li, H., Souza, S. O., and Pérez-Villegas, A. (Jan. 2024a). The influence of globular cluster evolution on the specific frequency in dwarf galaxies. *MNRAS* 527(2), 2765–2780.

Moreno-Hilario, E., Martinez-Medina, L. A., Li, H., Souza, S. O., and Pérez-Villegas, A. (Jan. 2024b). The influence of globular cluster evolution on the specific frequency in dwarf galaxies. *MNRAS* 527(2), 2765–2780.

Mowla, L., Iyer, K., Asada, Y., Desprez, G., Tan, V. Y. Y., Martis, N., Sarrouh, G., Strait, V., Abraham, R., Bradač, M., Brammer, G., Muzzin, A., Pacifici, C., Ravindranath, S., Sawicki, M., Willott, C., Estrada-Carpenter, V., Jahan, N., Noirot, G., Matharu, J., Rihtaršič, G., and Zabl, J. (Dec. 2024). Formation of a low-mass galaxy from star clusters in a 600-million-year-old Universe. *Nature* 636(8042), 332–336.

Müller, O., Durrell, P. R., Marleau, F. R., Duc, P.-A., Lim, S., Posti, L., Agnello, A., Sánchez-Janssen, R., Poulain, M., Habas, R., Emsellem, E., Paudel, S., van der Burg, R. F. J., and Fensch, J. (Dec. 2021). Dwarf Galaxies in the MATLAS Survey: Hubble Space Telescope Observations of the Globular Cluster System in the Ultra-diffuse Galaxy MATLAS-2019. *ApJ* 923(1) 9, 9.

Müller, O., Marleau, F. R., Duc, P.-A., Habas, R., Fensch, J., Emsellem, E., Poulain, M., Lim, S., Agnello, A., Durrell, P., Paudel, S., Sánchez-Janssen, R., and van der Burg, R. F. J. (Aug. 2020). Spectroscopic study of MATLAS-2019 with MUSE: An ultra-diffuse galaxy with an excess of old globular clusters. *A&A* 640 A106, A106.

Munshi, F., Brooks, A. M., Applebaum, E., Christensen, C. R., Quinn, T., and Sligh, S. (Dec. 2021). Quantifying Scatter in Galaxy Formation at the Lowest Masses. *ApJ* 923(1) 35, 35.

Murray, C. E., Hasselquist, S., Peek, J. E. G., Lindberg, C. W., Almeida, A., Choi, Y., Craig, J. E. M., Dénes, H., Dickey, J. M., Di Teodoro, E. M., Federrath, C., Gerrard, I. A., Gibson, S. J., Leahy, D., Lee, M.-Y., Lynn, C., Ma, Y. K., Marchal, A., McClure-Griffiths, N. M., Nidever, D., Nguyen, H., Pingel, N. M., Tarantino, E., Uscanga, L., and van Loon, J. T. (Feb. 2024). A Galactic Eclipse: The Small Magellanic Cloud Is Forming Stars in Two Superimposed Systems. *ApJ* 962(2) 120, 120.

Murray, C. E., Peek, J. E. G., Di Teodoro, E. M., McClure-Griffiths, N. M., Dickey, J. M., and Dénes, H. (Dec. 2019). The 3D Kinematics of Gas in the Small Magellanic Cloud. *ApJ* 887(2) 267, 267.

Myeong, G. C., Vasiliev, E., Iorio, G., Evans, N. W., and Belokurov, V. (Sept. 2019). Evidence for two early accretion events that built the Milky Way stellar halo. *MNRAS* 488(1), 1235–1247.

Nadler, E. O., Wechsler, R. H., Bechtol, K., Mao, Y. .-., Green, G., Drlica-Wagner, A., McNanna, M., Mau, S., Pace, A. B., Simon, J. D., Kravtsov, A., Dodelson, S., Li, T. S., Riley, A. H., Wang, M. Y., Abbott, T. M. C., Aguena, M., Allam, S., Annis, J., Avila, S., Bernstein, G. M., Bertin, E., Brooks, D., Burke, D. L., Rosell, A. C., Kind, M. C., Carretero, J., Costanzi, M., da Costa, L. N., De Vicente, J., Desai, S., Evrard, A. E., Flaugher, B., Fosalba, P., Frieman, J., García-Bellido, J., Gaztanaga, E., Gerdes, D. W., Gruen, D., Gschwend, J., Gutierrez, G., Hartley, W. G., Hinton, S. R., Honscheid, K., Krause, E., Kuehn, K., Kuropatkin, N., Lahav, O., Maia, M. A. G., Marshall, J. L., Menanteau, F., Miquel, R., Palmese, A., Paz-Chinchón, F., Plazas, A. A., Romer, A. K., Sanchez, E., Santiago, B., Scarpine, V., Serrano, S., Smith, M., Soares-Santos, M., Suchyta, E., Tarle, G., Thomas, D., Varga, T. N., Walker, A. R., and DES Collaboration (Apr. 2020). Milky Way Satellite Census. II. Galaxy-Halo Connection Constraints Including the Impact of the Large Magellanic Cloud. *ApJ* 893(1) 48, 48.

Nagai, D. and Kravtsov, A. V. (Jan. 2005). The Radial Distribution of Galaxies in Λ Cold Dark Matter Clusters. *ApJ* 618(2), 557–568.

Narayanan, D. and Davé, R. (July 2012). Cosmological implications of a stellar initial mass function that varies with the Jeans mass in galaxies. *MNRAS* 423(4), 3601–3615.

Newman, A. B., Treu, T., Ellis, R. S., Sand, D. J., Nipoti, C., Richard, J., and Jullo, E. (Mar. 2013). The Density Profiles of Massive, Relaxed Galaxy Clusters. I. The Total Density Over Three Decades in Radius. *ApJ* 765(1) 24, 24.

Newton, O., Davies, J. J., Pfeffer, J., Crain, R. A., Kruijssen, J. M. D., Pontzen, A., and Bastian, N. (Sept. 2024). The formation and disruption of globular cluster populations in simulations of present-day L^* galaxies with controlled assembly histories. *arXiv e-prints* arXiv:2409.04516, arXiv:2409.04516.

Okabe, A., Boots, B., and Sugihara, K. (1992). *Spatial tessellations. Concepts and Applications of Voronoi diagrams.* Wiley.

Padoan, P., Jimenez, R., and Jones, B. (Mar. 1997). On star formation in primordial protoglobular clouds. *MNRAS* 285(4), 711–717.

Pasquali, A., Gallazzi, A., Fontanot, F., van den Bosch, F. C., De Lucia, G., Mo, H. J., and Yang, X. (Sept. 2010). Ages and metallicities of central and satellite galaxies: implications for galaxy formation and evolution. *MNRAS* 407(2), 937–954.

Patel, E., Besla, G., and Mandel, K. (July 2017). Orbits of massive satellite galaxies - II. Bayesian estimates of the Milky Way and Andromeda masses using high-precision astrometry and cosmological simulations. *MNRAS* 468(3), 3428–3449.

Peebles, P. J. E. (Feb. 1984). Dark matter and the origin of galaxies and globular star clusters. *ApJ* 277, 470–477.

Peebles, P. J. E. and Dicke, R. H. (Dec. 1968). Origin of the Globular Star Clusters. *ApJ* 154, 891.

Peletier, R. F., Davies, R. L., Illingworth, G. D., Davis, L. E., and Cawson, M. (Oct. 1990). CCD Surface Photometry of Galaxies with Dynamical Data. II. UBR Photometry of 39 Elliptical Galaxies. *AJ* 100, 1091.

Peñarrubia, J., Varri, A. L., Breen, P. G., Ferguson, A. M. N., and Sánchez-Janssen, R. (Oct. 2017). Stellar envelopes of globular clusters embedded in dark mini-haloes. *MNRAS* 471(1), L31–L35.

Peñarrubia, J., Walker, M. G., and Gilmore, G. (Nov. 2009). Tidal disruption of globular clusters in dwarf galaxies with triaxial dark matter haloes. *MNRAS* 399(3), 1275–1292.

Peng, E. W., Ferguson, H. C., Goudfrooij, P., Hammer, D., Lucey, J. R., Marzke, R. O., Puzia, T. H., Carter, D., Balcells, M., Bridges, T., Chiboucas, K., del Burgo, C., Graham, A. W., Guzmán, R., Hudson, M. J., Matković, A., Merritt, D., Miller, B. W., Mouhcine, M., Phillipps, S., Sharples, R., Smith, R. J., Tully, B., and Verdoes Kleijn, G. (Mar. 2011). The HST/ACS Coma Cluster Survey. IV. Intergalactic Globular Clusters and the Massive Globular Cluster System at the Core of the Coma Galaxy Cluster. *ApJ* 730(1) 23, 23.

Peng, E. W., Jordán, A., Côté, P., Takamiya, M., West, M. J., Blakeslee, J. P., Chen, C.-W., Ferrarese, L., Mei, S., Tonry, J. L., and West, A. A. (July 2008). The ACS Virgo Cluster Survey. XV. The Formation Efficiencies of Globular Clusters in Early-Type Galaxies: The Effects of Mass and Environment. *ApJ* 681(1), 197–224.

Peng, E. W. and Lim, S. (May 2016). A Rich Globular Cluster System in Dragonfly 17: Are Ultra-diffuse Galaxies Pure Stellar Halos? *ApJ* 822(2) L31, L31.

Peterson, C. J. and King, I. R. (June 1975). The structure of star clusters. VI. Observed radii and structural parameters in globular clusters. *AJ* 80, 427–436.

Pfeffer, J., Forbes, D. A., Romanowsky, A. J., Bastian, N., Crain, R. A., Kruijssen, J. M. D., Bekki, K., Brodie, J. P., Chevance, M., Couch, W. J., and Gannon, J. S. (Jan. 2025). Comparing E-MOSAICS predictions of high-redshift proto-globular clusters with JWST observations in lensed galaxies. *MNRAS* 536(2), 1878–1893.

Pfeffer, J., Kruijssen, J. M. D., Crain, R. A., and Bastian, N. (Apr. 2018). The E-MOSAICS project: simulating the formation and co-evolution of galaxies and their star cluster populations. *MNRAS* 475(4), 4309–4346.

Planck Collaboration et al. (Sept. 2016). Planck 2015 results. XIII. Cosmological parameters. *A&A* 594 A13, A13.

Planck Collaboration et al. (Sept. 2020). Planck 2018 results. VI. Cosmological parameters. *A&A* 641 A6, A6.

Popesso, P., Biviano, A., Böhringer, H., and Romaniello, M. (Mar. 2007). RASS-SDSS galaxy cluster survey. VII. On the cluster mass-to-light ratio and the halo occupation distribution. *A&A* 464(2), 451–464.

Poulain, M., Marleau, F. R., Habas, R., Duc, P.-A., Sánchez-Janssen, R., Durrell, P. R., Paudel, S., Ahad, S. L., Chougule, A., Müller, O., Lim, S., Bílek, M., and Fensch, J. (Oct. 2021). Structure and morphology of the MATLAS dwarf galaxies and their central nuclei. *MNRAS* 506(4), 5494–5511.

Prieto, J. L. and Gnedin, O. Y. (Dec. 2008). Dynamical Evolution of Globular Clusters in Hierarchical Cosmology. *ApJ* 689(2), 919–935.

Prole, D. J., Hilker, M., van der Burg, R. F. J., Cantiello, M., Venhola, A., Iodice, E., van de Ven, G., Wittmann, C., Peletier, R. F., Mieske, S., Capaccioli, M., Napolitano, N. R., Paolillo, M., Spavone, M., and Valentijn, E. (Apr. 2019). Halo mass estimates from the globular cluster populations of 175 low surface brightness galaxies in the Fornax cluster. *MNRAS* 484(4), 4865–4880.

Ramella, M., Boschin, W., Fadda, D., and Nonino, M. (Mar. 2001). Finding galaxy clusters using Voronoi tessellations. *A&A* 368, 776–786.

Read, J. I., Iorio, G., Agertz, O., and Fraternali, F. (May 2017). The stellar mass-halo mass relation of isolated field dwarfs: a critical test of ΛCDM at the edge of galaxy formation. *MNRAS* 467(2), 2019–2038.

Reina-Campos, M., Keller, B. W., Kruijssen, J. M. D., Gensior, J., Trujillo-Gomez, S., Jeffreson, S. M. R., Pfeffer, J. L., and Sills, A. (Dec. 2022). Introducing EMP-Pathfinder: modelling the simultaneous formation and evolution of stellar clusters in their host galaxies. *MNRAS* 517(3), 3144–3180.

Reina-Campos, M., Trujillo-Gomez, S., Pfeffer, J. L., Sills, A., Deason, A. J., Crain, R. A., and Kruijssen, J. M. D. (June 2023). Constraining the shape of dark matter haloes with globular clusters and diffuse stellar light in the E-MOSAICS simulations. *MNRAS* 521(4), 6368–6382.

Renaud, F., Segovia Otero, Á., and Agertz, O. (Nov. 2022). The merger-starburst connection across cosmic times. *MNRAS* 516(4), 4922–4931.

Ryon, J. E. (2019). *Advanced Camera for Surveys Instrument Handbook for Cycle 27 v. 18.0.*

Saifollahi, T. et al. (Mar. 2025a). Euclid: Early Release Observations – Interplay between dwarf galaxies and their globular clusters in the Perseus galaxy cluster. *arXiv e-prints* arXiv:2503.16367, arXiv:2503.16367.

Saifollahi, T. et al. (May 2025b). Euclid: Early Release Observations – Globular clusters in the Fornax galaxy cluster, from dwarf galaxies to the intracluster field. *A&A* 697 A10, A10.

Saifollahi, T., Zaritsky, D., Trujillo, I., Peletier, R. F., Knapen, J. H., Amorisco, N., Beasley, M. A., and Donnerstein, R. (Feb. 2022). Implications for galaxy formation models from observations of Globular Clusters around Ultra-Diffuse Galaxies. *MNRAS*.

Sánchez-Janssen, R., Côté, P., Ferrarese, L., Peng, E. W., Roediger, J., Blakeslee, J. P., Emsellem, E., Puzia, T. H., Spengler, C., Taylor, J., Álamo-Martínez, K. A., Boselli, A., Cantiello, M., Cuillandre, J.-C., Duc, P.-A., Durrell, P., Gwyn, S., MacArthur, L. A., Lançon, A., Lim, S., Liu, C., Mei, S., Miller, B., Muñoz, R., Mihos, J. C., Paudel, S., Powalka, M., and Toloba, E. (June 2019). The Next Generation Virgo Cluster Survey. XXIII. Fundamentals of Nuclear Star Clusters over Seven Decades in Galaxy Mass. *ApJ* 878(1) 18, 18.

Scharré, L., Sorini, D., and Davé, R. (Oct. 2024). The effects of stellar and AGN feedback on the cosmic star formation history in the SIMBA simulations. *MNRAS* 534(1), 361–383.

Schaye, J., Crain, R. A., Bower, R. G., Furlong, M., Schaller, M., Theuns, T., Dalla Vecchia, C., Frenk, C. S., McCarthy, I. G., Helly, J. C., Jenkins, A., Rosas-Guevara, Y. M., White, S. D. M., Baes, M., Booth, C. M., Camps, P., Navarro, J. F., Qu, Y., Rahmati, A., Sawala, T., Thomas, P. A., and Trayford, J. (Jan. 2015). The EAGLE project: simulating the evolution and assembly of galaxies and their environments. *MNRAS* 446(1), 521–554.

Searle, L. and Zinn, R. (Oct. 1978). Composition of halo clusters and the formation of the galactic halo. *ApJ* 225, 357–379.

Shen, Z., Danieli, S., van Dokkum, P., Abraham, R., Brodie, J. P., Conroy, C., Dolphin, A. E., Romanowsky, A. J., Kruijssen, J. M. D., and Dutta Chowdhury, D. (June 2021). A Tip of the Red Giant Branch Distance of 22.1 ± 1.2 Mpc to the Dark Matter Deficient Galaxy NGC 1052-DF2 from 40 Orbits of Hubble Space Telescope Imaging. *ApJL* 914(1) L12, L12.

Shen, Z., van Dokkum, P., and Danieli, S. (Sept. 2023). Confirmation of an anomalously low dark matter content for the galaxy NGC1052-DF4 from deep, high resolution continuum spectroscopy. *arXiv e-prints* arXiv:2309.08592, arXiv:2309.08592.

Shin, M.-S. and Kawata, D. (Jan. 2009). The Spatial Distributions of Red and Blue Globular Clusters in Major Dry Merger Remnants. *ApJ* 691(1), 83–90.

Simpson, J. D., De Silva, G., Martell, S. L., Navin, C. A., and Zucker, D. B. (Dec. 2017). ESO 452-SC11: the lowest mass globular cluster with a potential chemical inhomogeneity. *MNRAS* 472(3), 2856–2868.

Spilker, J. S., Suess, K. A., Setton, D. J., Bezanson, R., Feldmann, R., Greene, J. E., Kriek, M., Lower, S., Narayanan, D., and Verrico, M. (Sept. 2022). Star Formation Suppression by Tidal Removal of Cold Molecular Gas from an Intermediate-redshift Massive Post-starburst Galaxy. *ApJ* 936(1) L11, L11.

Spitler, L. R. and Forbes, D. A. (Jan. 2009). A new method for estimating dark matter halo masses using globular cluster systems. *MNRAS* 392(1), L1–L5.

Spitler, L. R., Forbes, D. A., Strader, J., Brodie, J. P., and Gallagher, J. S. (Mar. 2008). The connection between globular cluster systems and their host galaxy and environment: a case study of the isolated elliptical NGC 821. *MNRAS* 385(1), 361–380.

Springel, V. and Farrar, G. R. (Sept. 2007). The speed of the 'bullet' in the merging galaxy cluster 1E0657-56. *MNRAS* 380(3), 911–925.

Strader, J., Brodie, J. P., Spitler, L., and Beasley, M. A. (Dec. 2006). Globular Clusters in Virgo Ellipticals: Unexpected Results for Giants and Dwarfs from Advanced Camera for Surveys Imaging. *AJ* 132(6), 2333–2345.

Suârez-Plasencia, L., Herrera-Macıas, J. A., Legôn-Pêrez, C. M., Socorro-LLanes, R., Rojas, O., and Sosa-Gômez, G. (July 2021). Analysis of the Number of Sides of Voronoi Polygons in PassPoint. In: *Lecture Notes of the Institute for Computer Sciences, Social Informatics and Telecommunications Engineering.*

Taylor, E. N., Hopkins, A. M., Baldry, I. K., Brown, M. J. I., Driver, S. P., Kelvin, L. S., Hill, D. T., Robotham, A. S. G., Bland-Hawthorn, J., Jones, D. H., Sharp, R. G., Thomas, D., Liske, J., Loveday, J., Norberg, P., Peacock, J. A., Bamford, S. P., Brough, S., Colless, M., Cameron, E., Conselice, C. J., Croom, S. M., Frenk, C. S., Gunawardhana, M., Kuijken, K., Nichol, R. C., Parkinson, H. R., Phillipps, S., Pimbblet, K. A., Popescu, C. C., Prescott, M., Sutherland, W. J., Tuffs, R. J., van Kampen, E., and Wijesinghe, D. (Dec. 2011). Galaxy And Mass Assembly (GAMA): stellar mass estimates. *MNRAS* 418(3), 1587–1620.

Toloba, E., Lim, S., Peng, E., Sales, L. V., Guhathakurta, P., Mihos, J. C., Côté, P., Boselli, A., Cuillandre, J.-C., Ferrarese, L., Gwyn, S., Lançon, A., Muñoz, R., and Puzia, T. (Apr.

2018). Dark Matter in Ultra-diffuse Galaxies in the Virgo Cluster from Their Globular Cluster Populations. *ApJL* 856(2) L31, L31.

Toloba, E., Sales, L. V., Lim, S., Peng, E. W., Guhathakurta, P., Roediger, J., Wang, K., Mihos, J. C., Cote, P., Durrell, P. R., and Ferrarese, L. (May 2023). The Next Generation Virgo Cluster Survey (NGVS). XXXV. First Kinematical Clues of Overly-Massive Dark Matter Halos in Several Ultra-Diffuse Galaxies in the Virgo Cluster. *arXiv e-prints* arXiv:2305.06369, arXiv:2305.06369.

Tozuka, M., Kawabata, K., Fukazawa, Y., Nishiura, S., and Hiraga, J. (Dec. 2021). Distributions of dwarf galaxies around giant elliptical galaxies NGC 3923 and NGC 4636. *Stars and Galaxies* 4, 6.

Trenti, M., Padoan, P., and Jimenez, R. (Aug. 2015). The Relative and Absolute Ages of Old Globular Clusters in the LCDM Framework. *ApJ* 808(2) L35, L35.

Tsuge, K., Fukui, Y., Tachihara, K., Sano, H., Tokuda, K., Ueda, J., Iono, D., and Finn, M. K. (Jan. 2021). The formation of young massive clusters triggered by cloud-cloud collisions in the Antennae galaxies NGC 4038/NGC 4039. *PASJ* 73, S35–S61.

Urbano, M. et al. (Dec. 2024). Euclid: Early Release Observations of diffuse stellar structures and globular clusters as probes of the mass assembly of galaxies in the Dorado group. *arXiv e-prints* arXiv:2412.17672, arXiv:2412.17672.

Usher, C., Dage, K. C., Girardi, L., Barmby, P., Bonatto, C. J., Chies-Santos, A. L., Clarkson, W. I., Gómez Camus, M., Hartmann, E. A., Ferguson, A. M. N., Pieres, A., Prisinzano, L., Rhode, K. L., Rich, R. M., Ripepi, V., Santiago, B., Stassun, K. G., Street, R. A., Szabó, R., Venuti, L., Zaggia, S., Canossa, M., Floriano, P., Lopes, P., Miranda, N. L., Oliveira, R. A. P., Reina-Campos, M., Roman-Lopes, A., and Sobeck, J. (July 2023). Rubin Observatory LSST Stars Milky Way and Local Volume Star Clusters Roadmap. *PASP* 135(1049) 074201, 074201.

Usher, C., Forbes, D. A., Brodie, J. P., Romanowsky, A. J., Strader, J., Conroy, C., Foster, C., Pastorello, N., Pota, V., and Arnold, J. A. (Jan. 2015). The SLUGGS survey: globular cluster stellar population trends from weak absorption lines in stacked spectra. *MNRAS* 446(1), 369–390.

Valenzuela, L. M., Moster, B. P., Remus, R.-S., O'Leary, J. A., and Burkert, A. (Aug. 2021). Globular cluster numbers in dark matter haloes in a dual formation scenario: an empirical model within EMERGE. *MNRAS* 505(4), 5815–5832.

Valenzuela, L. M., Remus, R.-S., McKenzie, M., and Forbes, D. A. (July 2024). Galaxy archaeology for wet mergers: Globular cluster age distributions in the Milky Way and nearby galaxies. *A&A* 687 A104, A104.

van de Weygaert, R. and Icke, V. (Apr. 1989). Fragmenting the universe. II - Voronoi vertices as Abell clusters. *A&A* 213(1-2), 1–9.

van Dokkum, P., Abraham, R., Brodie, J., Conroy, C., Danieli, S., Merritt, A., Mowla, L., Romanowsky, A., and Zhang, J. (Sept. 2016). A High Stellar Velocity Dispersion and ∼100 Globular Clusters for the Ultra-diffuse Galaxy Dragonfly 44. *ApJL* 828(1) L6, L6.

van Dokkum, P., Abraham, R., Romanowsky, A. J., Brodie, J., Conroy, C., Danieli, S., Lokhorst, D., Merritt, A., Mowla, L., and Zhang, J. (July 2017). Extensive Globular Cluster Systems Associated with Ultra Diffuse Galaxies in the Coma Cluster. *ApJL* 844(1) L11, L11.

van Dokkum, P., Danieli, S., Cohen, Y., Merritt, A., Romanowsky, A. J., Abraham, R., Brodie, J., Conroy, C., Lokhorst, D., Mowla, L., O'Sullivan, E., and Zhang, J. (Mar. 2018). A galaxy lacking dark matter. *Nature* 555(7698), 629–632.

van Dokkum, P., Li, D. D., Abraham, R., Danieli, S., Eadie, G. M., Harris, W. E., and Romanowsky, A. J. (May 2024). Deep HST/UVIS Imaging of the Candidate Dark Galaxy CDG-1. *Research Notes of the American Astronomical Society* 8(5) 135, 135.

van Dokkum, P., Shen, Z., Keim, M. A., Trujillo-Gomez, S., Danieli, S., Dutta Chowdhury, D., Abraham, R., Conroy, C., Kruijssen, J. M. D., Nagai, D., and Romanowsky, A. (May 2022). A trail of dark-matter-free galaxies from a bullet-dwarf collision. *Nature* 605(7910), 435–439.

van Dokkum, P., Wasserman, A., Danieli, S., Abraham, R., Brodie, J., Conroy, C., Forbes, D. A., Martin, C., Matuszewski, M., Romanowsky, A. J., and Villaume, A. (Aug. 2019). Spatially Resolved Stellar Kinematics of the Ultra-diffuse Galaxy Dragonfly 44. I. Observations, Kinematics, and Cold Dark Matter Halo Fits. *ApJ* 880(2) 91, 91.

van Dokkum, P. G., Abraham, R., Merritt, A., Zhang, J., Geha, M., and Conroy, C. (Jan. 2015a). Forty-seven Milky Way-sized, Extremely Diffuse Galaxies in the Coma Cluster. *ApJL* 798(2) L45, L45.

van Dokkum, P. G., Romanowsky, A. J., Abraham, R., Brodie, J. P., Conroy, C., Geha, M., Merritt, A., Villaume, A., and Zhang, J. (May 2015b). Spectroscopic Confirmation of the Existence of Large, Diffuse Galaxies in the Coma Cluster. *ApJ* 804(1) L26, L26.

VandenBerg, D. A., Brogaard, K., Leaman, R., and Casagrande, L. (Oct. 2013). The Ages of 55 Globular Clusters as Determined Using an Improved $\hat{V}$HB_TO Method along with Color-Magnitude Diagram Constraints, and Their Implications for Broader Issues. *ApJ* 775(2) 134, 134.

Vanzella, E., Claeyssens, A., Welch, B., Adamo, A., Coe, D., Diego, J. M., Mahler, G., Khullar, G., Kokorev, V., Oguri, M., Ravindranath, S., Furtak, L. J., Hsiao, T. Y.-Y., Abdurro'uf, Mandelker, N., Brammer, G., Bradley, L. D., Bradač, M., Conselice, C. J., Dayal, P., Nonino, M., Andrade-Santos, F., Windhorst, R. A., Pirzkal, N., Sharon, K., de Mink, S. E., Fujimoto, S., Zitrin, A., Eldridge, J. J., and Norman, C. (Mar. 2023). JWST/NIRCam Probes Young Star Clusters in the Reionization Era Sunrise Arc. *ApJ* 945(1) 53, 53.

Vasiliev, E. and Baumgardt, H. (Aug. 2021). Gaia EDR3 view on galactic globular clusters. *MNRAS* 505(4), 5978–6002.

Veale, M., Ma, C.-P., Thomas, J., Greene, J. E., McConnell, N. J., Walsh, J., Ito, J., Blakeslee, J. P., and Janish, R. (Jan. 2017). The MASSIVE Survey - V. Spatially resolved stellar angular momentum, velocity dispersion, and higher moments of the 41 most massive local early-type galaxies. *MNRAS* 464(1), 356–384.

Veršič, T., Rejkuba, M., Arnaboldi, M., Gerhard, O., Pulsoni, C., Valenzuela, L. M., Hartke, J., Watkins, L. L., van de Ven, G., and Thater, S. (July 2024). Shapes of dark matter haloes with discrete globular cluster dynamics: The example of NGC 5128 (Centaurus A). *A&A* 687 A80, A80.

Vesperini, E. and Heggie, D. C. (Aug. 1997). On the effects of dynamical evolution on the initial mass function of globular clusters. *MNRAS* 289(4), 898–920.

Villaume, A., Romanowsky, A. J., Brodie, J., van Dokkum, P., Conroy, C., Forbes, D. A., Danieli, S., Martin, C., and Matuszewski, M. (Jan. 2022). Spatially Resolved Stellar Spectroscopy of the Ultra-diffuse Galaxy Dragonfly 44. III. Evidence for an Unexpected Star Formation History under Conventional Galaxy Evolution Processes. *ApJ* 924(1) 32, 32.

Villegas, D., Jordán, A., Peng, E. W., Blakeslee, J. P., Côté, P., Ferrarese, L., Kissler-Patig, M., Mei, S., Infante, L., Tonry, J. L., and West, M. J. (July 2010). The ACS Fornax Cluster Survey. VIII. The Luminosity Function of Globular Clusters in Virgo and Fornax Early-type Galaxies and Its Use as a Distance Indicator. *ApJ* 717(2), 603–616.

Virtanen, P., Gommers, R., Oliphant, T. E., Haberland, M., Reddy, T., Cournapeau, D., Burovski, E., Peterson, P., Weckesser, W., Bright, J., van der Walt, S. J., Brett, M., Wilson, J., Millman, K. J., Mayorov, N., Nelson, A. R. J., Jones, E., Kern, R., Larson, E., Carey, C. J., Polat, İ., Feng, Y., Moore, E. W., VanderPlas, J., Laxalde, D., Perktold, J., Cimrman, R., Henriksen, I., Quintero, E. A., Harris, C. R., Archibald, A. M., Ribeiro, A. H., Pedregosa, F., van Mulbregt, P., and SciPy 1.0 Contributors (2020). SciPy 1.0: Fundamental Algorithms for Scientific Computing in Python. *Nature Methods* 17, 261–272.

Vitral, E. and Boldrini, P. (Nov. 2022). Properties of globular clusters formed in dark matter mini-halos. *A&A* 667 A112, A112.

Wan, Z., Lewis, G. F., Li, T. S., Simpson, J. D., Martell, S. L., Zucker, D. B., Mould, J. R., Erkal, D., Pace, A. B., Mackey, D., Ji, A. P., Koposov, S. E., Kuehn, K., Shipp, N., Balbinot, E., Bland-Hawthorn, J., Casey, A. R., Da Costa, G. S., Kafle, P., Sharma, S., and De Silva, G. M. (July 2020). The tidal remnant of an unusually metal-poor globular cluster. *Nature* 583(7818), 768–770.

Webb, K. A., Villaume, A., Laine, S., Romanowsky, A. J., Balogh, M., van Dokkum, P., Forbes, D. A., Brodie, J., Martin, C., and Matuszewski, M. (Nov. 2022). Still at odds with conventional galaxy evolution: the star formation history of ultradiffuse galaxy Dragonfly 44. *MNRAS* 516(3), 3318–3341.

Weinberger, R., Springel, V., Hernquist, L., Pillepich, A., Marinacci, F., Pakmor, R., Nelson, D., Genel, S., Vogelsberger, M., Naiman, J., and Torrey, P. (Mar. 2017). Simulating galaxy formation with black hole driven thermal and kinetic feedback. *MNRAS* 465(3), 3291–3308.

Wetzel, A. R., Tinker, J. L., Conroy, C., and van den Bosch, F. C. (June 2013). Galaxy evolution in groups and clusters: satellite star formation histories and quenching time-scales in a hierarchical Universe. *MNRAS* 432(1), 336–358.

Whitaker, K. E., Cutler, S. E., Chandar, R., Pan, R., Setton, D. J., Furtak, L. J., Bezanson, R., Labbé, I., Leja, J., Suess, K. A., Wang, B., Weaver, J. R., Atek, H., Brammer, G. B., Feldmann, R., Förster Schreiber, N. M., Glazebrook, K., de Graaff, A., Greene, J. E., Khullar, G., Marchesini, D., Maseda, M. V., Miller, T. B., Mo, H., Mowla, L. A., Nanayakkara, T., Nelson, E. J., Price, S. H., Rizzo, F., van Dokkum, P., Williams, C. C., Zhang, Y., Zhang, Y., and Zitrin, A. (Jan. 2025). Discovery of Ancient Globular Cluster Candidates in The Relic, a Quiescent Galaxy at z=2.5. *arXiv e-prints* arXiv:2501.07627, arXiv:2501.07627.

Woody, T. and Schlaufman, K. C. (Aug. 2021). The Age-Metallicity-Specific Orbital Energy Relation for the Milky Way's Globular Cluster System Confirms the Importance of Accretion for Its Formation. *AJ* 162(2) 42, 42.

Ying, J. (, Chaboyer, B., Boylan-Kolchin, M., Weisz, D. R., and Goebel-Bain, R. (July 2025). The Absolute Age of Milky Way Globular Clusters. *ApJ* 987(1) 52, 52.

Zepf, S. E. and Ashman, K. M. (Oct. 1993). Globular cluster systems formed in galaxy mergers. *MNRAS* 264, 611–618.

Zhang, E., Sales, L. V., Marinacci, F., Torrey, P., Vogelsberger, M., Springel, V., Li, H., Pakmor, R., and Gutcke, T. A. (Nov. 2024). Bursty Star Formation in Dwarfs is Sensitive to Numerical Choices in Supernova Feedback Models. *ApJ* 975(2) 229, 229.

Zhao, J.-H., Morris, M. R., and Goss, W. M. (Mar. 2022). Detection of a Dense Group of Hypercompact Radio Sources in the Central Parsec of the Galaxy. *ApJ* 927(1) L6, L6.